New version of the thesis,
revised post-publication and
released in March 2022

Evaluate the Performance of a Camber Controlled Cycloidal Rotor

Master Thesis

by

Doudou Huang

Conducted at the

Institute of Aerodynamics and Gas Dynamics

at the University of Stuttgart

Stuttgart, August 2021

Universität Stuttgart

INSTITUT FÜR AERODYNAMIK UND GASDYNAMIK IAG

DIREKTOR: PROF. DR.-ING. EWALD KRÄMER

Pfaffenwaldring 21, 70550 Stuttgart, Tel (0711) 685-3401, Fax 3402, email:kraemer@iag.uni-stuttgart.de

Master Thesis for Doudou Huang

Evaluate the Performance of a Camber Controlled Cycloidal Rotor

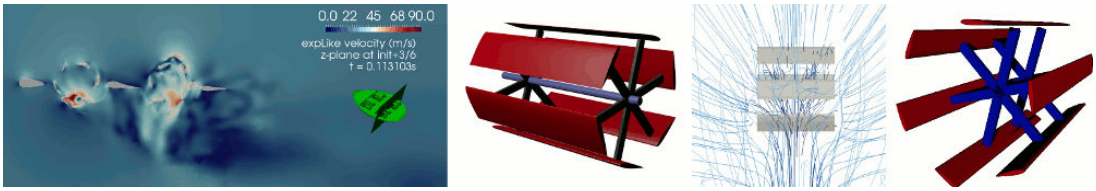

Cycloidal rotors have the advantages of providing 360° thrust forces and having constant flow velocities on their blades. However, the deformation of their blades reduces efficiency and is not well understood. Also, while air enters and exits the rotor, it encounters the blade twice and this favors dynamic stall and blade-vortex interaction. The given advantages over conventional helicopter rotors and consequent challenges make cyclorotors ideal for research. The aerodynamic phenomena they produce are investigated by means of numerical fluid simulation.

In their actual form, these rotors rely on the pitching of the airfoil to generate thrust. It is suspected that an implementation with no pitching could be simple yet efficient. In such a configuration, the creation of aerodynamic forces would be achieved by dynamically morphing the blades to considerably camber them.

The theme of the proposed thesis is thus to *improve the current cycloidal rotor CFD models to allow modeling morphing blades.* The objective is to *demonstrate possible improvements in the aerodynamic forces and power introduced by such a modification.*

Milestones:

- familiarize with the **OpenFOAM** CFD toolbox and the pimpleFoam tutorials
- model a rotating and oscillating airfoil using the Arbitrary Mesh Interface
- develop different **camber morphing concepts** to define the deformed blade shape
- extend the system to allow modelling **dynamically morphing blades**
- conduct the force and power analysis and identify the flow field behavior
- compare the results of cases with different camber morphing methods.

Date Issued: February 17th, 2021

Date Submitted: August 17th, 2021

Student: Doudou Huang

Advisor: Louis Gagnon

Examiner 1: Manuel Keßler

Examiner 2: Ewald Krämer

Statement of Originality

This thesis has been performed independently with support of my supervisor. It contains no material that has been accepted for the award of a degree at this or any other university. To the best of my knowledge and belief, this thesis contains no material previously published or written by another person except where due reference is made in the text.

I further declare that I have performed this thesis according to the existing copyright policy and the rules of good scientific practice. In case this work contains contributions of someone else (eg. pictures, drawings, text passages etc.), I have clearly identified the source of these contributions, and, if necessary, have obtained approval from the originator for making use of them in this thesis. I am aware that I have to bear the consequences in case I have contravened these duties.

_____

Date, Signature

Erklärung

Hiermit versichere ich, dass ich diese Bachelorarbeit selbstständig mit Unterstützung des Betreuers angefertigt und keine anderen als die angegebenen Quellen und Hilfsmittel verwendet habe. Die Arbeit oder wesentliche Bestandteile davon sind weder an dieser noch an einer anderen Bildungseinrichtung bereits zur Erlangung eines Abschlusses eingereicht worden.

Ich erkläre weiterhin, bei der Erstellung der Arbeit die einschlägigen Bestimmungen zum Urheberschutz fremder Beiträge entsprechend den Regeln guter wissenschaftlicher Praxis eingehalten zu haben. Soweit meine Arbeit fremde Beiträge (z.B. Bilder, Zeichnungen, Textpassagen etc.) enthält, habe ich diese Beiträge als solche gekennzeichnet (Zitat, Quellenangabe) und eventuell erforderlich gewordene Zustimmungen der Urheber zur Nutzung dieser Beiträge in meiner Arbeit eingeholt. Mir ist bekannt, dass ich im Falle einer schuldhaften Verletzung dieser Pflichten die daraus entstehenden Konsequenzen zu tragen habe.

Abstract

The curvature of the airfoil has a significant effect on the performance of the cycloidal rotor system. This paper aims to improve the aerodynamic performance of the cycloidal rotor system by utilizing dynamical morphing blades in a CFD model. Particularly, three different camber morphing concepts, including leading edge deflection, trailing edge deformation, and cambered NACA profile, are employed to a baseline 2-bladed system with rotating and pitching NACA0015 aerofoils. Based on these three camber concepts, a series of URANS 2-D numerical simulations in OpenFOAM are conducted for blades with different morphing degrees and positions. The simulation results verified that the flow field condition could be optimized and thus significant improvement in thrust and efficiency could be achieved by properly tuning the morphing control.

Übersicht

Die Wölbung von den Blättern hat einen wesentlichen Einfluss auf die aerodynamische Leistung eines Zyklorotors. Das Ziel dieser Arbeit ist es, die aerodynamische Leistung des Zyklorotorsystems durch die Verwendung dynamisch verformbarer Schaufeln im CFD-Modell zu verbessern. Konkret werden drei verschiedene Wölbung konzepte, einschließlich Vorderkantenverformung, Hinterkantenverformung und gewölbtes NACA-Profil, für ein 2-Blatt-Basissystem mit rotierenden und oszillierenden NACA0015-Profilen verwendet. Basierend auf diesen drei Camber-Konzepten werden numerischen URANS 2-D-Simulationen in OpenFOAM für Blätter mit unterschiedlichen Morphing-Graden und -Positionen durchgeführt. Die Simulationsergebnisse bestätigten, dass das Strömungsfeld optimiert werden konnte und somit eine signifikante Verbesserung von Schub und Effizienz durch den Einsatz der Morphing-Schaufel.

Contents

List of Figures

Nomenclature

t	Time
n	Number of blade
c	Chord length
b	Blade span
Δz	Actual thickness
μ	Thickness ratio
A_{res}	Reference area
Ω	Rotational speed
R	Rotation radius
ρ	Density
p	Camber position
m	Maximum camber degree
k	Turbulent kinetic energy
ω	Specific dissipation rate
ν_T	Turbulent viscosity
x, y, z	Cartesian coordinates
U_x, U_y, U_z	Velocity components in cartesian coordinates
$\bar{u}, \bar{v}, \bar{w}$	Main stream Velocity
u', v', w'	Turbulent fluctuations

θ	Pitching angle
ψ	Azimuth angle
Φ	Thrust angle
T	Time period for revolution
F_x, F_y	Sideward and vertical force
F_{res}	Resulting thrust
M_z	Torque in z direction
P	Power
P_{idea}	Ideal hover power
PL	Power loading
FoM	Figure of merit
Re	Reynolds Number
Co	Courant number

1 Introduction

1.1 Cycloidal Rotors

The cycloidal propeller is a novel concept of a rotary-wing system, where the rotation axis is parallel to the blade span. It has the advantages of providing 360° thrust force which is perpendicular to the rotational axis and maintaining constant flow velocity along the blade span. Consequently, it has the potential to achieve higher aerodynamic efficiency when compared with conventional propeller or helicopter rotor. Inspired by this, the cycloidal propeller has been considered to be a promising candidate for the propulsion system for various applications, such as VTOL vehicles, unmanned Air Vehicles (UAVs), and micro air vehicles (MAVs).

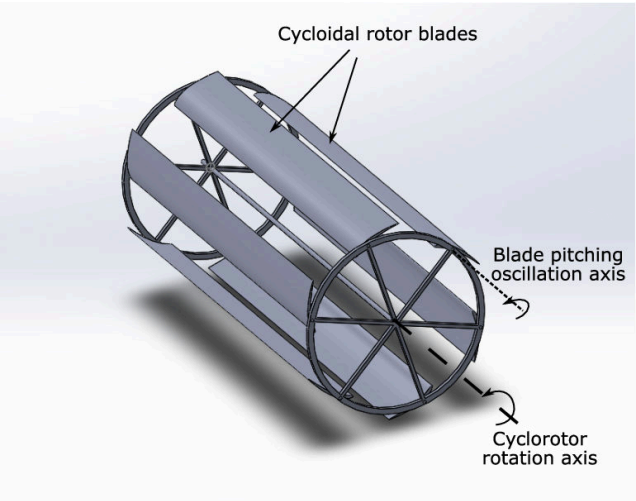

Figure 1.1: Schematic of a cycloidal rotor[1].

1.2 Literature Review

1.2.1 Previous Researches on Cycloidal Rotor

The origins of the cycloidal rotor can be traced back to the beginning of the twentieth century. In the early 1920s, the cycloidal propeller was patented by Prof. Kurt Kirsten from the University of

Washington who conducted many pieces of research for the cycloidal blade motion and successfully applied this concept to the vessel model. However, his subsequent commercial application attempts ended in failure.

Throughout the 1930s, National Advisory Committee for Aeronautics (NACA) continued the researches to obtain a further understanding of the aerodynamics and operation of cycloidal rotors. In 1933, Wheatley[2] developed a simplified momentum theory for the cyclogiro, which was later applied in a wind tunnel test[3]. The research showed that there were significant differences between the experimental test and analytical studies based on their simplified theory, where the unsteady aerodynamic phenomena were considered to be responsible for this deviation. Moreover, due to the lack of fundamental understanding of the mechanism and aerodynamic phenomena of the cycloidal rotor, almost all attempts to construct a flying cyclocopter in this period failed.

After World War II, the research of cycloidal propellers was temporarily suspended due to the great achievements of other rotary-wing aircraft and flying devices. Until the end of the 1990s, with the development of related disciplines, the concept of cycloidal rotor regained the extensive attention and considerable breakthroughs have been obtained in the past two decades.

Especially, Bosch Aerospace, University of Maryland (US), Seoul National University (S.Korea), University of Tsukuba (Japan), Technion-Israel Institute of Technology (TITT), and other institutions have made many important achievements in the field of the cycloidal rotor.

Several computational and experimental investigations were performed by the researchers at Seoul national University[4, 5, 6, 7]. Particularly, structure and system optimization was first developed to maximize thrust with predetermined engine power. Then the results were utilized in the design and creation of several UAV-scale cyclorotors with different sizes. Experimental flight test results showed that stable hovering flight could be demonstrated for both four-rotor and dual-rotor cyclorotors.

At the same time, Benedict[8, 9, 10, 11, 12] from the University of Maryland conducted a series of experimental and numerical researches to further understand the aerodynamic and performance characteristics of micro air vehicle (MAV) scale cycloidal rotors. He also successfully constructed and tested several lightweight cyclorotors from 29 to 800 grams.

Experiments developed by Adam John Kellen[13] achieved the optimal performance of a UAV-scale cyclorotor aerodynamic. In addition, the experiments with different blade configurations were conducted for different rotational speeds and blade pitch amplitudes. The results showed that at Reynolds number of 200,000, the optimal cycloidal rotor configuration was 3 blades with NACA0020 airfoil in a chord-by-radius ratio of 0.66, a blade aspect ratio (span/chord) of 4, and a rotor aspect ratio (span/diameter) of 1.33. Moreover, for cyclic pitch amplitude of $\pm 40^{\circ}$, this optimal rotor obtained a figure of merit of 0.6.

Therefore, the practicality of the cycloidal rotor concept is well demonstrated by the aforementioned investigations.

1.2.2 Researches on Morphing Helicopter Rotors

The curvature of the airfoil has significant impacts on the unsteady aerodynamic phenomena, e.g., blade dynamic stall and blade vortex interactions. Various researches on the morphing effect of helicopter rotors have been carried out in the past.

Michael Kerho[14] has developed an adaptive variable camber airfoil to alleviate the negative effects of dynamic stall. In his research, variable droop leading edge was adapted to the baseline Sikorsky SSC-A09 airfoil. The results of numerical simulation indicated that the deformed airfoil performed better in the flow condition with large adverse pressure, besides, the mass flow separation, as well as the dynamic stall, could be reduced by adapting the deformed blade into the system.

Amine Abdelmoula[15] investigated the 2D aerodynamic characteristics of the Bo105 helicopter main rotor with camber airfoils. Specifically, different degrees of trailing-edge camber were employed to the baseline NACA23012 airfoil. During the simulation, the Mach number M varied from 0.2 to 0.7 and the angle of attack α ranged from -10° to 18°. The simulation result evidenced that with the increasing camber higher lift and drag could be achieved, the airfoil with the maximum 6% deformation observed a 30% higher maximum lift coefficient $C_{l,max}$ at $M = 0.4$ and a 63% higher $C_{l,max}$ at M = 0.6. The moderately morphed camber airfoils presented the greatest efficiency augmentation with 30% gain for M = 0.4 at $C_{l,max} = 1.45$ and 120% gain for $M = 0.6$ at $C_{l,max} = 0.85$. Overall, the moderate camber airfoils (airfoils with 2% and 3% downward deflection) showed the greatest performance gains.

Abdelmoula[16] continued to investigate the aerodynamic interaction of a pitching motion with morphing camber actuation of an airfoil. Particularly, the Mach number was set to 0.4 and the pitching angle varied from 0° to 8°, with a pitching frequency of 7 Hz. The result indicated that significant deviations occurred between steady and unsteady airfoil characteristics when combining a pitching airfoil with morphing camber actuation. In addition, a larger deviation in airfoil coefficients (normal force coefficient C_n and pitch moment coefficient C_m) was observed with respect to the increasing of camber frequency. Moreover, if the pitching motion and camber morphing actuation were in phase, the highest C_n amplitudes would be observed. It is worth mentioning that the mean trailing edge deflection and deflection amplitude also had different contributions to the deviations in C_n and C_m.

Therefore, according to the previous investigation, the camber morphing control has great poten-

tials for optimizing the blade flow condition.

1.2.3 Researches on Morphing Cycloidal Rotor

Recently, many experiments and numerical simulations were specifically carried out to investigate the effects of camber morphing on cycloidal rotors.

Liam Ferrier[17] conducted numerical simulations on a two-bladed cycloidal rotor in forward flight, which employed an active continuous leading edge (15% chord length) morphing to the rotating and oscillating NACA0015 airfoils. Particularly, the shape change was only utilized to the blade at the retreating side and the maximum droop was set to 10%. The CFD model was first validated by the experimental case with Re = 1,514,100 and Ma = 0.1198, then the simulation results confirmed that dynamic stall could be mitigated or removed and thus the large loss of lift could be reduced by adapting such morphing control.

Besides, Hailang Zhang and Yu Hu[18] performed simulations on 11 aerofoils with different camber from positive 9% to inverse 9% to study the effect of camber over the revolution. The simulation results verified that the cycloidal rotor with large positive cambered aerofoil (NACA8515) has the lowest hovering efficiency while the rotor with symmetrical aerofoil or small inverse (NACA0015 and inverse NACA2515) reaches the highest efficiency. Moreover, large cambered aerofoil achieves the high aerodynamic performance at the upper part of its trajectory, while the symmetric and inverse cambered aerofoils perform better at the lower part.

Most previous researches are based on the deformed airfoils, whose shape remains fixed during the simulation. The effect of dynamical morphing has not been systematically studied yet. In this project, we made an effort to adapt the dynamical morphing blades to the current cycloidal rotor CFD models. According to the simulation results, by introducing the camber morphing control, the thrust and efficiency could be significantly improved.

2 Methodology

To evaluate the performance of the camber controlled cycloidal rotor, various camber methods are first derived to define the morphing airfoils. After the mesh generation, 2-D URANS simulations are conducted by utilizing the CFD tool OpenFOAM. This chapter illustrates such numerical methodologies, with special attention to the construction of the CFD model of the cycloidal rotor system, which allows the modelling of morphing blades.

2.1 Camber Morphing Concepts

In this work, the airfoil deformation is realized by superimposing different camber line functions onto the baseline symmetrical NACA airfoils. The morphing concepts of NACA camber, trailing edge deflection and leading edge deformation are developed to define the shape of morphing blades.

2.1.1 NACA Camber Concept

The first morphing method utilized is the NACA camber concept. According to the definition[19], the shape of symmetric NACA airfoil (Fig. 2.1) is described by the half thickness function. Its distribution at a given non-dimensional chord position x is defined as:

$$y_t = \frac{t}{0.2}\left(0.2969\sqrt{x} - 0.1260x - 0.3516x^2 + 0.2843x^3 - 0.1015x^4\right) \tag{2.1}$$

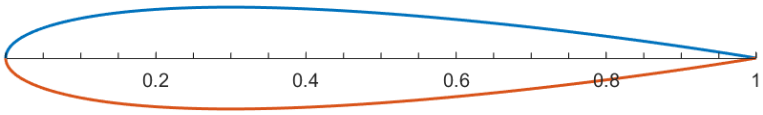

Figure 2.1: Symetric NACA airfoils, NACA0015.

Particularly, for the cambered NACA airfoil (Fig. 2.2), an additional camber line function is required to determine the morphing configuration. Based on the definition of cambered 4-digit NACA airfoil[19], the camber line function is a second order polynomial segment function, denoted as:

$$y_c = \begin{cases} \frac{m}{p^2}\left(2px - x^2\right), & 0 \le x < p \\ \frac{-m}{(1-p)^2}\left(1 - 2p + 2px - x^2\right), & p \le x \le 1 \end{cases} \tag{2.2}$$

where p represents the position of maximum camber as percentage of the chord, m stands for the maximum degree of deformation.

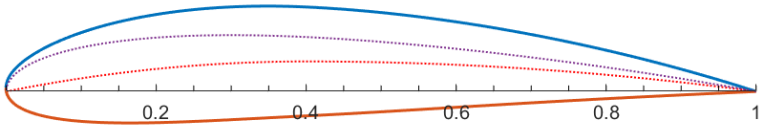

Figure 2.2: Cambered NACA airfoils, NACA4415.

As shown in Fig.2.2, the cambered airfoil shape is modelled up by overlaying the thickness distribution (purple dash line, which is identical with the thickness distribution of the symmetric airfoil) onto the camber line function (red dash line). The coordinates of the upper and lower surface of the cambered NACA airfoils can be calculated respectively by[19]:

$$\begin{aligned} \text{Upper:} \quad & x_u = x - y_t \sin\theta, \quad y_u = y_c + y_t \cos\theta \\ \text{Lower:} \quad & x_l = x + y_t \sin\theta, \quad y_l = y_c - y_t \cos\theta \end{aligned} \tag{2.3}$$

where θ indicates the slope of the camber line at each position, derived as:

$$\theta = \arctan\left(\frac{dy_c}{dx}\right) \tag{2.4}$$

A wide range of cambered NACA airfoils are modelled by varying the maximum degree of camber m and the location of the maximum morphing p .

2.1.2 Trailing And Leading Edge Deformation Concepts

Moreover, based on the concept of cambered NACA airfoil, more generalized morphing methods can be derived efficiently by introducing different polynomial camber line functions into the system.

According to the previous research, airfoils with trailing edge deformation[16] and dynamically drooped leading edges[14] have the great potentials to significantly reduce or eliminate the dynamic stall and the massive flow separation. Therefore, the investigation regarding the effect of trailing and leading edge deformation are included in this project.

Specifically, the trailing edge deformation is first achieved by overlapping a third order polynomial shape function[20] to the trailing edge section of baseline configuration. The camber line function is denoted as:

$$y_c = \begin{cases} 0, & 0 \le x < p \\ \frac{-m}{(1-p)^3}(x-p)^3, & p \le x \le 1 \end{cases} \tag{2.5}$$

where p represents the non-dimensional start location of trailing edge morphing and m denotes the degree of maximum camber. Different airfoils with deformed trailing edge are shown in Fig. 2.3.

(a) $p = 0.4$, $0 < m \leq 16\%$

(b) $p = 0.6$, $0 < m \leq 16\%$

(c) $p = 0.8$, $0 < m \leq 10\%$

Figure 2.3: Airfoils with morphing trailing edge.

Subsequently, the leading edge deformation can be achieved by applying a similar third order polynomial segment function (2.6), which can be expressed as:

$$y_c = \begin{cases} \frac{-m}{p^3}(p-x)^3, & 0 \leq x < p \\ 0, & p \leq x \leq 1 \end{cases} \tag{2.6}$$

to the leading edge section of the symmetric NACA airfoil. In this situation, p denotes the non-dimensional end location of leading edge morphing and m indicates the maximum camber degree. Note that only the first p in Eq.(2.6) fraction of the chord is deformed, the rest part remains fixed. Different airfoils with morphed leading edge deflection are shown in Fig. 2.4.

A wide range of morphing configurations with cambered leading and trailing edge can be efficiently modelled by adapting different values of p and m in the camber line functions.

2.2 Case Description

A series of 2D incompressible URANS numerical simulations are conducted on the cycloidal rotor systems with morphing blades by utilizing the open-source CFD tool OpenFOAM.

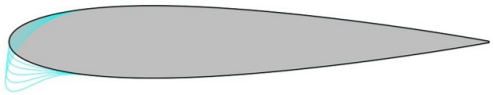

(a) $p = 0.2,\ 0 < m \leq 12\%$

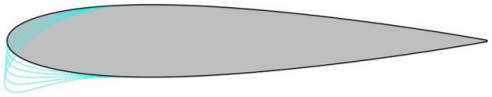

(b) $p = 0.3,\ 0 < m \leq 12\%$

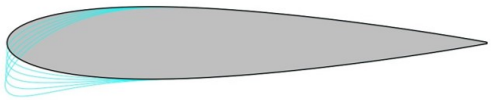

(c) $p = 0.4,\ 0 < m \leq 12\%$

Figure 2.4: Airfoils with morphed leading edge.

2.2.1 Numerical Setting

All the simulations are iteratively solved by the PIMPLE algorithm in OpenFOAM, which is a pressure-based solver and can be regarded as a combination of Pressure Implicit with Splitting of Operator (PISO) solver and Semi-Implicit Method for Pressure-Linked Equations (SIMPLE) solver.

The size of the time step in the simulation Δt is limited by the Courant number, denoted as

$$C = \frac{u\Delta t}{\Delta x} \tag{2.7}$$

where Δx is the spacing of the grid. Generally, convergence is only possible when the Courant number is under 1 for explicit solvers to satisfy the CFL condition. Since the PIMPLE algorithm iterates the solution of pressure-velocity coupling within a time step for the transient case, larger time step Δt and higher Courant number (consistently above 1) are allowed in the simulations. Besides, Δt is set as 0.00005 s in this work, which means 20 time steps are solved for every azimuth degree. Consequently, the Courant number varies between 1 to 2 for all simulations.

The convergence and stability of the PIMPLE algorithm can be improved by increasing the number of correctors and reducing the relaxation factor. The setting of PIMPLE is consistent with the setting of Florian Zimmer's case[21], see Appendix I.

Moreover, $k - \omega - SST$ model is utilized in this work to solve the turbulent closure problem, due to its highly accurate prediction of the dynamic stall phenomena for oscillating airfoils[17]. In detail, it is a 2-equation eddy-viscosity model, which can be regarded as a blend of $k - \epsilon$ model for the free stream and $k - \omega$ model for the near-wall region. Consequently, it benefits from the enhanced

near-wall treatment of $k-\omega$ model and bypasses the free stream sensitivity of the $k-\epsilon$ model. Since wall functions are not used in this turbulence model, a relatively fine mesh resolution is required for the near-wall region.

Relevant numerical information of the rotor system in CFD simulation is summarized in Table 2.1.

Simulation Type	2D URANS	**Angular Velocity**	$17.453 rad/s$
Turbulence Model	$k-\omega-SST$	**Reynolds Number**	$72,000$
Baseline Airfoil	NACA0015	**Courant Number**	$(1,2)$

Table 2.1: Parameters of the rotor system in CFD simulation.

Besides, the selection of spatial and temporal discretization methods plays an essential role in the accuracy and stability of the simulation results. In this project, the discretizations are approximated with second-order schemes, which can be specified as:

- The temporal discretization scheme **ddtSchemes** is set to *backward*, a time dependent second order (implicit) scheme.
- The discretization scheme of the convective terms **divSchemes** is set to $Gausslimited Linear V$ 1.0, which is an accurate and stable numerical scheme with second-order accuracy.
- The discretization scheme of the diffusive terms **divSchemes** is set to *Gausslinearlimited*, which is generally employed for meshes with low non-orthogonality.
- The discretization scheme of the gradient terms **gradSchemes** $cellLimitedleastSquares$ 1, the gradient limiter is implemented here to increase the stability.

More information on the setting of numerical schemes is included in $fvSchemes$ (see Appendix I).

2.2.2 Blade Camber and Motion Definition

The rigid body motion of blade is the combination of revolution around the centre of rotor system and pitching around its pivot point. Both of them are introduced into the system as *solidBody* motions, which are defined in the $dynamicMeshDict$ (see Appendix III) in OpenFOAM.

The schematic of the coordinate system and rotor parameters are shown in Fig. 2.5, where θ represents the pitching amplitude and ψ indicates the azimuth angle, denotes as

$$\psi = \frac{2\pi t}{T} \tag{2.8}$$

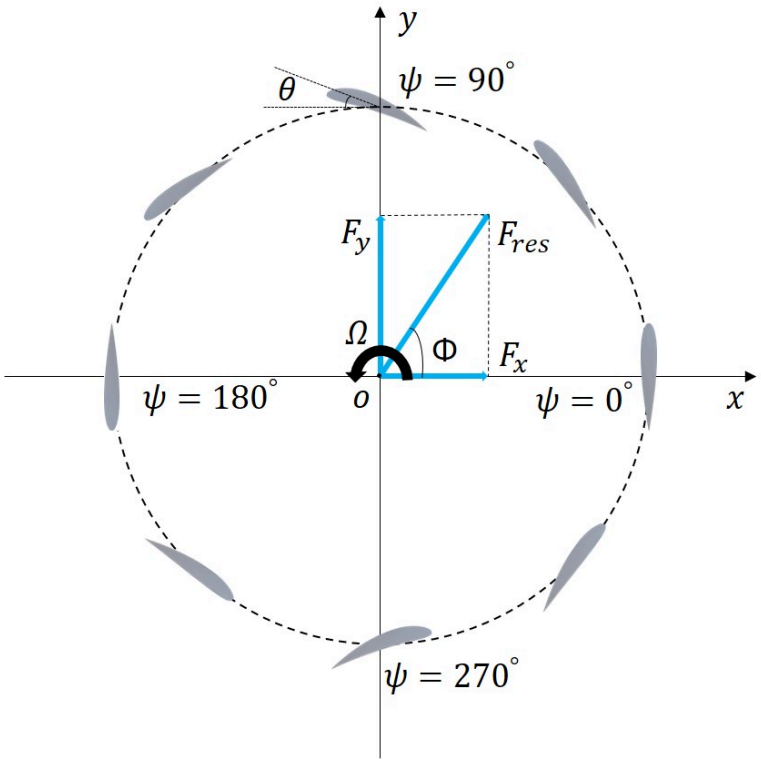

Figure 2.5: Definition of coordinate system and parameters.

where T represents the time period of the revolution. From the figure, the blades are rotating counterclockwise, and the positive vertical and side-ward force directions follow the positive x-axis and y-axis directions.

Generally, for conventional cycloidal rotors, the thrust is mainly generated by the pitching motion of the blade. In this work, the dynamically morphing configuration of the airfoil contributes to lift generation as well. Moreover, both the pitching amplitude θ_t and camber morphing degree m_t vary periodically over the azimuth angle, as shown in Fig. 2.6.

Specifically, a sinusoidal pitching motion is defined in the system, which is expressed as

$$\theta(t) = \theta_0 \sin(\psi) \tag{2.9}$$

where θ_0 stands for the maximum pitching amplitude (set as 20° for all cases). The pitching motion is symmetrical between the upper and lower half, therefore, when the blade is at the position of $\psi = 0°$ *and* 180°, the pitching angle is 0. When the blade is at the top ($\psi = 90°$) or bottom ($\psi = 270°$) of the trajectory, the pitching angle will reach its maximum amplitude. In addition, the increment in pitching angle means the blade pitching is in the counterclockwise direction while the decrease of θ stands for the clockwise pitching.

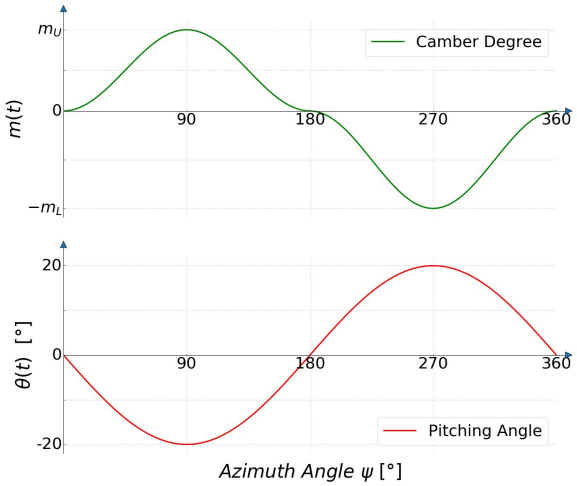

Figure 2.6: Periodical pitching and camber morphing setting.

Besides, the camber morphing of the blade shows a similar behavior, the periodical variation of camber degree $m(t)$ is is governed by a half-cosine function(2.10):

$$m(t) = \begin{cases} \frac{m_U}{2}[\cos(2\psi) + 1], & 0° \leq \psi < 180° \\ -\frac{m_L}{2}[\cos(2\psi) + 1], & 180° \leq \psi < 360° \end{cases} \tag{2.10}$$

where m_U and m_L represent the maximum camber degree for the upper and lower half respectively. Specifically, as shown in Fig. 2.6, the value of $m(t)$ is negative for the lower part, which indicates the inverse camber is applied in this section. In addition, the inverse cambered aerofoil is symmetrical about the blade chord to the cambered one with the corresponding positive camber degree.

Particularly, at the position of $\psi = 0°$, the blade remains symmetric. As the blade rotates, the airfoil will be gradually deformed and reach the maximum camber for the upper part m_U at the top position of its trace. Afterwards, the cambered configuration will recover and return slowly to the symmetrical shape in the following 90°. Furthermore, for the lower part of the trajectory, the morphing process behaves the same as the upper part. Especially, the airfoil will change its camber direction and reach the maximum morphing degree of inverse camber m_L at the bottom of its trace, then the deformed configuration will revert to the symmetrical airfoil at the position $\psi = 360°$.

2.2.3 Realization of Blade Morphing

The blade deformation is realized by superimposing a predetermined displacement field on the original coordinates of the points on the symmetric blade surface. Specifically, the predetermined

displacement saved as *pointDisplacement* file is introduced into the system as the boundary data during the simulation.

In OpenFOAM, **timeVaryingMappedFixedValue** (see Appendix III) is the boundary condition that can read boundary data from files and interpolates the values from a set of supplied points in space and time. Based on this feature, **timeVaryingMappedFixedValue** is constrained as the boundary condition for pointDisplacement in this work to load the predetermined displacement files from the *constant/boundaryData* folder for every time step.

According to the aforementioned camber line functions ((2.2) (2.5) and (2.6)) and the camber degree variation(2.10), the displacements for points are calculated and saved for every time step by using Python scripts. The generation process of relevant files can be summarized as follow:

- A series of points on the baseline profile (NACA0015) are selected to define the shape of the airfoil. The coordinates of the points are saved as *points* file in the *constant/boundaryData* directory.
- The camber degree of each position is determined by the half cosine function (2.10). Accordingly, the coordinate of the morphing blade is calculated based on the predetermined camber function defined in section 2.1.
- The difference between the coordinate of the cambered and symmetric baseline airfoil is calculated and termed as the original displacement. Subsequently, the original displacement is projected to the current position of the rotating and oscillating blade according to the azimuth angle ψ and pitching angle θ.
- The projected displacement of each point is calculated and written in the *pointDisplacment* file for every time step in the *constant/boundaryData* directory.

2.2.4 Realization of Mesh Morphing

The control of the mesh morphing during the simulation is realized by the *dynamicMeshDict* file in the *constant* folder. The *dynamicMotionSolverFvMesh* type of solver is selected to deform the mesh around the morphing blade and provide feedback to the fluid simulation. Then the meshing motion is calculated based on the pressure on those moving boundaries.

Moreover, the diffusion of mesh deformation has a significant impact on the morphing process, which is controlled by the mesh diffusivity in the *dynamicMeshDict*. In this research, various type of mesh diffusivity ($uniform$, $quadratic\ inverseDistance$, and $inverseDistance$) are tested for the cases with camber morphing blades (NACA camber concept with $p = 0.4, m = 10\%$).

For cases with *uniform* diffusivity, all cells in the computational domain are handled uniformly, namely, they are deformed with the same ratio.

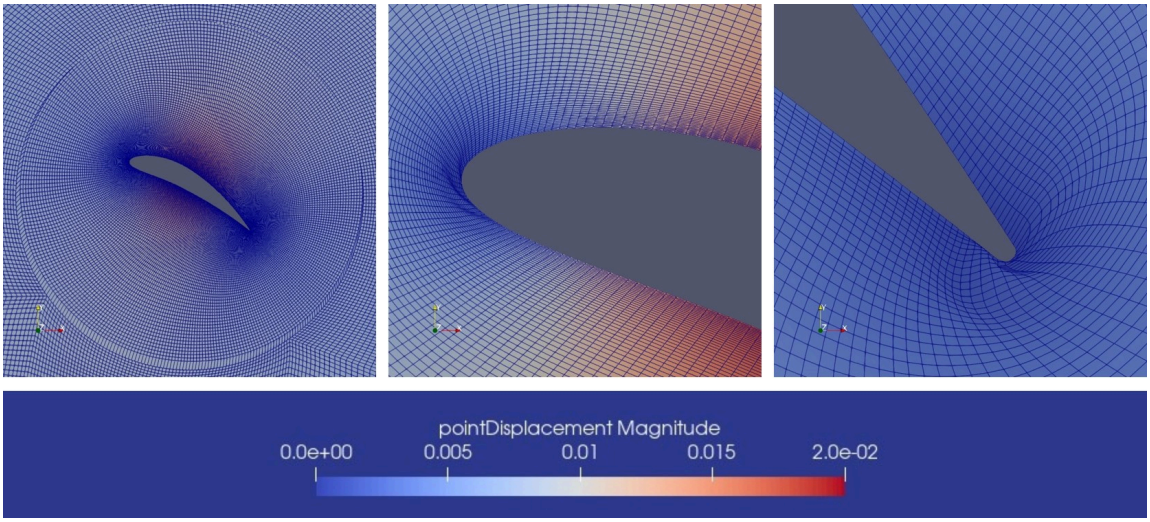

Figure 2.7: Mesh deformation for the case with uniform diffusivity.

The simulation results of pointDisplacement are shown in Fig. 2.7. From the figure, severe mesh distortion is observed near the leading edge and trailing edge. In addition, the meshes at the AMI boundary are compressed or stretched due to blade deformation. Moreover, as the degree of camber increases, more severely deformed grids will be observed near the AMI interface and the morphing blade surface, which will eventually lead to the collapse of the simulation.

Furthermore, the cases with *quadratic inverseDistance* diffusivity show best results as depicted in Fig. 2.8. In this case, the diffusion coefficient is inversely proportional to the square of the distance to the specified boundary. Specifically, both the morphing surfaces and the AMI interfaces should be set as the specified boundaries to ensure that the grids close to the boundaries have a rather large value of mesh diffusivity. By doing so, the mesh can follow the deformation of the blade and the AMI surface can maintain its shape during the morphing process. As a consequence, the grid deformation is constrained within a slightly smaller region close to the morphing surface when compared with the situation under *inverseDistance* diffusivity, as shown in Fig. 2.9. Therefore, the *quadratic inverseDistance* diffusivity is selected to control the deformation process for all simulations with camber morphing blades.

More settings of morphing control and physical definition of rigid body motion are shown in Appendix IV.

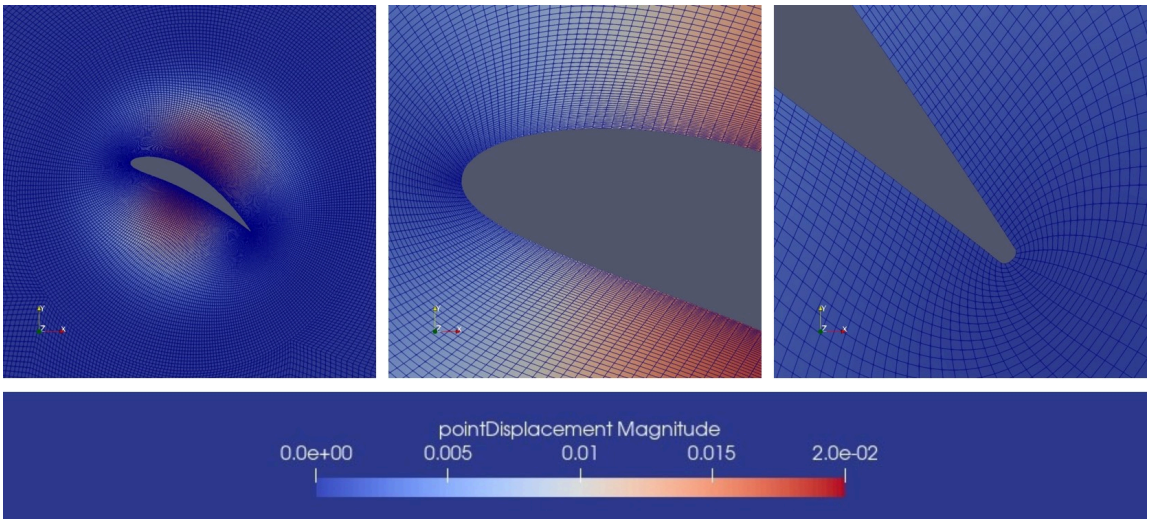

Figure 2.8: Mesh deformation for the case with quadratic InverseDistance diffusivity.

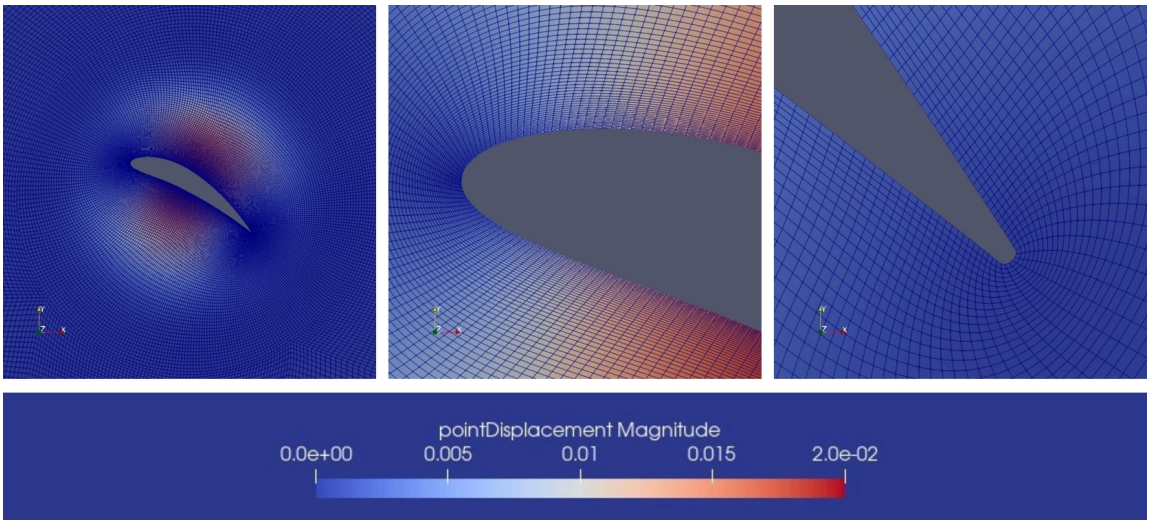

Figure 2.9: Mesh deformation for the case with InverseDistance diffusivity.

2.3 Mesh Strategy

The spatial discretization strategy has a great influence on the accuracy of the simulation. In this research, a structured mesh is constructed for the whole computational domain by using the mesh tool Pointwise.

2.3.1 Grid Generation

The initial rotor system investigated in this work consists of two baseline NACA0015 airfoils, with chord length $c = 0.2\ m$, rotation radius $r = 0.32\ m$, and blade span $b = 0.8\ m$. The aspect ratio and chord-by-radius ratio of the blades are selected, according to Kellen's optimization analysis[13]. Note that only one cell is extruded in z-direction since 2-D simulations are conducted in this work.

Geometrical information for mesh generation is summarized in the Table 2.2.

Number of Blades	2	Baseline Airfoil	NACA0015
Chord Length	0.2 m	Rotation Radius	0.32 m
Blade Span	0.8 m	Pitching Axis	50% of the chord

Table 2.2: Geometrical information of the rotor system.

From Fig. 2.10, a boundary fitted structured mesh is modelled around the blades. By utilizing such a structured mesh, the initial spacing, growth rate, and total height of the boundary layer can be easily controlled. In addition, the radius of the whole domain is 50 times the blade chord length. Consequently, the far-field computational boundary condition[22], which is generally employed to solve the differential equations in exterior domains, can be applied to the outer boundary patch termed **farFields**, in this research.

Detailed mesh generation topology around the morphing blade is illustrated in Fig. 2.11. The entire mesh will revolve around the centre of the domain, while the pitch motion around the pivot point is only applied to a small circular area around the blade, which is termed *Pitching Domain*.

As shown in Fig. 2.11(a), the pitching domain and the non-pitching zone are separated by the Arbitrary Mesh Interface (**AMI**), which is particularly useful to separate stationary and rotating geometries. Note that **cyclicAMI** type of boundary conditions are introduced here to enable the adjacent interfaces to match with each other under the assumption that they are physically connected. In addition, a refined leading edge (Fig. 2.11(b)) and a rounded trailing edge (Fig. 2.11(c)) are employed in the system for a better morphing performance.

Moreover, the **BaseAndTop** are the front and back patches whose normal is aligned to the z-axis. Since 2-D simulations are performed in this research, no solution is required for these two patches.

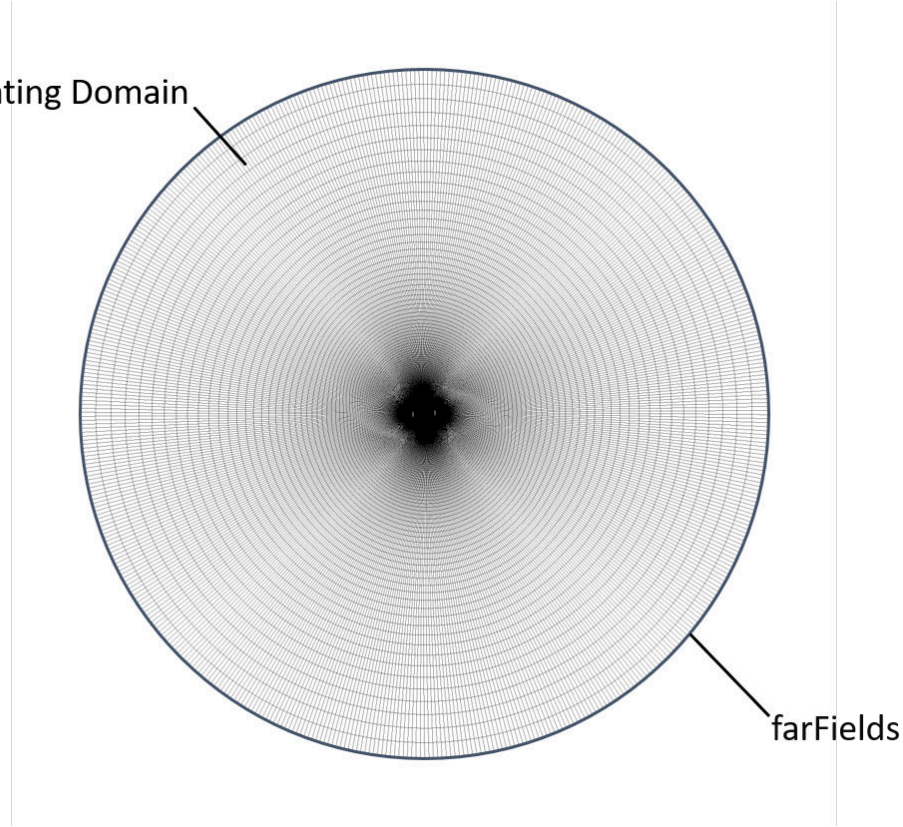

Figure 2.10: Mesh of the entire computational domain.

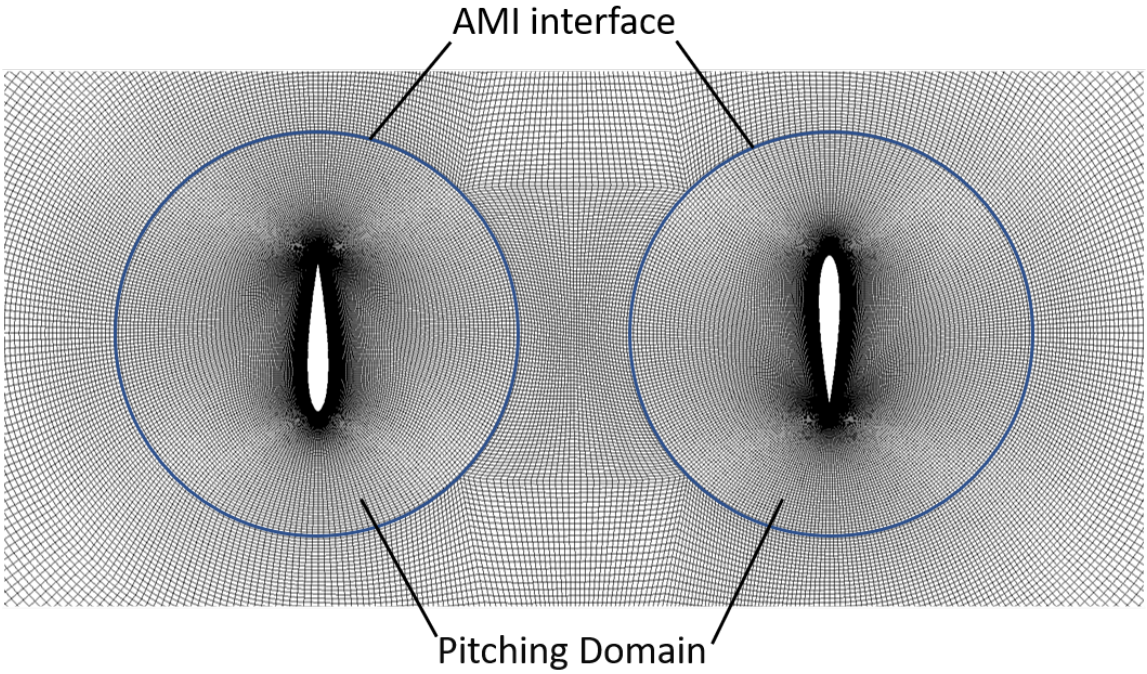

(a) AMI interface and pitching domain

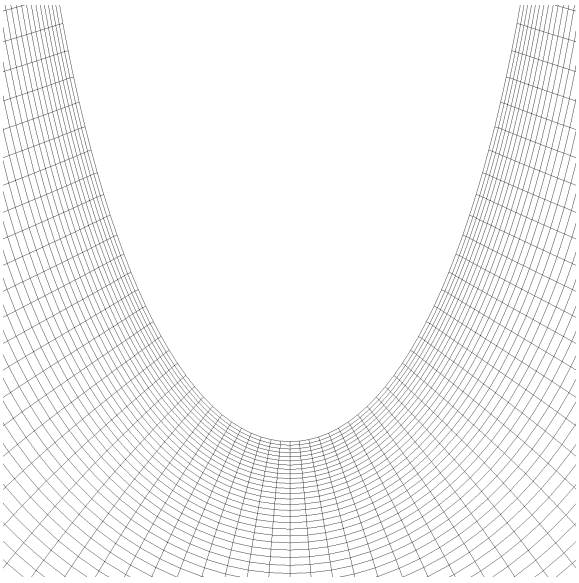

(b) Leading edge grids

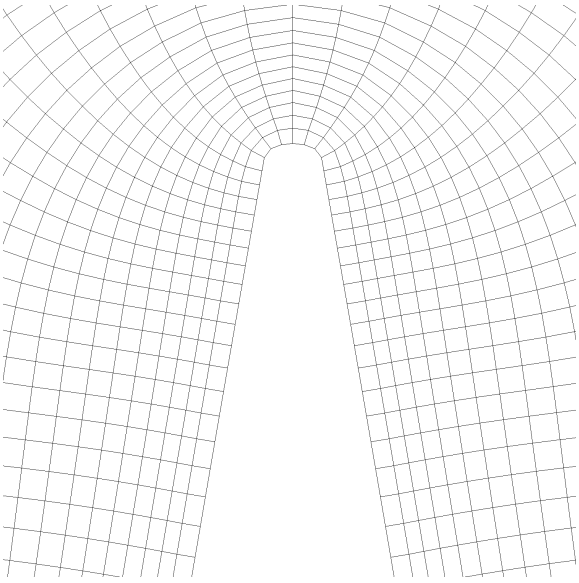

(c) Trailing edge grids

Figure 2.11: Mesh topology for the 2-blade rotor system.

Accordingly, the *empty* type of boundary condition is employed for such reduced dimensions cases.

Boundary conditions of the above-mentioned patches in the rotor system are summarized in Table 2.3.

	farfields	**AMI**	**BaseAndTop**
U	pressureInletOutletVelocity	cyclicAMI	empty
p	totalPressure	cyclicAMI	empty
k	inletOutlet	cyclicAMI	empty
ω	inletOutlet	cyclicAMI	empty
ν_T	calculated	cyclicAMI	empty

Table 2.3: Boundary conditions for the patches

2.3.2 Grid Resolution

To analyze the effect of grid resolution, a qualitative assessment is conducted on the grids with different initial cell heights (initial spacing). In details, the baseline test cases (no camber) are running on coarse, medium, and fine grids. More information of the meshes is described in Table 2.4.

	initial spacing	y^+ value	cell count	blade dimension
Coarse mesh:	2×10^{-4}	< 8	123,408	305
Medium mesh:	2×10^{-5}	< 4	141,322	305
Fine mesh:	1×10^{-5}	< 1	238,505	405

Table 2.4: Information of the mesh construction.

For the morphing blades **wing1** and **wing2**, the selection of the boundary condition depends on the y^+ value distribution on the surface of the airfoil. In detail, if the y^+ of the first cell is less than 1, a low Re version of boundary conditions for turbulence properties k, ω, and ν_t is compulsory to provide a wall constraint on the quantities. However, if the first cell height is in the region of $30 < y^+ < 200$, the high Re version of boundary should be employed for the blades instead. The exact boundary condition for velocity, pressure, and turbulence quantities are described in Table 2.5. Note that in the test case for grid analysis, both low Re and high Re boundary conditions are utilized.

In particular, the coarse and medium mesh have a maximum value of $y^+ = 8$ and $y^+ = 4$ respectively, which are used in the test case employing high Re boundary conditions. For the case with

	High Re BC	Low Re BC
U	movingWallVelocity	movingWallVelocity
p	zeroGradient	zeroGradient
k	kLowReWallFunction	kqRWallFunction
ω	omegaWallFunction	omegaWallFunction
ν_T	nutLowReWallFunction	nutkWallFunction

Table 2.5: Boundary conditions for the morphing surface.

	Thrust [N]	Thrust Angle [Deg]	Power [W]		Power Loading [N/W]		Figure of Merit [-]	
CM_HighRe	0.84	96.43	1.65		0.51		0.42	
MM_HighRe	0.85	94.65	1.52	-7.88%	0.56	+9.8%	0.46	+9.52%
FM_HighRe	0.84	95.08	1.44	-12.7%	0.58	+13.7%	0.48	+14.3%
FM_LowRe	0.84	94.71	1.45	-12.1%	0.58	+13.7%	0.48	+14.3%

Table 2.6: Aerodynamic prediction of baseline case with difference grids.

the fine mesh, the y^+ value is less than 1 over the whole airfoil. Consequently, both high Re and low Re boundary conditions for surface are utilized to study the influence of the selection of boundary conditions.

Furthermore, baseline cases (no camber) with aforementioned grids and boundary conditions are conducted, the aerodynamic predictions of these cases are summarized in Table 2.6, where CM, MM, and FM indicate coarse mesh, medium mesh, and fine mesh, respectively. Besides, HighRe and LowRe represent high Re and low Re boundary conditions, respectively. From the table, all cases exhibit almost the same averaged resultant thrust values and the difference between required power is less than 13%. Moreover, the baseline case with finer grids achieves an increase of power loading and figure of merit. Since this work is a qualitative research and only URANS simulations are implemented, then the difference of 15% is still acceptable.

Furthermore, the grids are applied to the case with cambered airfoils as well. The simulation results indicate that, for the case with fine mesh, the girds closed to the surface would deteriorate and lead to the simulation collapse when the camber degree is reaching 2%. As for the test cases with medium mesh, around 12% of morphing could be achieved. Moreover, around 20% of deformation could be realized for the test case of the coarse grid. According to the results, it is confident to conclude that more camber morphing could be realized for the case with Coarse mesh.

Based on the above study of baseline and camber morphing cases, more camber is expected to be introduced to the rotor system to obtain a more convincing result, therefore, the coarse mesh is selected for further simulations to ensure that the grid closed to the morphing surface is not severely distorted.

The y^+ distribution along the normalized chord for the baseline case with coarse mesh at the position $\psi = 0°$ is shown in Fig. 2.12. From the figure, the y^+ values are always below 6 in this situation. Moreover, during the entire cycle, the maximum y^+ value at the blade surface varies between 1 to 8.

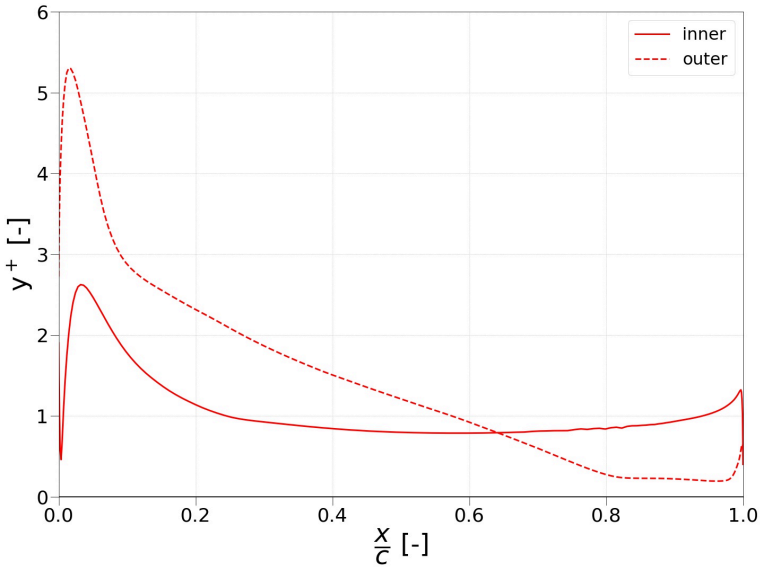

Figure 2.12: y^+ distribution along the chord for the baseline case, $\psi = 0°$.

Overall, mesh information over the rotation is obtained by executing the **checkMesh** command. For the test case with cambered NACA airfoils ($p = 0.4, m = 10\%$), where the coarse mesh is adapted, the maximum length ratio is 10.285, the maximum skewness is 0.57, and the maximum mesh non-orthogonality is 33.204 over the rotation, which ensures the effectiveness of the case with cambered geometry during the simulation.

2.4 Aerodynamic Properties

The primary objective of this research is to improve the aerodynamic performance of the cycloidal rotor system with the morphing blades. Therefore, both resultant thrust F_{res}, power P, as well as power loading PL and figure of merit FoM are calculated to evaluate the performance of camber controlled rotor systems. Besides, vertical force F_y, sideward force F_x, and torque M_Z are involved

in the force and power analysis, which are all obtained as outputs of Force Function included in file *controlDict* during the simulation.

2.4.1 Force Analysis

Since the 2D analysis is performed in this work, the grids introduced into OpenFOAM only have one cell in the z-direction. Consequently, a thickness ratio, denoted as μ , is needed to extend the data obtained from the simulation thickness (one cell in the z-direction) to the designed blade span, which can be expressed as

$$\mu = \frac{\text{blade span}}{\text{actual thickness}} = \frac{b}{\Delta z} \tag{2.11}$$

In addition, from the Fig. 2.5, the positive vertical and sideward force is the x-component and y-component of the total thrust. The resultant thrust of the blade F_{res} is calculated with the square root of the x-component and y-component,

$$F_{\text{res}} = \mu\sqrt{F_x^2 + F_y^2} \tag{2.12}$$

Note that F_{x} and F_{y} are the averaged values over the entire cycle. Besides, its angle to the horizontal (x-axis), termed as thrust angle Φ, is calculated by

$$\Phi = \tan^{-1}\frac{F_y}{F_x} \tag{2.13}$$

2.4.2 Power Analysis

The total aerodynamic power of a cyclorotor consists of the induced power, profile power, pitching power, and losses. The actual required power is calculated as the product of the measured torque M_Z and the speed multiplied by the thickness ratio, which is denoted as

$$P = \mu M_Z \Omega \tag{2.14}$$

where Ω represents the *angular velocity*.

Specifically, two types of efficiency are calculated in this work. Firstly, the figure of merit (FoM) is defined as the ratio of the ideal power required in hover state to the actual power required. Unlike the helicopter rotor which calculates the reference area from the swept area $A = 2Rb\pi$, the reference area involved for a cycloidal rotor is the projected area $A_{ref} = 2Rb$. The definition of the ideal power requirement is denoted as

$$P_{ideal} = \frac{F_{res}^{3/2}}{(2\rho A_{ref})^{1/2}} = \frac{\mu^{3/2}(F_x^2 + F_y^2)^{3/4}}{(4\rho R\mu\Delta z)^{1/2}} = \mu\frac{(F_x^2 + F_y^2)^{3/4}}{(4\rho R\Delta z)^{1/2}} \tag{2.15}$$

Generally speaking, FoM can be introduced to predict the overall aerodynamic performance. Specifically, a higher value of the figure of merit indicates a better aerodynamic performance of the rotor system in hover, which can be expressed as

$$FoM = \frac{P_{ideal}}{P} = \frac{P_{ideal}}{\mu M_Z \Omega} = \frac{(F_x^2 + F_y^2)^{3/4}}{M_Z\Omega(4\rho R\Delta z)^{1/2}} \tag{2.16}$$

Another employed dimensional quantity is the power loading PL, which represents the minimum power required for the system with a given weight, expressed as

$$PL = \frac{F_{res}}{P} = \frac{\mu(F_x^2 + F_y^2)^{1/2}}{\mu M_Z \Omega} = \frac{(F_x^2 + F_y^2)^{1/2}}{M_Z\Omega} \tag{2.17}$$

The following chapters present a detailed assessment of the effect of various camber methods on aerodynamic performance by comparing the aerodynamic parameters defined in this section.

3 Results of Cambered NACA Airfoil

This chapter investigates the aerodynamic performance of the cycloidal rotors with cambered NACA airfoils. Particularly, the effect of camber degree m, the effect of position of maximum camber p, and the asymmetric camber effect are illustrated in this chapter.

3.1 Effect of Maximum Degree of Camber Morphing

First of all, the effect of camber degree for the NACA camber concept is studied. As illustrated in Fig. 3.1, the maximum camber degree varies from 0% to 16% of the chord length, and the baseline case with symmetric airfoils (NACA0015) is denoted as 0% NACA camber in the section. Besides, for the cambered NACA airfoils, the locations of the maximum camber morphing are occurring at the position 40% of the normalized chord, i.e., $p = 0.4$. Moreover, the maximum camber degrees for the upper (m_U) and lower (m_L) half are set to be identical.

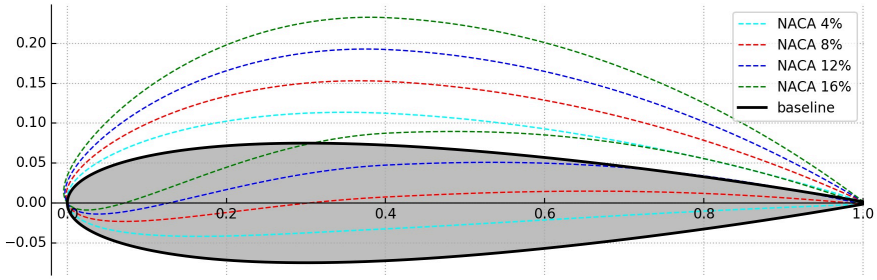

Figure 3.1: Camber NACA airfoils, $p = 0.4$.

3.1.1 Force and Power Analysis

The variation of resultant thrust and power over the camber degree is shown in Fig. 3.2. From the figure, significantly higher resultant thrust and power levels can be observed with the increasing camber degree. For the cases with 4%, 8%, 12%, and 16% cambered NACA airfoils, 18.0%, 36.8%, 60.4%, and 77.5% higher thrust are observed, respectively. Meanwhile, 6.74%, 25.7%, 48.1%, and 65.0% more power are required by the blades. Furthermore, the gain in thrust is always greater than the power increment, which leads to a better efficiency performance for the case with cambered NACA airfoils.

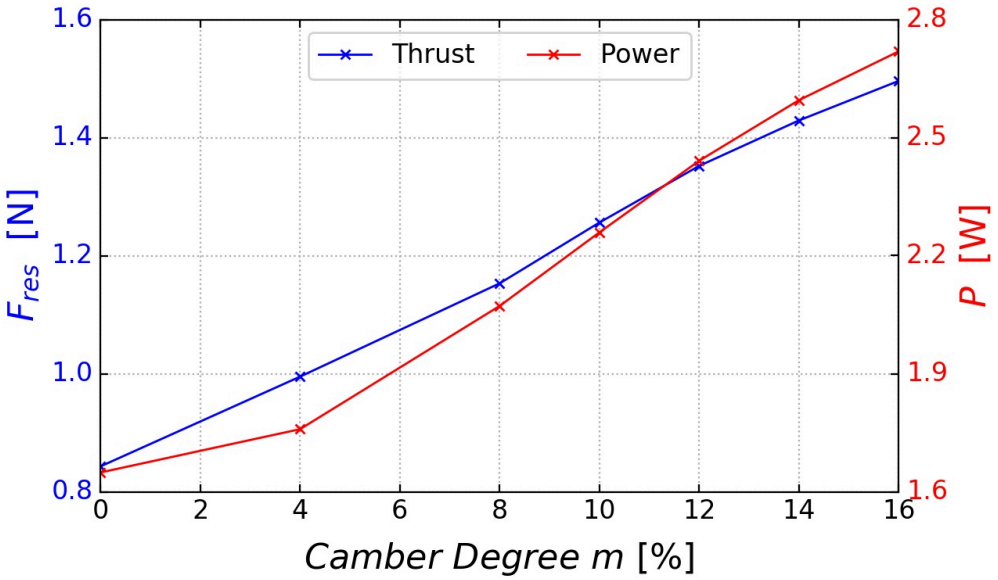

Figure 3.2: Thrust and power prediction vs. NACA camber degree, $p = 0.4$.

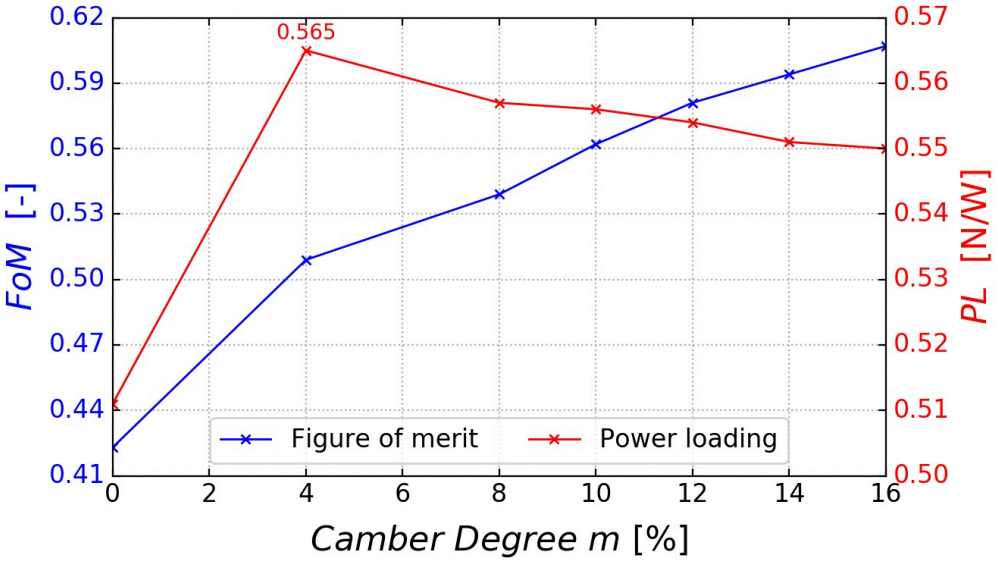

Figure 3.3: Efficiency prediction vs. NACA camber degree, $p = 0.4$.

The results of figure of merit and power loading versus camber degree are described in Fig. 3.3. As depicted in the figure, for the case with camber NACA airfoils, a higher value of FoM and PL are obtained. The value of power loading would reduce with respect to the increasing camber degree. Specifically, the reason for this tendency is that in all cases with cambered airfoils, thrust increases more than power, however, as the camber degree increases, the gap in increments gradually narrows. As a consequence, the value of power loading will gradually decrease. Meanwhile, the variation of figure of merit over the camber degree exhibits an opposite trend, and its value increases as more camber are introduced into the system. Besides, in the case of 16% NACA camber, the FoM could reach the value of 0.61, which is the highest value that can be achieved in this work.

Figure 3.4 illustrates the variation of vertical force and required power for one blade for case with cambered NACA airfoils. From Fig. 3.4(a), a significantly higher lift level is observed over the rotation. Besides, both the symmetric and cambered NACA airfoils have identical thrust variation patterns, the thrust is mainly obtained in the intervals near $\psi = 90°$, $\psi = 225°$, and $\psi = 310°$. Moreover, with the increase of camber degree, a higher peak value of vertical thrust can be observed near the top and lower left part of the trajectory. It is particularly noteworthy that in the lower right part of the rotation, i.e., $270° < \psi < 320°$, the lift even exceeds the previous peak and reaches its maximum value during the entire cycle. The significant gain in thrust could be explained by the increase of downwash velocity and the change of local flow condition with the increasing camber degree.

The results of the required power are shown in Fig. 3.4(b). Generally speaking, a higher thrust generation means more energy consumption is required. Therefore, the power distribution is consistent with the thrust change shown in Fig. 3.4(a). Specifically, due to the formation and development of the leading edge vortex, the baseline airfoil exhibits a relatively higher value of required power at the position $120° < \psi < 180°$. In addition, since the development of the vortex and its detachment occur on the outer surface of the blade, significantly more power is required near the lower end, i.e., $220° < \psi < 310°$, for cases with a large NACA camber degree.

A detailed illustration of the force and power analysis would be presented in the following sections.

3.1.2 Flow Field Visualization

The induced velocity in the negative y-direction is termed downwash velocity. It varies the effective angle of attack (AoA) of the blade and changes the incident flow velocity. Therefore, it has a great impact on the aerodynamic performance of the rotor system.

As shown in Fig. 3.5, the larger the camber degree is, the more intensified and concentrated

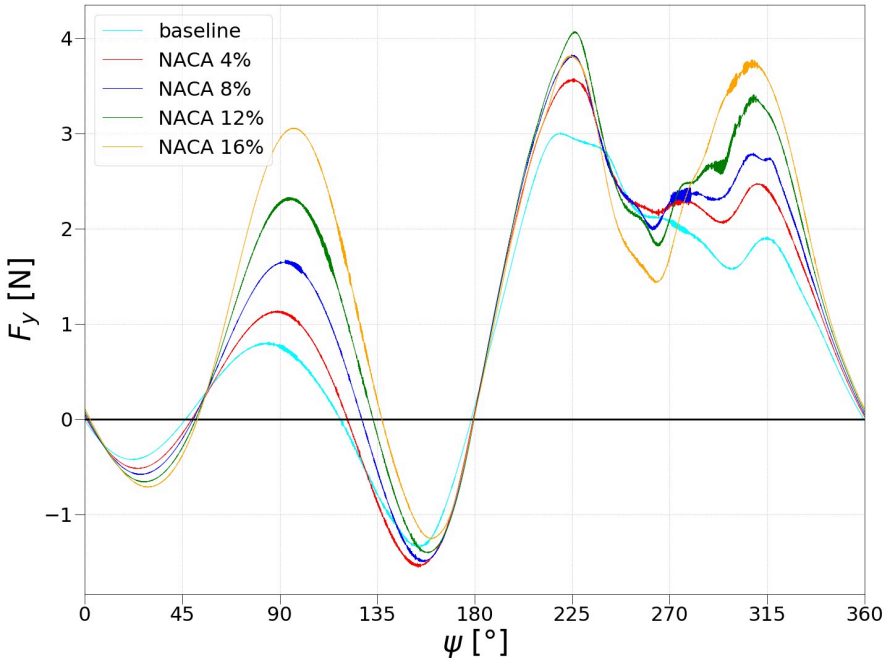

(a) Vertical force

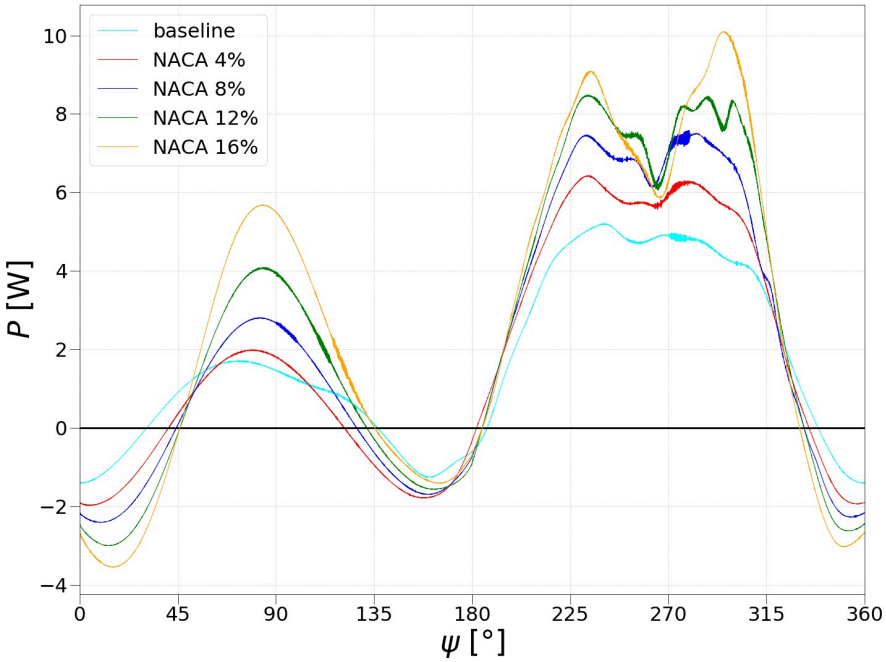

(b) Required power

Figure 3.4: Vertical thrust and power distribution for one blade with different NACA camber degree.

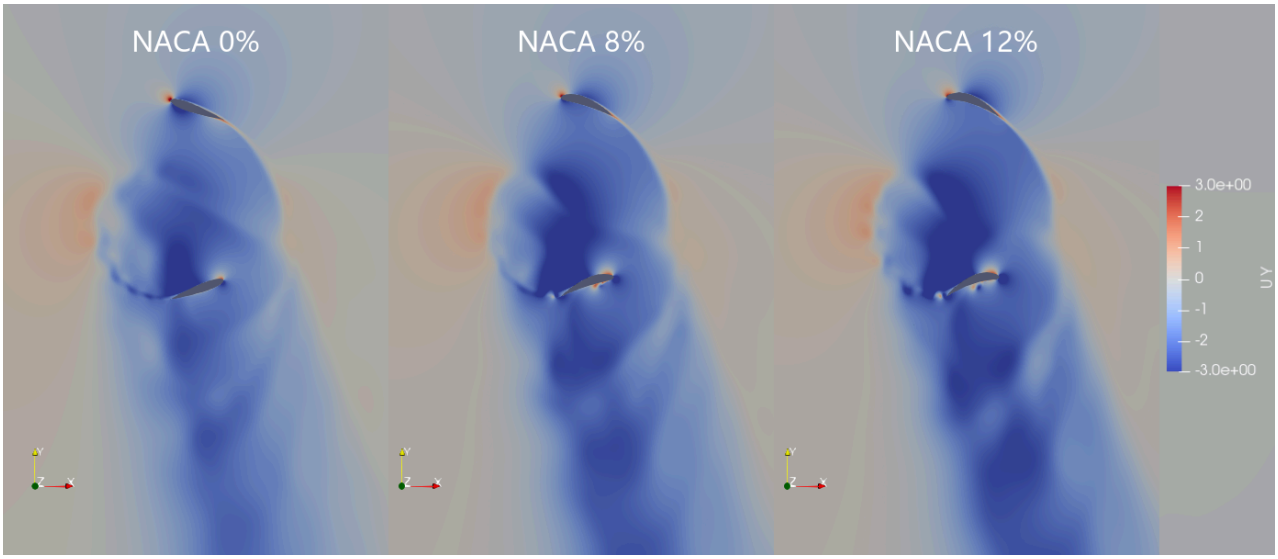

Figure 3.5: Downwash velocity for cases with different NACA camber degree.

downwash velocity could be observed. In addition, the local downwash velocity possesses the same magnitude as the tangential velocity of the linear rotation of the blade for the cases with cambered airfoils. Consequently, more reduction in the effective AoA and change in inflow velocity could be expected for the case with large camber when the blade is passing through the lower end of its trace.

The vorticity contours of the case with cambered NACA airfoils are shown in Fig. 3.6 and 3.7.

It is evident that the case with cambered NACA aerofoils show a better aerodynamic performance when the blade is moving through the upper part of its trace. Specifically, for the baseline case, the leading edge vortex (LEV) would appear near the position $\psi = 120°$. Subsequently, the vortex develops rapidly and spans the entire surface. However, in the case of cambered NACA airfoils, the formation of the vortex is eliminated. Thus the flow field condition in the upper half is optimized by cambered NACA airfoils.

When the blade is in the lower half of the trajectory, a completely different behaviour would be expected. Particularly, for the baseline case, fluid flows smoothly on the surface of the symmetric airfoils and is always attached. However, in the case of large NACA camber, the presence of vortex and its detachment at the outer side (pressure side) of the oscillating blade as well as the distorted boundary vorticity could be observed near the lower end, i.e., $260° < \psi < 310°$, due to the cambered configuration and the intensified downwash effect. As a result, reduction in lift and increasing pressure loss could be expected for the case with cambered NACA airfoils near the lowest point of its cycle.

More information on the unsteady phenomena and the corresponding effect on the pressure distribution and vertical thrust are introduced in the next section.

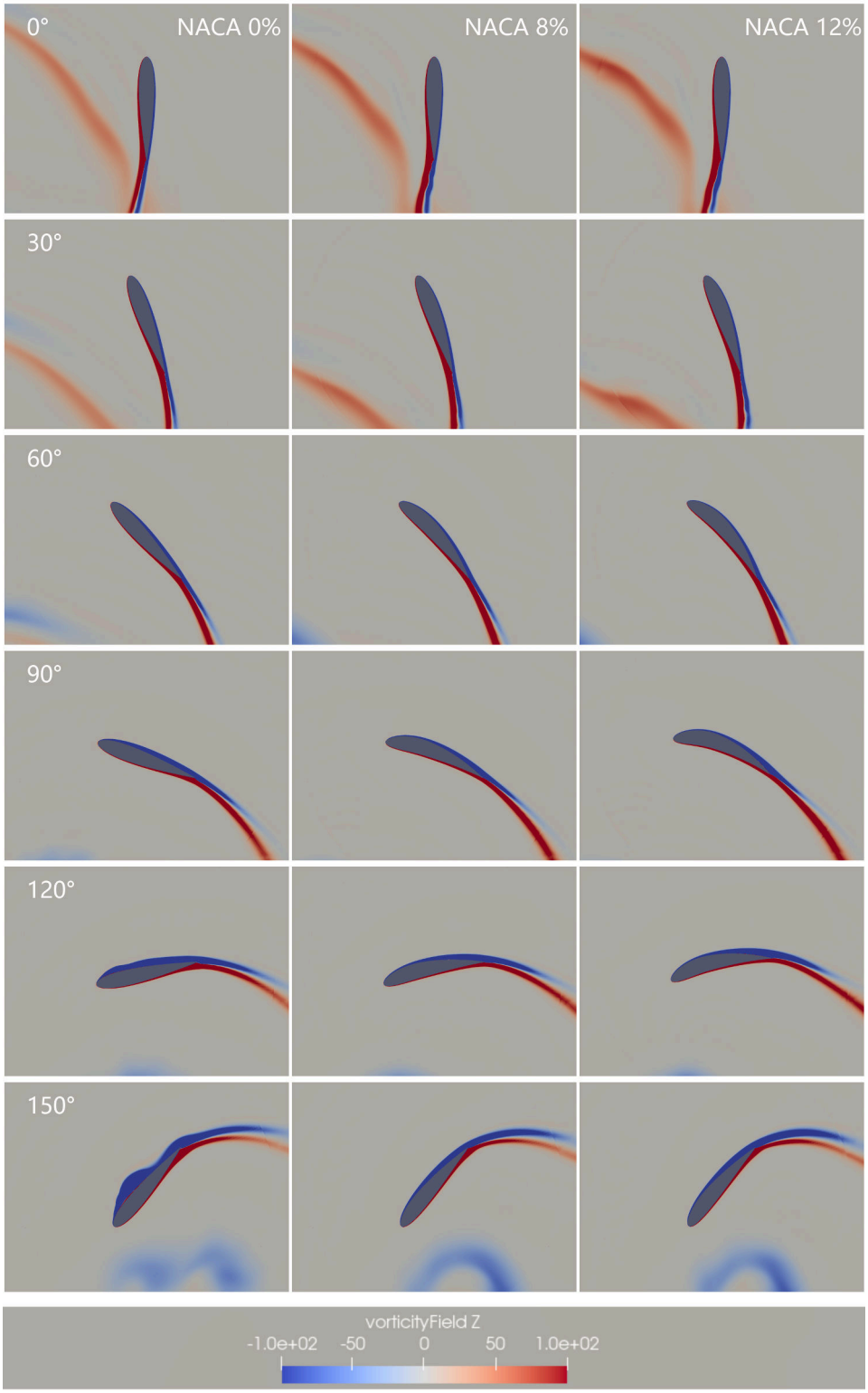

Figure 3.6: Vorticity field for cases with different NACA camber degree, $0° < \psi < 150°$.

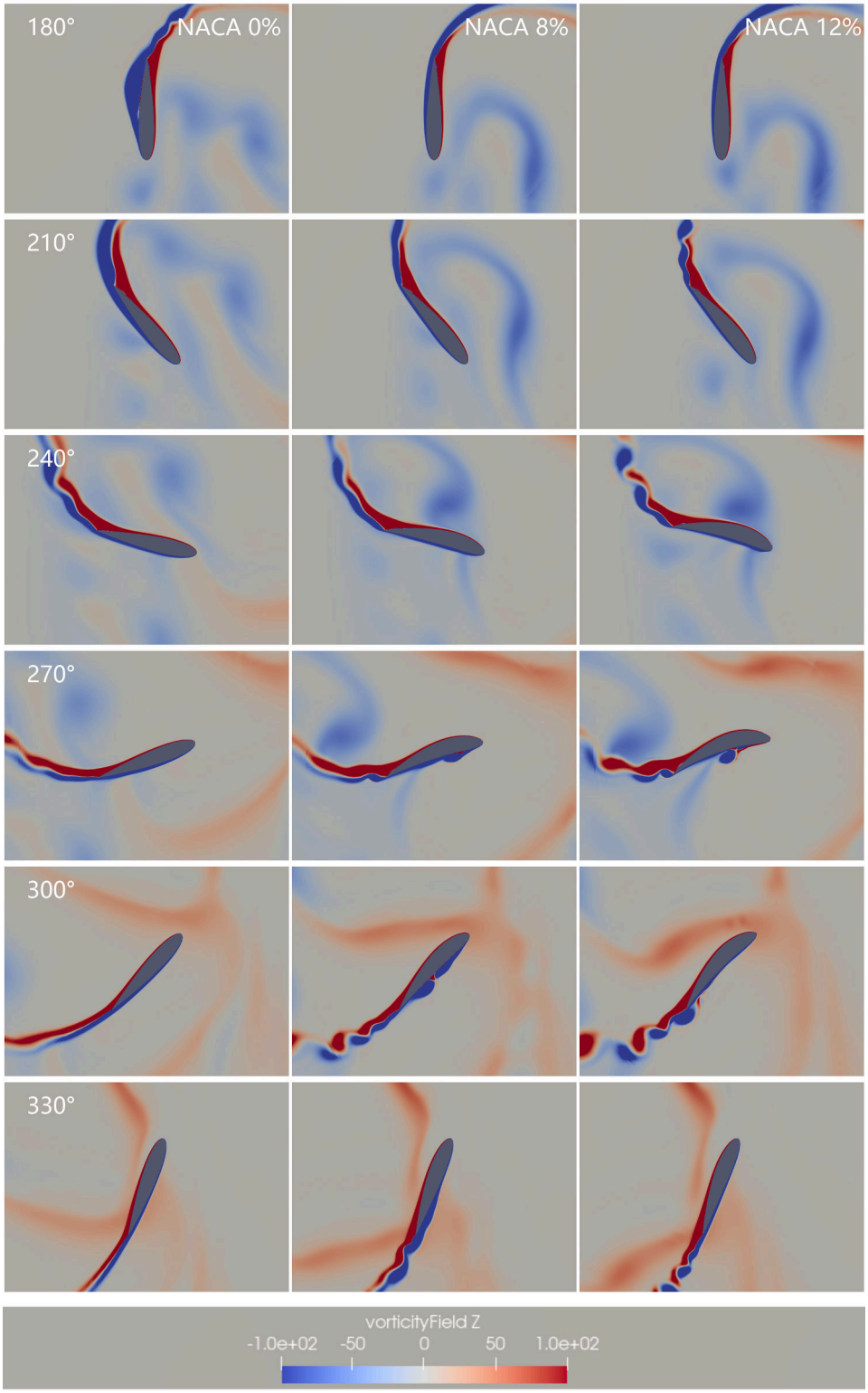

Figure 3.7: Vorticity field for cases with different NACA camber degree, $180° < \psi < 330°$.

3.1.3 Pressure Distribution Along the Chord

The pitching motion of the blade, the formation of the vortex, and the induced downwash velocity all have a great influence on the local pressure distribution and lift generation. Fig. 3.8 and Fig. 3.9 present the pressure distribution versus azimuth angle for both baseline and the case with 8% and 12% cambered NACA airfoils. Combining with the vertical thrust variation (Fig. 3.4), the downwash-velocity (Fig. 3.5), as well as vorticity contours (Fig. 3.6 and Fig. 3.7), following information can be obtained:

- $0° < \psi < 50°$: negative vertical thrust is provided in this region due to the virtual camber effect and a relatively small effective AoA. As the blade pitches up (clockwise), the AoA and the lift would increase. Besides, the flow is attached for both cambered and baseline cases.

- $50° < \psi < 90°$: the blade is still pitching up, thus the effective AoA and lift would continue to grow. In addition, a strong suction peak appears at the leading edge, which results in a thrust peak of the upper part of its trace.

  As the camber degree increases, the suction peak of the outer surface (suction side) at the leading edge and the absolute value of negative pressure at the inner surface (pressure side) are reduced. Overall, higher vertical thrust is generated by the camber NACA airfoils at the highest point of its trace.

- $90° < \psi < 160°$: the decreasing of pitching angle leads to a rapid reduction in lift generation.

  For the baseline case, the leading edge separation bubble (LESB) forms at the position $\psi = 120°$, which develops rapidly into leading edge vortex and spans the whole surface. Consequently, the pressure distribution on the outer surface experiences an obvious fluctuation.

  In addition, for cases with deformed airfoils, the boundary layer can follow the curvature and flow smoothly over the camber morphing surface, therefore, no vortex appears on the camber surface, which accounts for smoother pressure distribution on the outer surface (suction side).

- $160° < \psi < 230°$: rapid increment in lift could be observed for all cases due to the increasing pitching angle. Particularly, when the blade is in the lower part of its trace, the blade changes its pitching direction from clockwise to counter-clockwise direction, the leading edge vortex for the baseline case is thus eliminated when $\psi > 180°$.

- $230° < \psi < 270°$: the local downwash velocity in this region has the same magnitude as the tangential velocity of linear rotation of the blade, thus a significant downwash effect could be

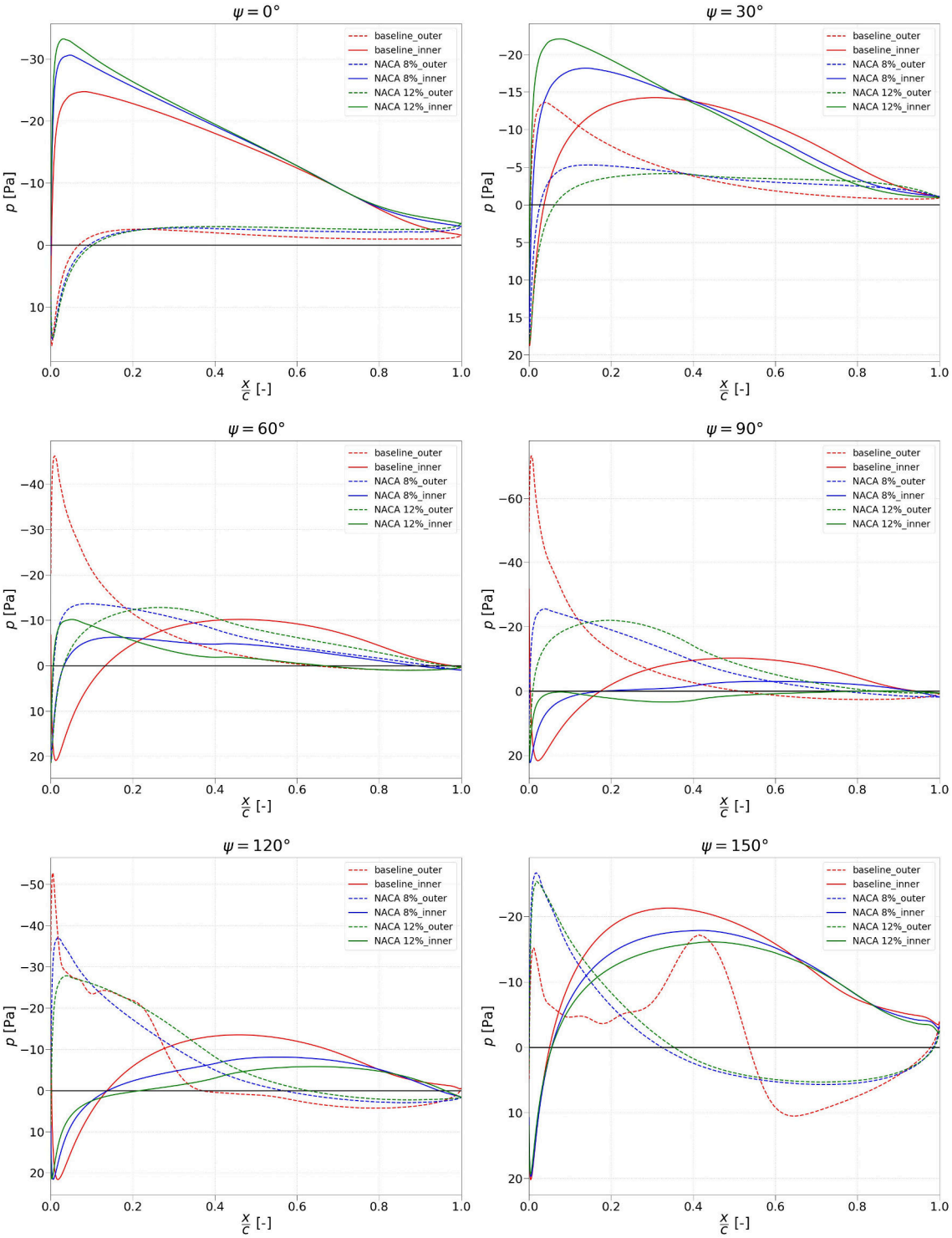

Figure 3.8: Pressure distribution for cases with different NACA camber degree, $0° < \psi < 150°$.

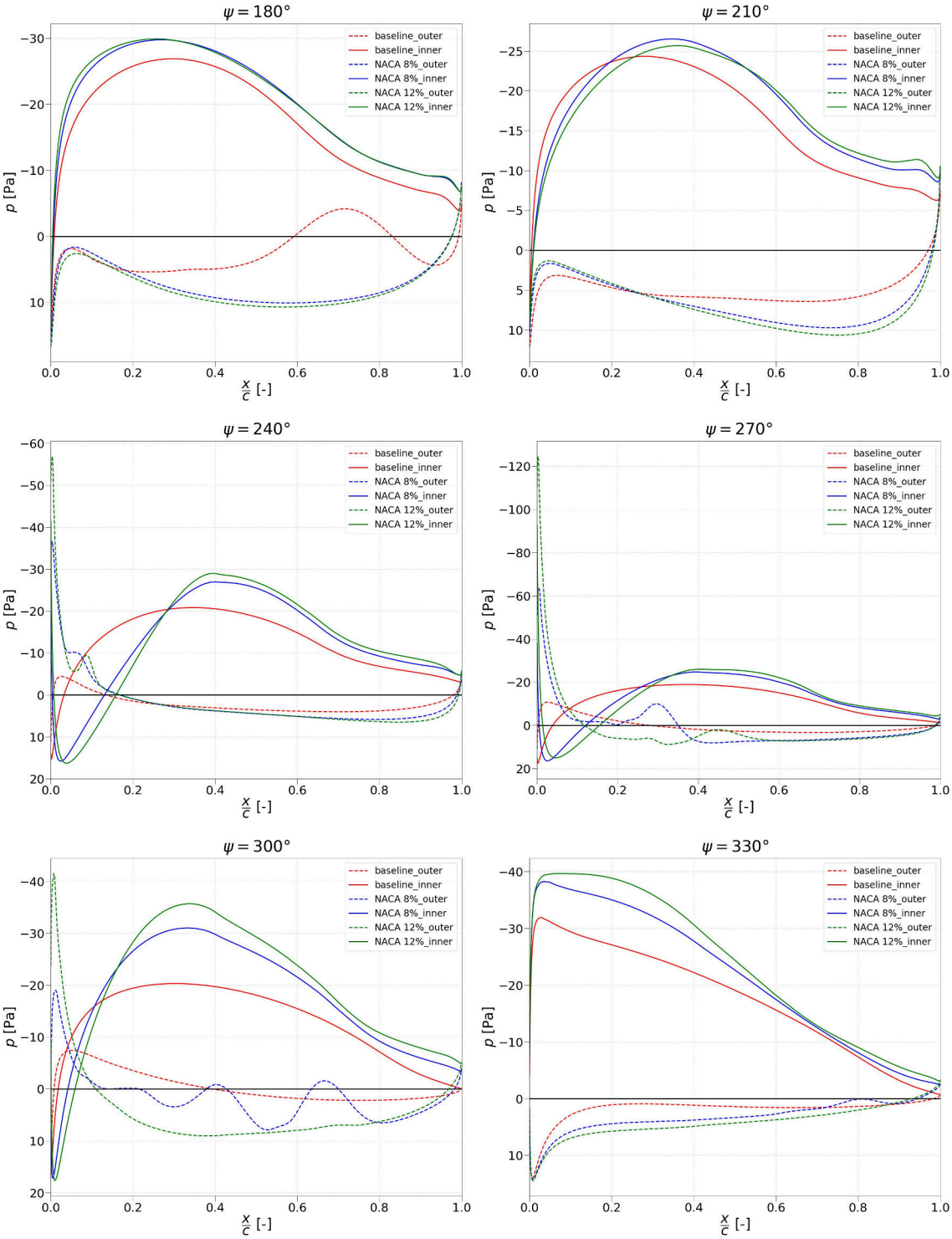

Figure 3.9: Pressure distribution for cases with different NACA camber degree, $180° < \psi < 330°$.

observed, which motivates a negative effect on lift generation. Overall, the downwash effect exceeds the pitching effect, which leads to a descending AoA and a sudden reduction in the lift for all cases.

For the case with cambered NACA airfoils, the higher negative peak at the leading edge of the outer surface increases greatly with respect to the increasing of camber degree, resulting in more lift reduction at the lowest point.

- $270° < \psi < 310°$: the influence of downwash velocity is gradually eliminated in this region, which results in the increase for both inflow velocity and effective AoA. Thus, growth in vertical thrust generation could be expected. Moreover, for the case with 12% NACA camber, the leading edge vortex appears on the outer surface (pressure side) would fluctuate the pressure distribution on the outer surface, reduction in lift generation and increasing power consumption are expected for the case with large NACA camber in this region.

  Overall, the cambered airfoils show more suction at the inner side (suction side) and a greater value at the outer side (pressure side) in the middle section of the chord, which results in a higher peak value of lift at $\psi < 310°$.

- $310° < \psi < 360°$: as the blade pitches down, the effective AoA decreases. Besides, combining with the reduced downwash velocity, a rapid decrease in vertical thrust would be expected in this region.

3.2 Effect of Position of Maximum Camber

The maximum camber position plays an essential role in the aerodynamic performance of the cambered NACA airfoils. In this section, 5 cases with different positions of maximum camber p, varies from 0.2 to 0.6 of the normalized chord, are investigated to analyze its effect. All cases have identical 12% camber degrees for the upper and lower half, i.e., $m_u = m_L = 12\%$.

3.2.1 Force and Power Analysis

The results of the force and required power are shown in Fig. 3.10. From the figure, the value of resultant force first experiences a increasing trend and reaches its maximum value when $p = 0.4$, following by a sharp descending trend, as the position of the maximum camber moves backwards, from LE to TE. Meanwhile, the required power shows a fluctuating trend with respect to the changing positions of the maximum camber. Specifically, relatively less power is required when the maximum camber is at the position of 30% of the normalized chord.

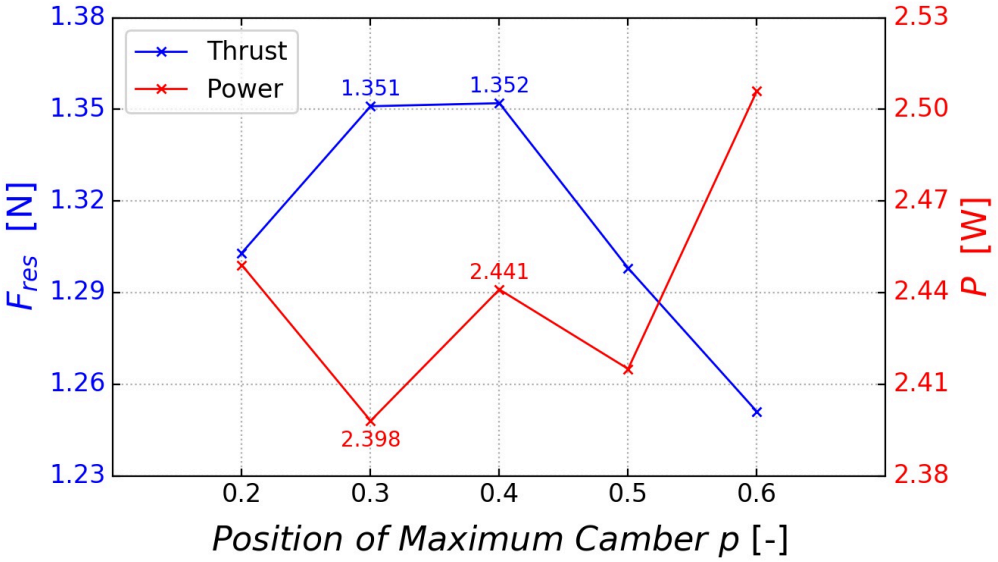

Figure 3.10: Thrust and power prediction vs. maximum camber position, $m = 12\%$.

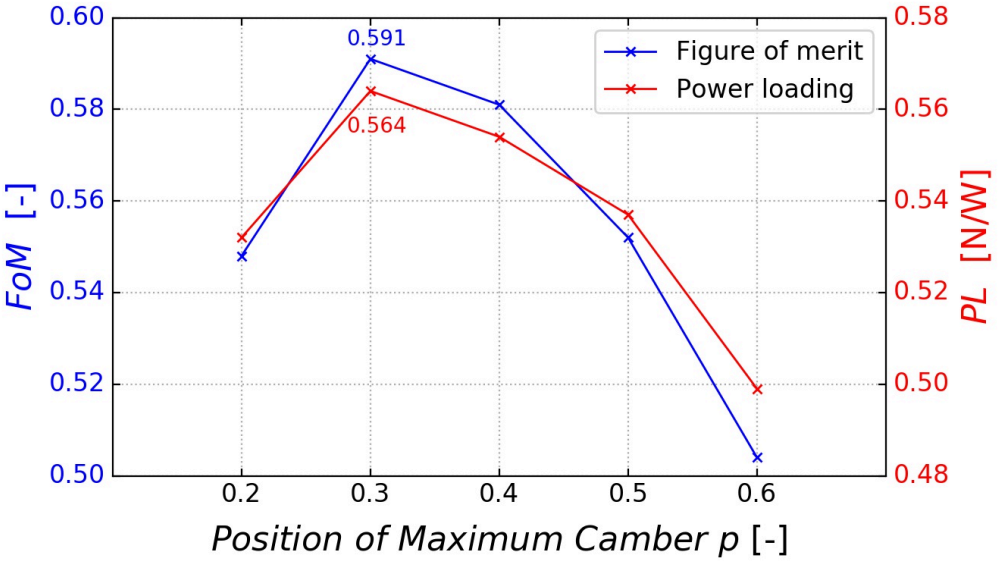

Figure 3.11: Efficiency prediction vs. maximum camber position, $m = 12\%$.

Fig. 3.11 illustrates the variation of efficiencies versus the position of maximum NACA camber. Particularly, both power loading and figure of merit will first increase, followed by a rapid decline, with respect to the increasing p value. In addition, the case $p = 0.3$ shows the best results for both figures of merit (39.7% higher than the value of baseline case), and power loading (10.4% higher than the baseline case).

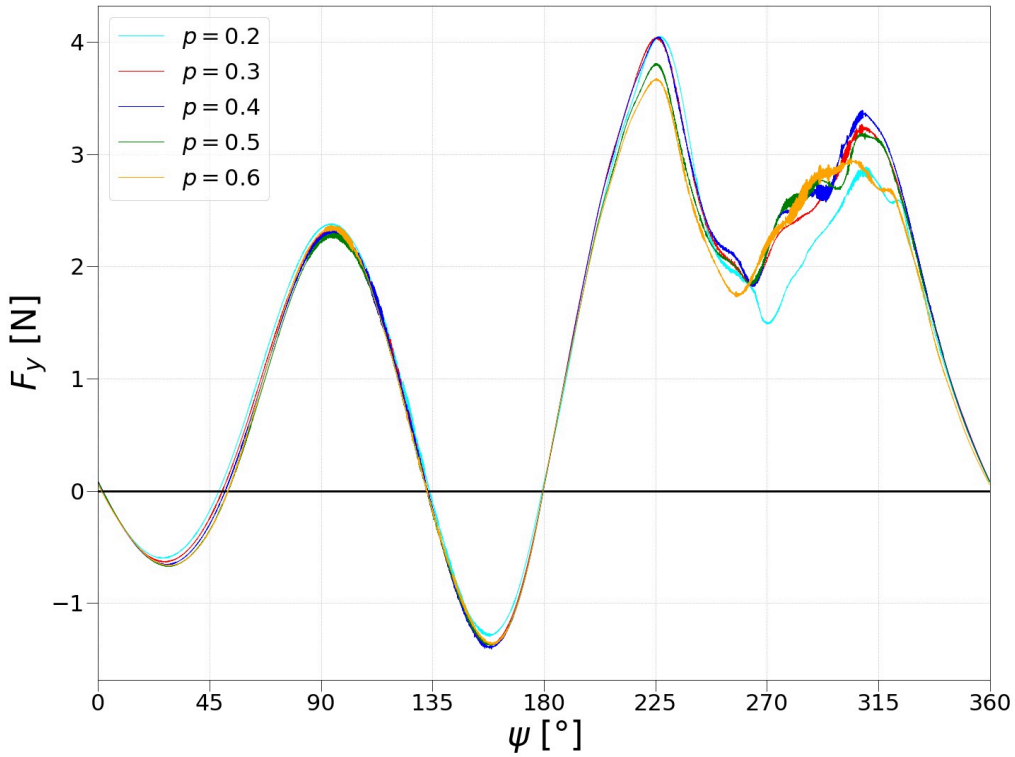

Figure 3.12: Vertical thrust distribution for one blade with different maximum camber position.

The variation of the vertical thrust of one blade over one cycle for cases with cambered NACA airfoil with different positions of maximum camber is included in Fig. 3.12. As depicted in the figure, when the blade is in the region of $-40° < \psi < 200°$, the thrust variation curves of cases with different maximum camber positions nearly overlap with each other. Besides, the major difference occurs in the region of $210° < \psi < 320°$. The cases where the maximum camber position is closest to the leading edge, i.e., $p = 0.2$, achieve the highest value of vertical thrust at the position $\psi = 225°$ and the lowest value of third lift peak at the position $\psi = 310°$, while the cases where the maximum camber is closer to the trailing edge, i.e., $p = 0.6$, produces less vertical thrust in the interval of $210° < \psi < 320°$ than any other case.

More information of the lift and power variation will be introduced in the following sections.

3.2.2 Flow Field Visualization

The downwash velocity for cases with different positions of NACA camber is shown in Fig. 3.13 As depicted in the figure, no obvious change in velocity magnitude and its influence area could be observed. In addition, for all cases, the effect is most significant when the blade is at the lowest point of its trajectory. However, as the position moves backward, the thrust angle varies from 103.9° ($p = 0.2$) to 102.2° ($p = 0.4$) and 100.0° ($p = 0.6$). As a result, the area affected by downwash velocity experiences a slightly clockwise shift. At the same time, the position of maximum downwash velocity moves slight downward, which causes changes in pressure distribution at the inner surface at the lower end of its trace.

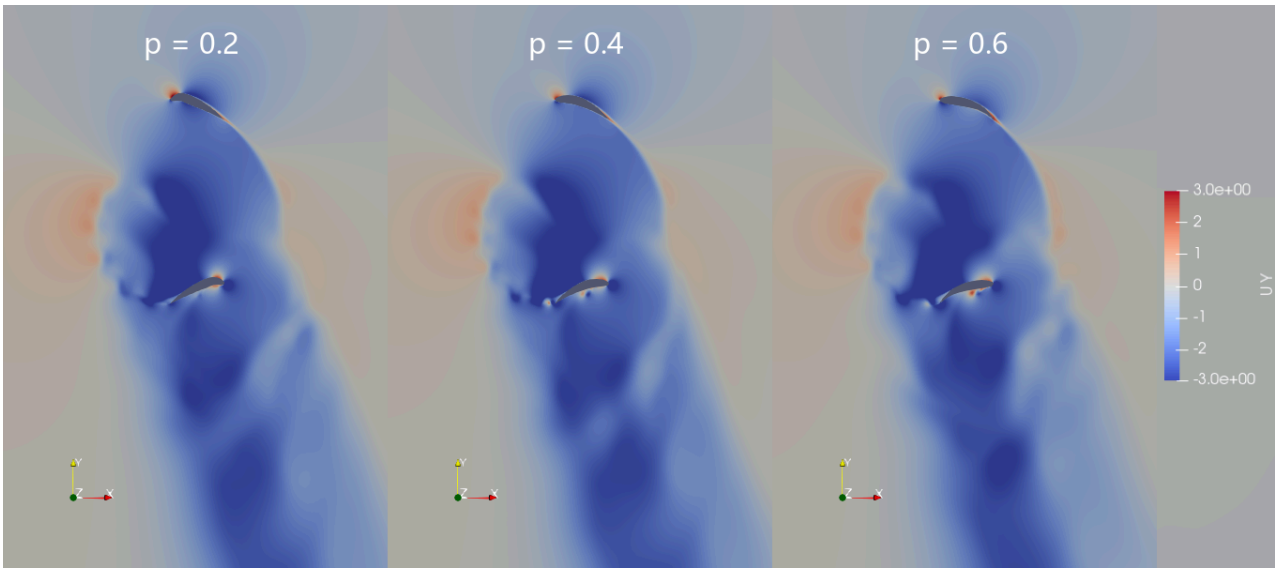

Figure 3.13: Downwash velocity for cases with different maximum camber position.

The vorticity contours for cambered NACA airfoils with different maximum camber positions are shown in Fig. 3.14.

From the figures, when the blade is passing through the upper part of its trace, no significant difference could be observed. Besides, the fluid flows smoothly over the blades and no sign of vortex are appearing on the surface of the cambered airfoils for all cases. The only difference occurs in the region of $150° < \psi < 180°$, where a thickened boundary layer vorticity is observed for the case $p = 0.2$.

When the blade is passing through the lower end of its trace, the formation of leading edge vortex, which is caused by the concave shape of the outer surface (pressure surface) of cambered NACA airfoil and the blade vortex interaction, could be seen for all cases. Moreover, the appearance of the vortex is slightly delayed as the position of the maximum camber moves backwards. For the case

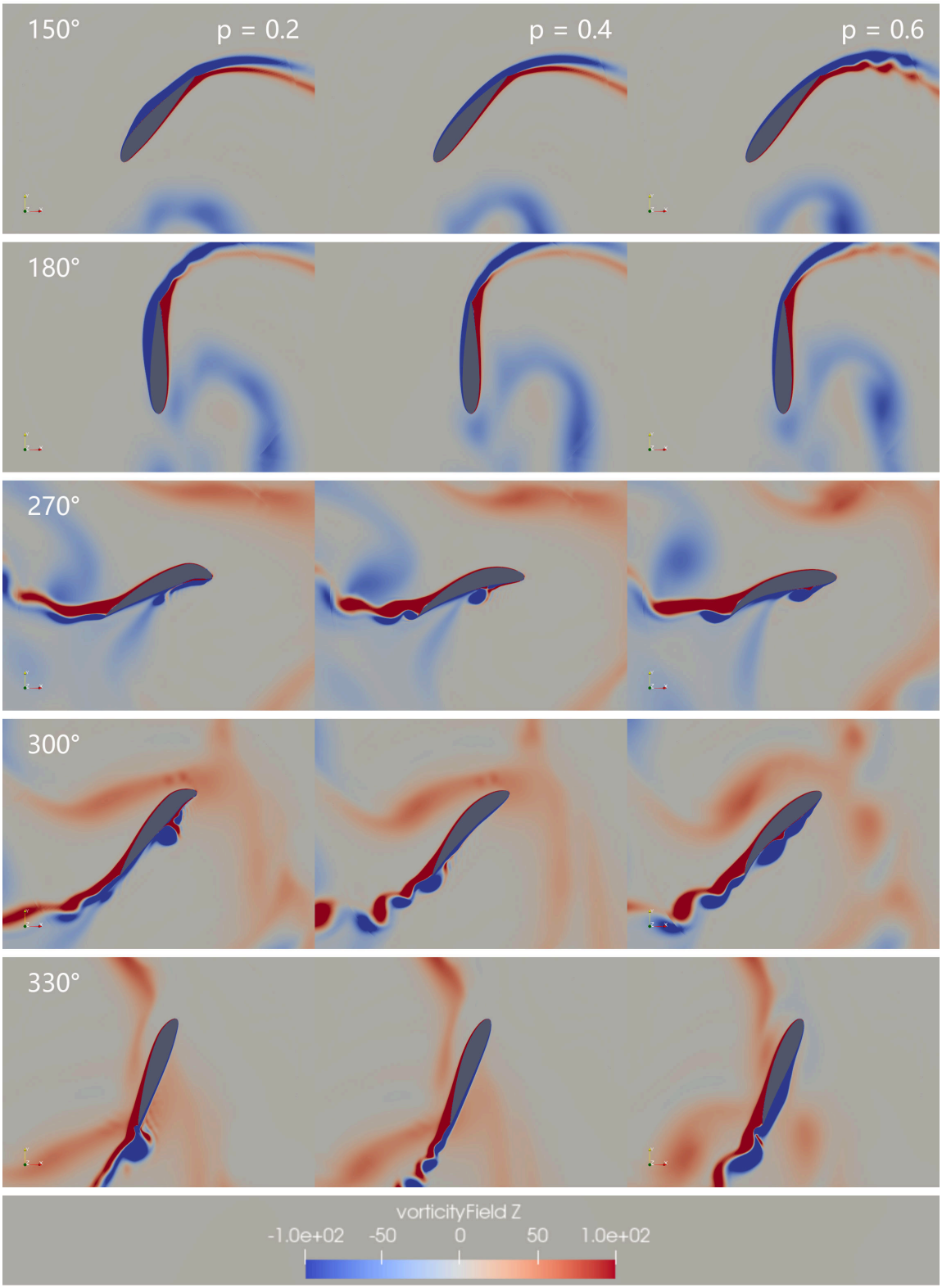

Figure 3.14: Vorticity field for cases with different maximum camber position.

$p = 0.2$, $p = 0.4$, and $p = 0.6$, the LEV forms at the position of $\psi = 236°$, $\psi = 240°$, and $\psi = 246°$, respectively. It is worth mentioning that the development of LEV and its detachment are greatly affected by the position of the maximum camber. In particular:

- For the case $p = 0.2$, the LEV travels downstream and detaches at the position $\psi = 272°$ while a new vortex forms at the leading edge and grows rapidly. The detached smaller vortex flows parallel downstream and joins the vortex shedding at the trailing edge, while the larger new LEV grows and quickly spans the entire leading edge. Then the larger LEV is detached at $\psi = 306°$ and subsequently sheds at the trailing edge.

- For the case $p = 0.4$, the LEV detaches at the position $\psi = 268°$. Subsequently, the detached vortex flows parallel downstream and detaches at the TE near the position $\psi = 300°$. Moreover, a pair of vortex streets is observed in the wake region due to the curved blade surface and the vortex shedding at the TE.

- For the case $p = 0.6$, the size of the vortex develops quickly and soon spans the entire upper surface at the position $\psi = 300°$. As the blade pitches down, the LEV at the inner surface diminishes and gradually turns into boundary vorticity.

3.2.3 Pressure Distribution Along the Chord

The Fig. 3.15 and Fig. 3.16 show the pressure distribution of cambered NACA airfoils with different maximum camber position. Combining with the vertical thrust variation and the vorticity contours shown in the previous sections, the major differences of the pressure distribution can be summarized as follow :

- For the upper half of the cycle, the pressure exhibits significant differences near the upper end, i.e. $60° < \psi < 120°$. In the case of $p = 0.2$, at the highest point of the trajectory, i.e., $\psi = 90°$, a large suction peak can be observed at the leading edge, and then the pressure drops rapidly. As the position of maximum camber moves backwards, the location of the suction peak shifts downstream as well, meanwhile, a lower peak value, followed by a slower pressure drop, can be observed in the plots. Consequently, more vertical thrust generation near the trailing edge could be expected. In addition, the increase of lift generation at the rear part compensates for the loss caused by the decreasing suction peak at the leading edge. Overall, the lift generated in the upper half is nearly the same for all three cases.

- At the lower end of the trajectory, i.e., $240° < \psi < 300°$, the pressure distribution is greatly affected by the formation and development of the vortex. In detail, the location of the suction

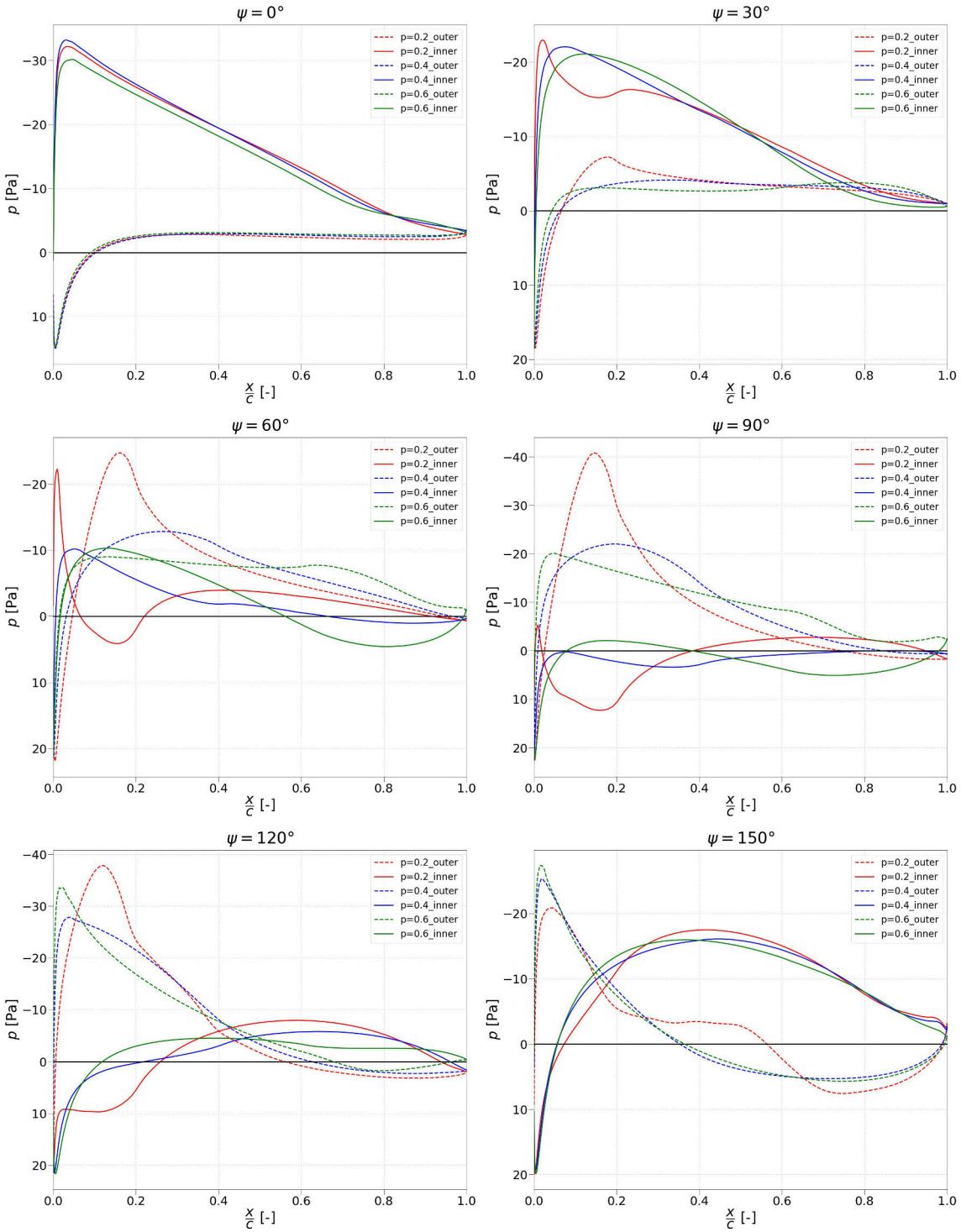

Figure 3.15: Pressure distribution for cases with different maximum camber position, $0° < \psi < 150°$.

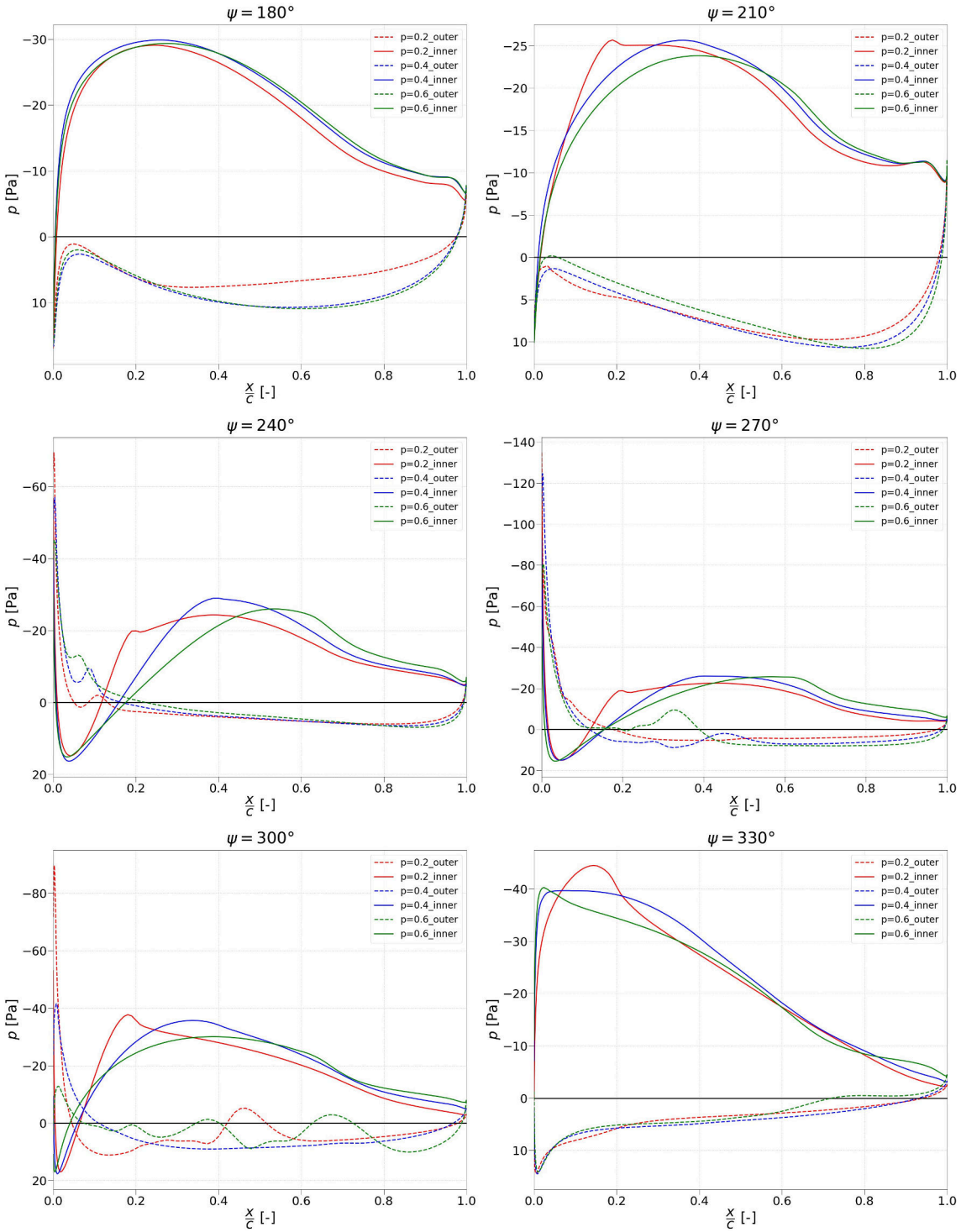

Figure 3.16: Pressure distribution for cases with different maximum camber position, $180° < \psi < 330°$.

peak (inner side) will slightly move backward as the value of p increases. Except for that, the pressure distribution of the inner surface exhibits a consistent behaviour for all cases.

On the contrary, the pressure distribution on the outer surface experiences a significant change. In detail, in the case of $p = 0.2$, a significantly higher peak of negative pressure at the LE of the outer surface is obtained in this region. As the position of the camber angle moves backwards, lower vertical thrust peaks are observed in the plots, which is similar to the situation for the upper half. In particular, for the case $p = 0.4$, the pressure on the outer surface shows a small depression at the leading edge in the range of $270° < \psi < 300°$, due to the appearance of LEV. Moreover, for the case $p = 0.2$ and $p = 0.6$, significant pressure fluctuations can be observed on the entire outer surface in the range of $270° < \psi < 320°$ due to the growth and detachment of LEV, which results in a lower third peak of vertical thrust at the position $\psi < 300°$.

3.3 Effect of Asymmetric Camber Morphing

As illustrated in the previous sections, the blade behaves differently at the upper and lower half of its trajectory. In this section, the aerodynamic performance of 5 cases with asymmetric cambered NACA airfoils are evaluated. Therefore, cases in this chapter have different maximum camber degree for the upper (m_U) and lower half (m_L) of the cycle. Besides, all cases have an average of 12% maximum camber degree of the upper and lower parts and the maximum camber positions are set to 0.4, i.e., $p = 0.4$.

3.3.1 Force and Power Analysis

The results of the resultant force and required power are shown in Fig. 3.17, where U and L represent the maximum camber degree for the upper half and lower half. For instance, U8/L16 means $m_U = 8\%$ and $m_L = 16\%$. From the figure, the case with less camber at the top and more camber at the bottom ($m_U < m_L$) achieve a relatively higher thrust and power. However, the values of required power and the resultant thrust decrease continuously with the increasing value of m_U and descending m_L.

Figure 3.18 illustrates the variation of efficiency of the asymmetric cambered NACA airfoils. Particularly, both power loading and figure of merit will first experience a moderate increase, followed by a slight decline, with the increasing of camber for the upper half and the decreasing of morphing for the lower half. In addition, the case U12/L12 shows the best results for the figure of merit (37.4% higher than the value of baseline case), while the case U14/L10 achieves the highest value of power

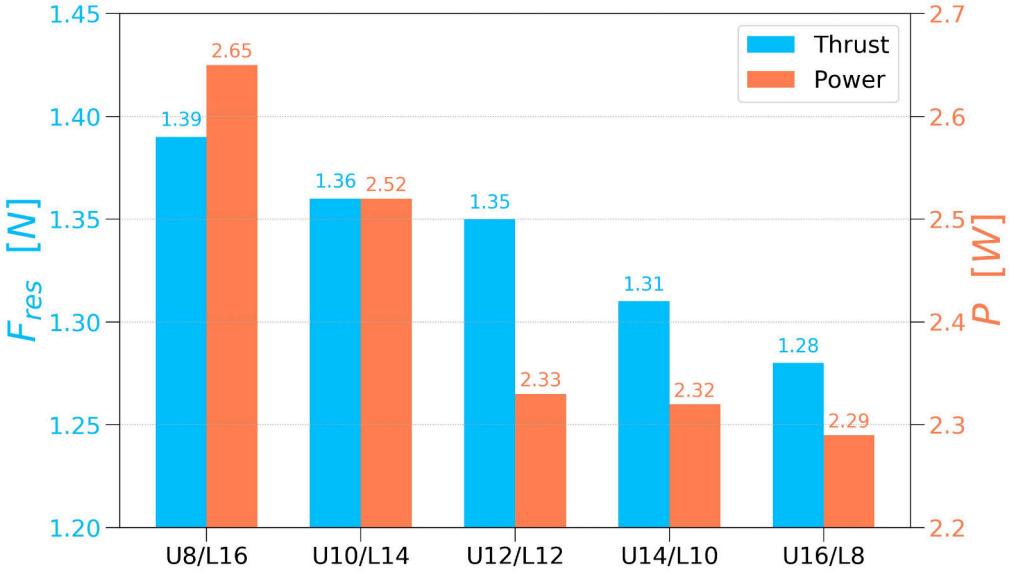

Figure 3.17: Thrust and power prediction for cases with asymmetric cambered NACA airfoils.

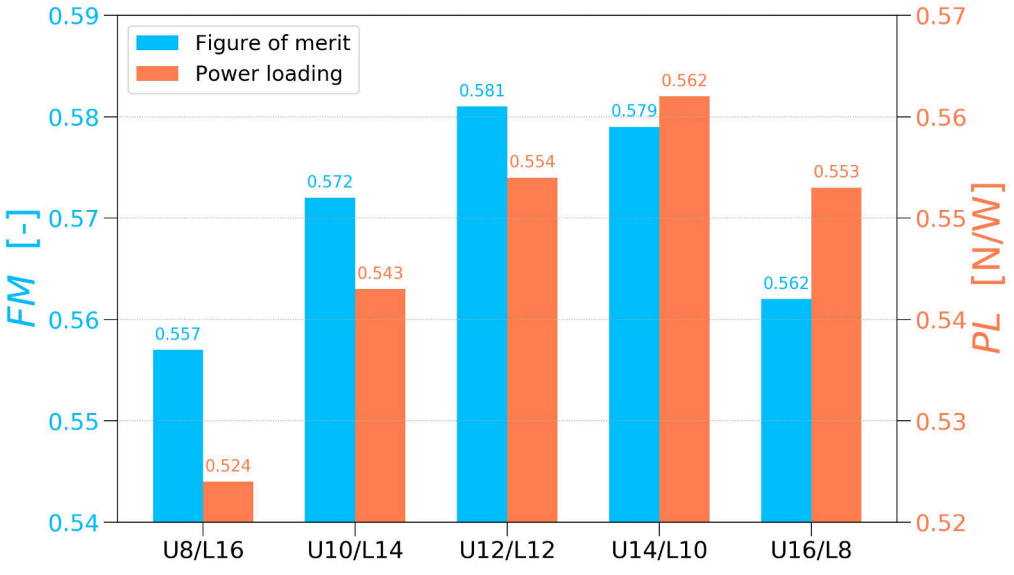

Figure 3.18: Efficiency prediction for cases with asymmetric cambered NACA airfoils.

loading (9.98% higher than the baseline case).

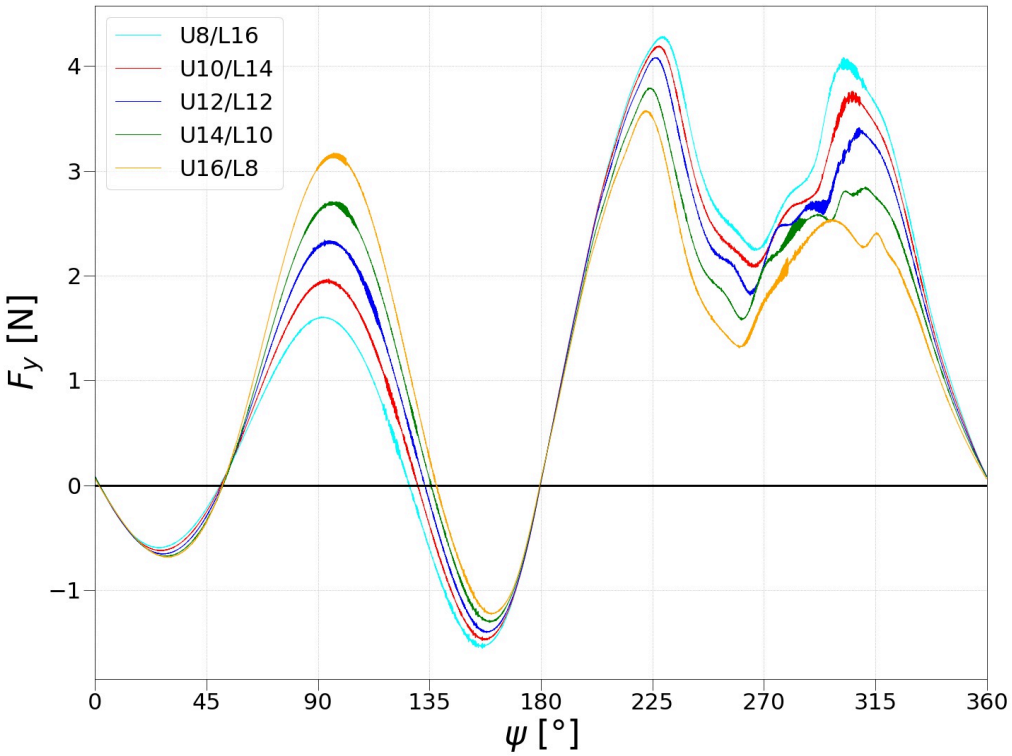

Figure 3.19: Vertical force distribution for one blade for cases with asymmetric NACA camber.

The variation of vertical force of asymmetric NACA camber airfoils over one period is shown in Fig. 3.19. Specifically, cases with asymmetric cambered airfoils have consistent thrust variation patterns. For the upper part of the trajectory, the vertical thrust is mainly produced near the top of the trajectory. Moreover, the peak value at the top position is directly related to the value of m_U. Furthermore, for the lower right part of the rotation, a higher peak at $\psi = 225°$ (global maximum) and a relatively lower local maximum value at $\psi = 310°$ are observed for all cases, besides, the lift is mainly obtained in the interval near these two peaks. As the value of m_L increases, the lift value between these two peaks moves upward.

Detailed illustrations of the lift variation with respect to the local flow condition would be presented in the following sections.

3.3.2 Flow Field Visualization

The downwash velocity contour for cases with asymmetric cambered NACA airfoils is shown in Fig. 3.20. A slight change in velocity magnitude and its influence area could be observed from the figure. Moreover, the cases U8/L16, U12/L12, and U16/L8 have thrust angles of 105.4°, 102.2°, and

98.4°, respectively. It can be inferred that with increasing m_U and descending m_L, the direction of the resultant force will move slightly towards the negative y-axis.

As a result, for the case U8/L16, a more concentrated influence area of downwash velocity could be expected in the lower right part of the trajectory, i.e., $270° < \psi < 300°$. While the case U16/L8, i.e., less camber for the upper half and more camber for the lower half, experience a more dispersed downwash velocity distribution and an enlarged influence area in the lower half of the cycle. Particularly, intensified downwash effect is observed in the region $270° < \psi < 290°$, which will lead to the change in pressure distribution at the lower end.

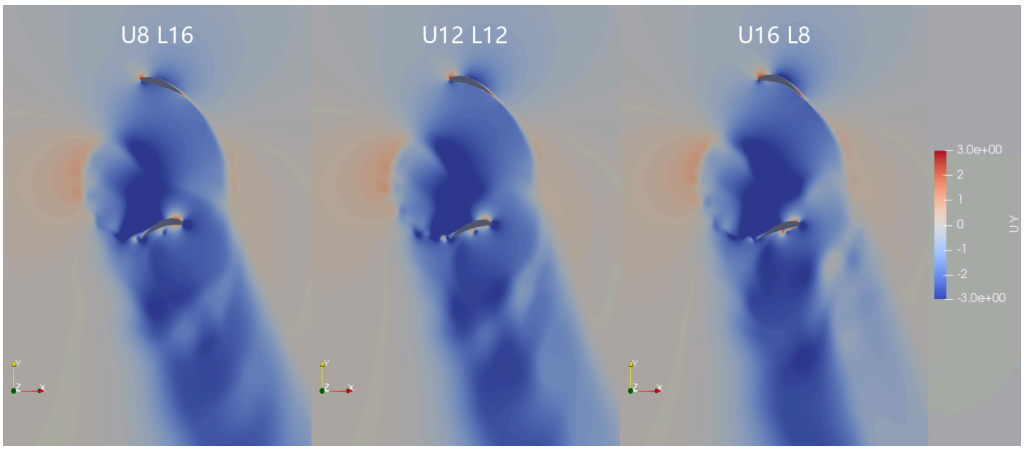

Figure 3.20: Downwash velocity for cases with asymmetric cambered NACA airfoils.

The vorticity contours of the case with asymmetric cambered NACA are shown in Fig. 3.21. When the blade is passing through the upper part of its trace, no significant difference could be observed. Besides, the fluid flows smoothly over the blades and no vortex appears on the surface of the cambered airfoils.

The major difference occurs when the blade is passing through the lower end. In detail, the formation of leading edge vortex near the position $\psi = 240°$ are observed for all cases, due to the concaved outer surface (pressure side) of cambered NACA airfoil and the negative vorticity shedding from the preceding blade.

Particularly, for cases U8/L16 and U12/L12, the LEV travels downstream and detaches near the position of $\psi = 272°$. Moreover, the detached vortex flows parallel down to the trailing edge and joins the vortex shedding near the position of $\psi = 300°$.

In the case U16/L8, the LEV develops rapidly and soon spans on the entire outer surface. At the position of $\psi = 298°$, the vortex breaks in the middle and splits into a leading edge vortex (LEV) and a trailing edge vortex (TEV). Subsequently, the TEV travels down to the trailing edge and sheds at $\psi = 320°$, while the LEV diminishes due to the pitching motion of the blade and eventually turns

into the boundary vorticity at $\psi = 346°$.

More detailed information about unsteady phenomena and their corresponding influence on the pressure distribution is introduced in the next section.

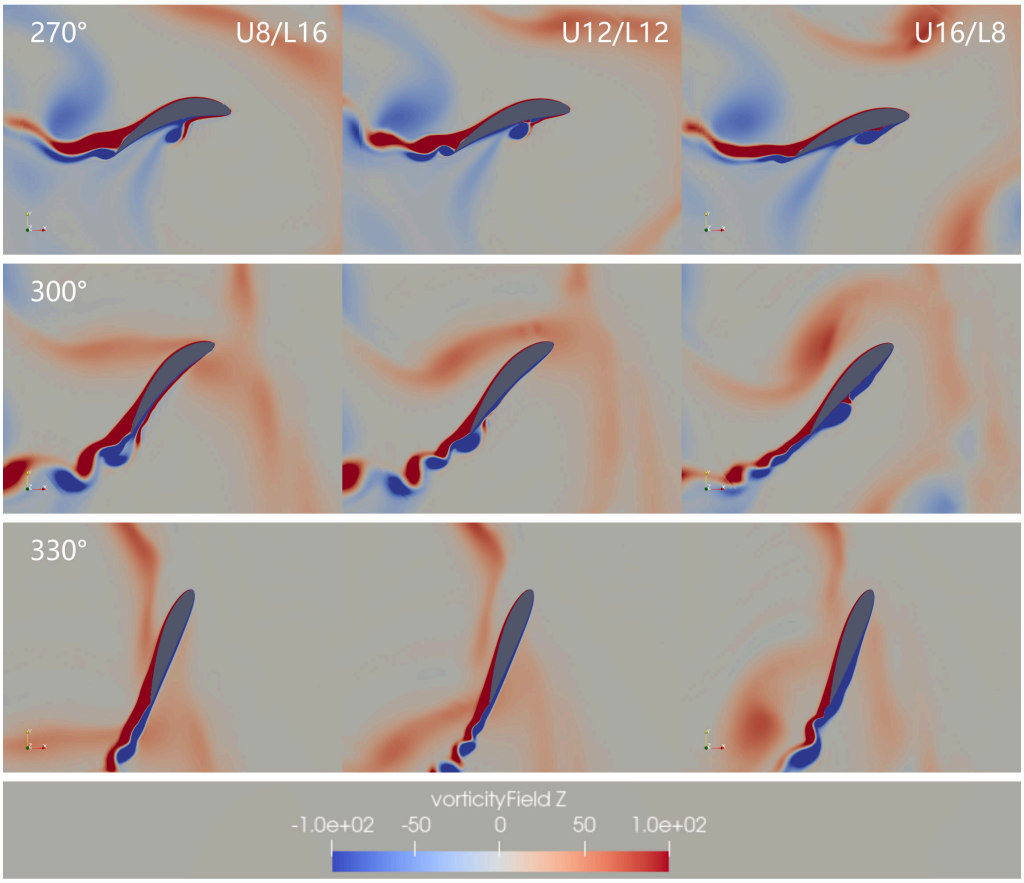

Figure 3.21: Vorticity field for cases with asymmetric cambered NACA airfoils.

3.3.3 Pressure Distribution along the Chord

Figure 3.22 indicates the pressure distribution versus azimuth angle for both baseline and the cases with asymmetric cambered NACA airfoils. Combining with the vertical thrust variation and the vorticity contours presented in previous sections, the major difference of the pressure distribution can be summarized as follow:

- Near the highest point of the trace, i.e., $\psi = 90°$, the position of the suction peak at the outer surface (suction surface) moves backward as the value of m_U increase. Besides, a higher negative pressure peak at the outer surface and greater positive pressure at the inner surface (pressure side) result in a higher vertical force for the case with more camber in the upper half.

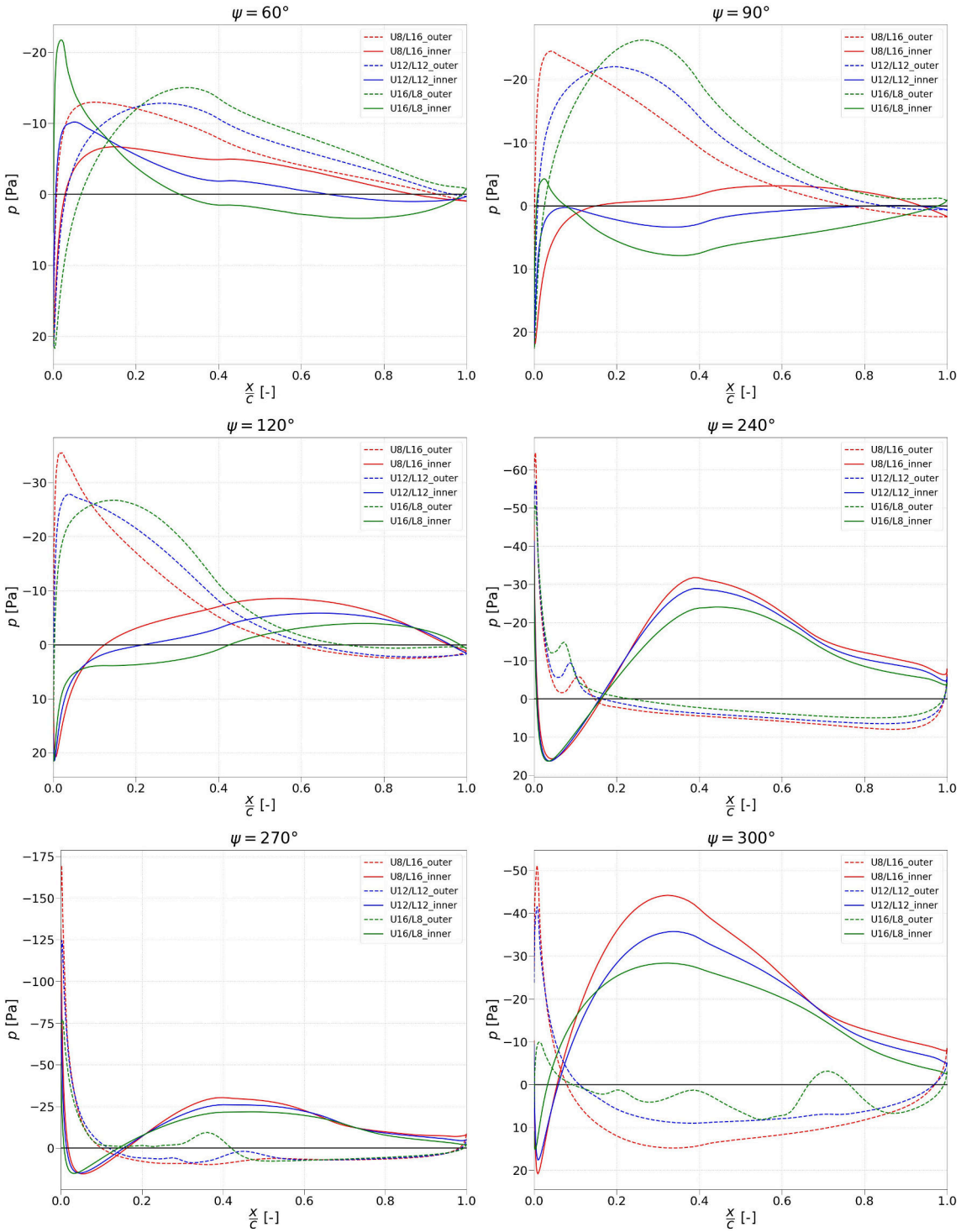

Figure 3.22: Pressure distribution for cases with asymmetric cambered NACA airfoils.

- At the lower end of the trajectory, i.e., $240^\circ < \psi < 300^\circ$, a significantly higher peak of negative pressure at the leading edge of the inner surface (suction surface) for the case with more camber at the lower part (U8/L16) is observed. And the lower pressure on the outer surface (pressure surface) accounts for a higher peak value of vertical thrust in this region for the case with more camber at the lower part.

- Especially, for the case with more camber in the lower part (U12/L12 and U8/L16), the pressure distribution exhibits a slight depression at the leading edge in the range of $270^\circ < \psi < 300^\circ$, due to the appearance of a leading edge vortex. While for the case U16/L8, greatly fluctuating pressure distribution on the entire outer surface could be observed in the region $270^\circ < \psi < 320^\circ$, due to the formation and the development of LEV and TEV.

4 Results of Trailing Edge Morphing

This chapter compared the aerodynamic performance of airfoils with cambered trailing edges. Particularly, the effect of camber degree, the effect of start location of trailing edge camber, and the asymmetric camber effect are obtained in this chapter.

4.1 Effect of Maximum Degree of Camber Morphing

In the beginning, the effect of camber degree is investigated. In this section, the maximum camber degree varies from 0% to 16%, with the morphing starting at the position of 70% chord, i.e., $p = 0.7$, as depicted in Fig. 4.1. Moreover, the maximum camber degree for the upper (m_U) and lower (m_L) half are set to be identical. Besides, the baseline case with symmetric airfoils is denoted as 0% TE camber.

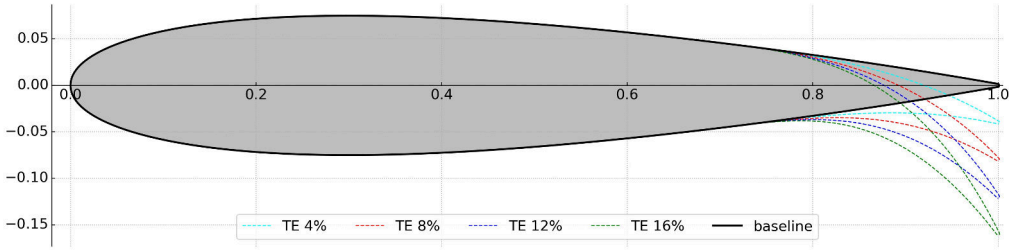

Figure 4.1: Airfoils with cambered trailing edge, $p = 0.7$.

4.1.1 Force and Power Analysis

Figure 4.2 depicts the change of averaged resultant thrust and required power in hover state over the TE camber degree. Similar to the case with the NACA camber concept, significantly higher resultant thrust and power levels can be achieved with respect to the increasing camber degree within the camber range.

Moreover, as shown in the figure, the thrust grows linearly as the camber degree increase while the power shows a quadratic increasing tendency. For the cases with 4%, 8%, 12%, and 16% TE camber morphing, 31.9%, 59.7%, 86.4%, and 116% higher thrust are observed, respectively. Meanwhile, 28.2%, 58.8%, 100%, and 156% extra power are required by the morphing blades. Apparently, the increment is significantly greater than the case of the NACA camber concept with the same camber

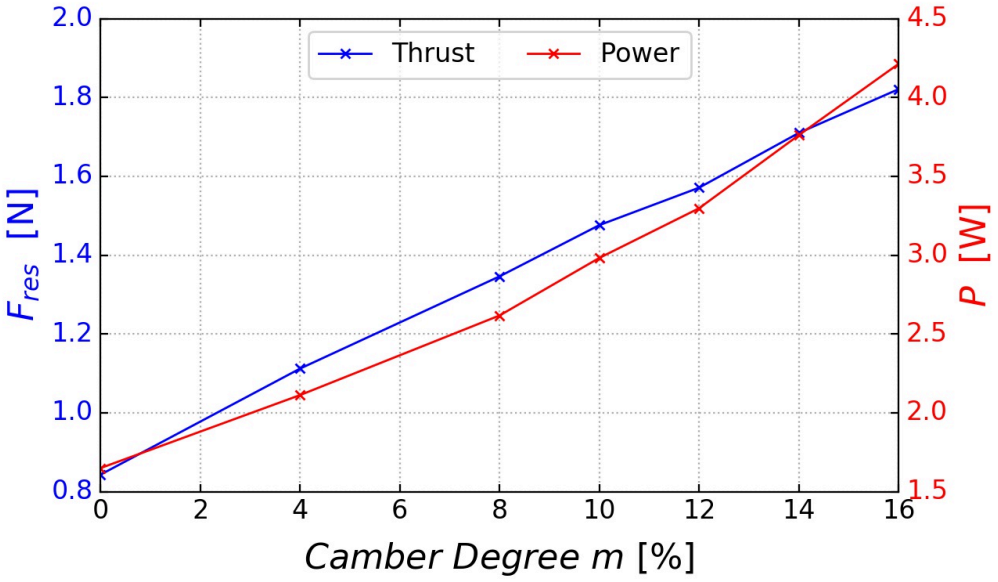

Figure 4.2: Thrust and power prediction vs. TE camber degree, $p = 0.7$.

degree.

The results of figure of merit and power loading versus the TE camber degree are included in Fig. 4.3. Specifically, the value of power loading will first exhibit a slight increment, followed by a continuously descending trend, as the TE camber degree increases. Consequently, for the case with small TE camber, higher values of power loading are obtained, while the increment will disappear under the situation $m > 8\%$. This trend can be explained by the change in force and power. In detail, in the case of small camber, more gain in resultant thrust is observed when compared with the required power. As the camber degree increased, the power grows more rapidly, thus the gain in power exceeds the increment of thrust, which accounts for the reduction in power loading. Moreover, the best result of power loading is obtained when the camber degree is around 4%. Furthermore, the variation of figure of merit over the camber degree exhibits a similar behaviour, it will first increase and then decrease as more camber is introduced. Specifically, the FoM reaches its maximum value of 0.542 (27.7% higher compared with baseline case) in the case of 10% TE morphing.

The variation of vertical force and power for one blade over the period is shown in Fig. 4.4. Particularly, as shown in Fig. 4.4(a), a significantly higher peak of vertical thrust is observed with respect to the increasing camber degree, and the blades perform better at the lower part of the trajectory for both baseline cases and cases with cambered TE. Particularly, for the baseline case, a relative small amount of lift is produced in the upper half of the cycle, most of the vertical thrust is generated in the interval of $220° < \psi < 320°$. As for the cases with cambered TE, the thrust is mainly

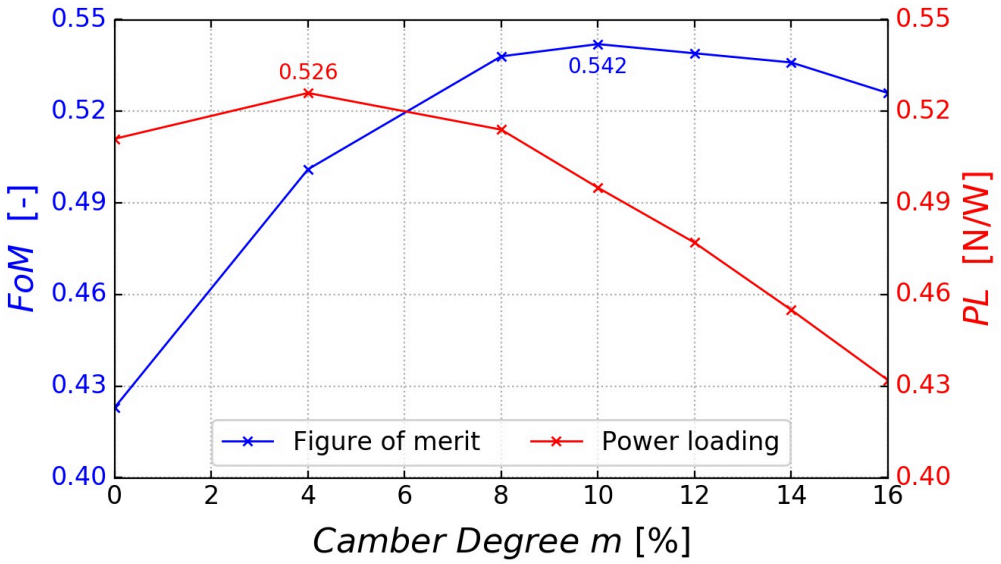

Figure 4.3: Efficiency prediction vs. TE camber degree, $p = 0.7$.

obtained at the positions near $\psi = 90°$, $\psi = 225°$, and $\psi = 300°$. Moreover, a higher peak value of thrust will be observed near the top and lower left part of the trajectory as the TE camber increases. It is particularly noteworthy that in the lower right part of the rotation, i.e., $270° < \psi < 320°$, the lift value of the third peak even exceeds the previous one and reaches its maximum during the entire cycle in the case of 16% TE camber.

The results of the required power are presented in Fig. 4.4(b). For the upper half of its trace, the variation of the required power is consistent with the thrust change shown in Fig. 4.4(a), the major difference occurs at the lower half. Specifically, due to the blade vortex interaction, significantly more power is required near the lower end $270° < \psi < 315°$ for cases with large TE camber degree.

In addition, the significant change in thrust and power with the increasing camber degree could be explained by the intensified downwash velocity and the change of flow field condition. More information would be introduced in the following sections.

4.1.2 Flow Field Visualization

As mentioned in the previous section 3.1.2, the induced downwash velocity plays an essential role in the aerodynamic performance of the cycloidal rotor. For the cases with different TE camber degree, as described in Fig. 4.5, the larger the camber degree is, the more intensified and concentrated downwash velocity is observed. Especially in the lower right part of the trajectory, i.e., $260° < \psi < 310°$, the local downwash velocity has the same magnitude as the tangential velocity of the linear rotation of the blade. Consequently, when the blade is passing through the lower end of its trace, more

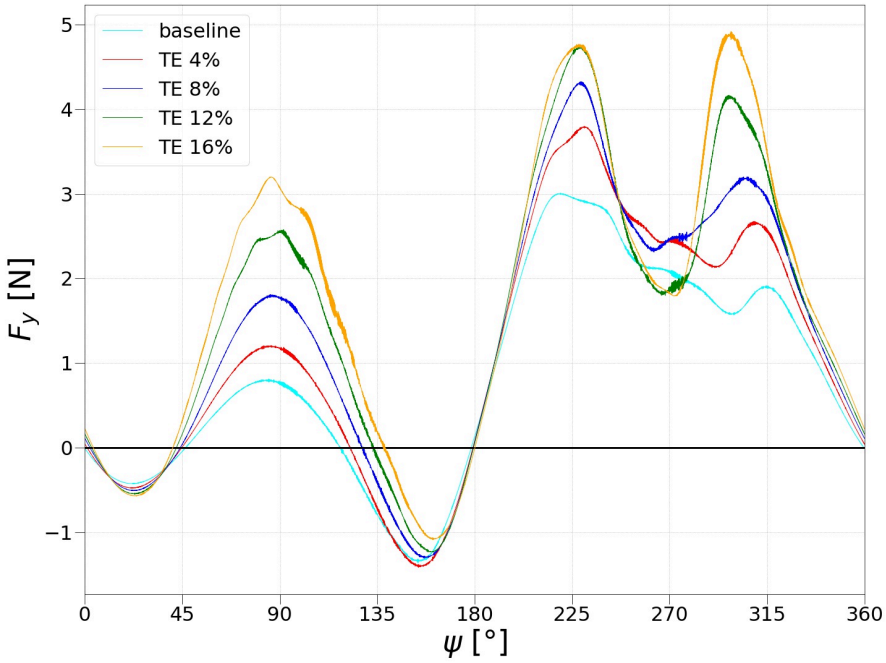

(a) Vertical force

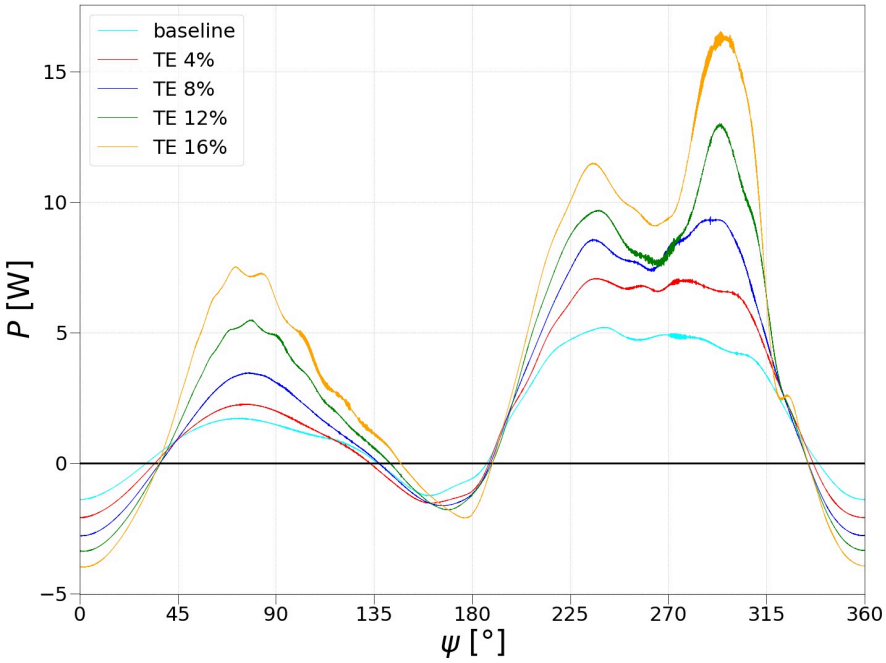

(b) Required power

Figure 4.4: Vertical thrust and power distribution for one blade with different TE camber degree.

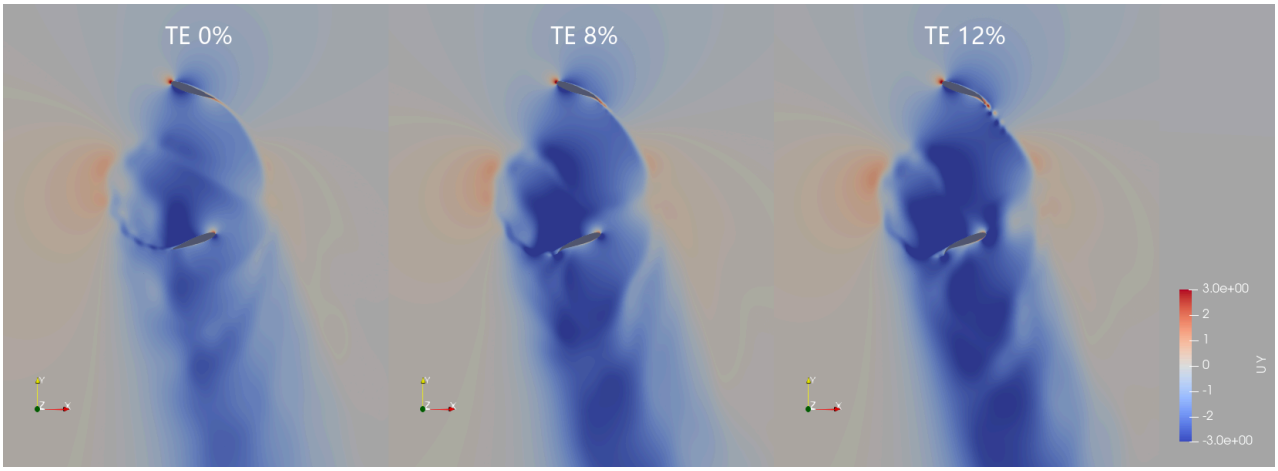

Figure 4.5: Downwash velocity for cases with different TE camber degree.

reduction in the effective AoA and change in inflow velocity could be expected for the case with large TE camber.

The vorticity contours of the cases with cambered TE are shown in Fig. 4.6 and Fig. 4.7. As shown in the figures, when the blade is moving through the upper right part of its trace, i.e., $0° < \psi < 90°$, both symmetric and cambered airfoils show similar vorticity distribution on the blade surface. However, a clearly different behaviour could be observed in the wake region. Particularly, for the case with the cambered TE, the unsteady effect is enhanced by the deformed configuration. Therefore, when the blade is near the highest point of the trace, where the maximum camber degree is applied, the boundary layer vorticity originating from the inner surface rolls up into an array of the counter-clockwise rotating vortex. Consequently, the appearance of vortex shedding in the wake region could be observed at the position of $\psi = 80°$ in the case of 12% TE camber.

When the blade is in the upper left part of its trace, i.e., $90° < \psi < 180°$, the leading edge vortex (LEV) appears on the outer surface (suction side) near the position of $\psi = 128°$ in all cases. Besides, the vortex grows rapidly and spans the entire surface. As shown in the vorticity contour, for the cases with TE camber, the size of LEV is slightly reduced, besides, the shedding vortex in the wake region could still be observed in this region.

When the blade is in the lower half of the trajectory, i.e., $180° < \psi < 360°$, for the baseline case, fluid flows smoothly on the surface of the symmetric airfoils and no signs of vortex are appearing. However, in the case of cambered TE, the flow field condition exhibits a different behaviour. The boundary vorticity at the trailing edge is also distorted by the cambered configuration. Meanwhile, in addition to the intensified downwash velocity, the presence of LEV on the outer surface (pressure side), and the blade vortex interaction (BVI) effect would account for the changes in aerodynamic

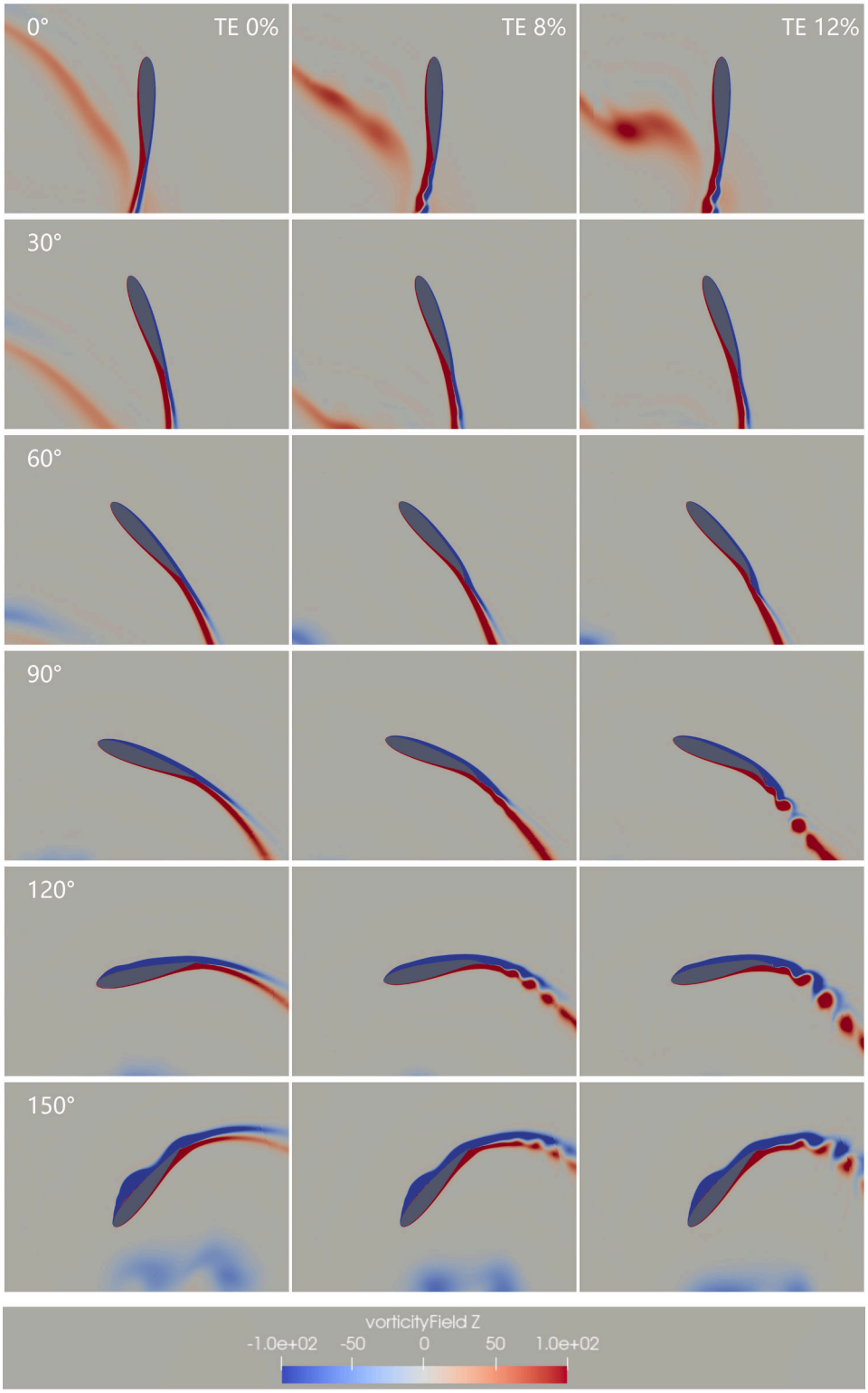

Figure 4.6: Vorticity field for for cases with different TE camber degree, $0° < \psi < 150°$.

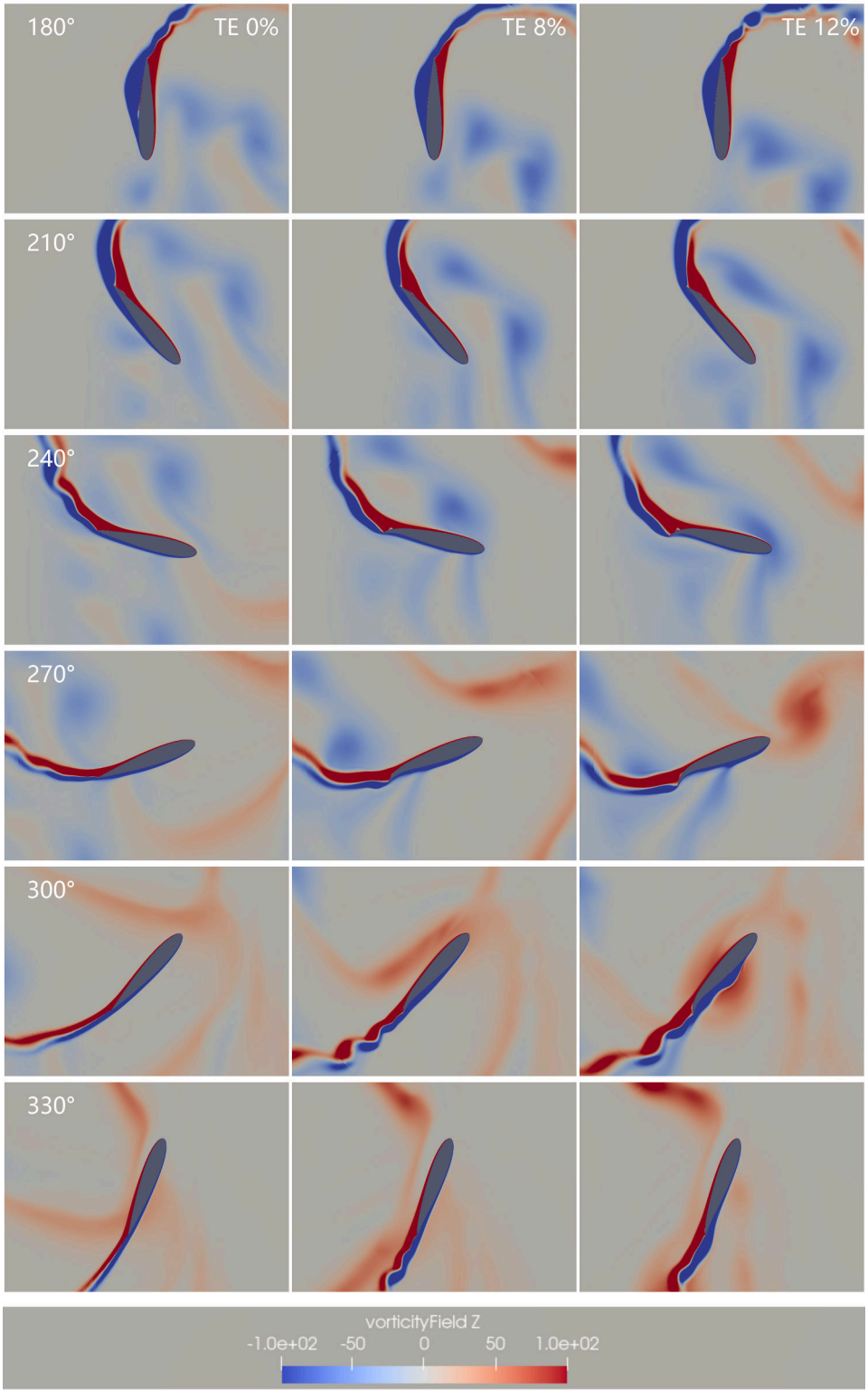

Figure 4.7: Vorticity field for for cases with different TE camber degree, $180° < \psi < 330°$.

performance.

More detailed information about the flow field and its corresponding influence on the pressure distribution would be presented in the next section.

4.1.3 Pressure Distribution along the Chord

The combined effect of pitching motion of the blade, the formation of the vortex as well as the intensified downwash velocity results in the variation of the pressure distribution on the blade surface. Figure 4.8 and 4.9 present the pressure distribution versus azimuth angle for both baseline and the case with 8% and 12% cambered cases. Combining with the vertical thrust and power variation (Fig. 4.4), the downwash velocity (Fig. 4.5), and vorticity contours (Fig. 4.6 and 4.7), following information can be obtained:

- $0° < \psi < 45°$: the negative vertical thrust is provided in this region due to the travel direction and the relatively small effective angle of attack. As the blade pitches up (clockwise), both the AoA and the generated vertical thrust experience a rapid increase. Besides, the flow is attached for both cambered and baseline cases.

- $45° < \psi < 90°$: the blade is still pitching up in this interval. As a result, the effective AoA and corresponding lift generation would continue to grow. Besides, a strong suction peak appears at the leading edge of the inner surface (suction side), which results in a vertical thrust peak near the top position of the trace.

  As the camber degree increases, the boundary vorticity bends due to the deformed geometry. As a result, vortex shedding occurs in the vicinity of trailing edge near the position of $\psi = 60°$. Moreover, the cambered airfoil shows a lower negative pressure at the inner surface (pressure side) and a higher value of positive pressure at the outer side (suction surface) at the trailing edge. Therefore, a positive vertical lift could be obtained at the rear part of the airfoil.

- $90° < \psi < 160°$: the decrease of pitching amplitude leads to a rapid reduction in lift. All cases experience the formations and developments of leading edge vortex (LEV).

  For the baseline case, the LEV appears at the position $\psi = 120°$, which develops rapidly and spans over the whole outer surface (suction side). Moreover, for cases with curved airfoils, the formation of the vortex is slightly delayed. In detail, in the case of 8% and 12% TE camber, the formation of the LEV occurs at the position of $\psi = 126°$ and $\psi = 132°$. In addition, the size of the vortex is slightly reduced, which accounts for a higher lift peak at the leading edge for the outer side as well.

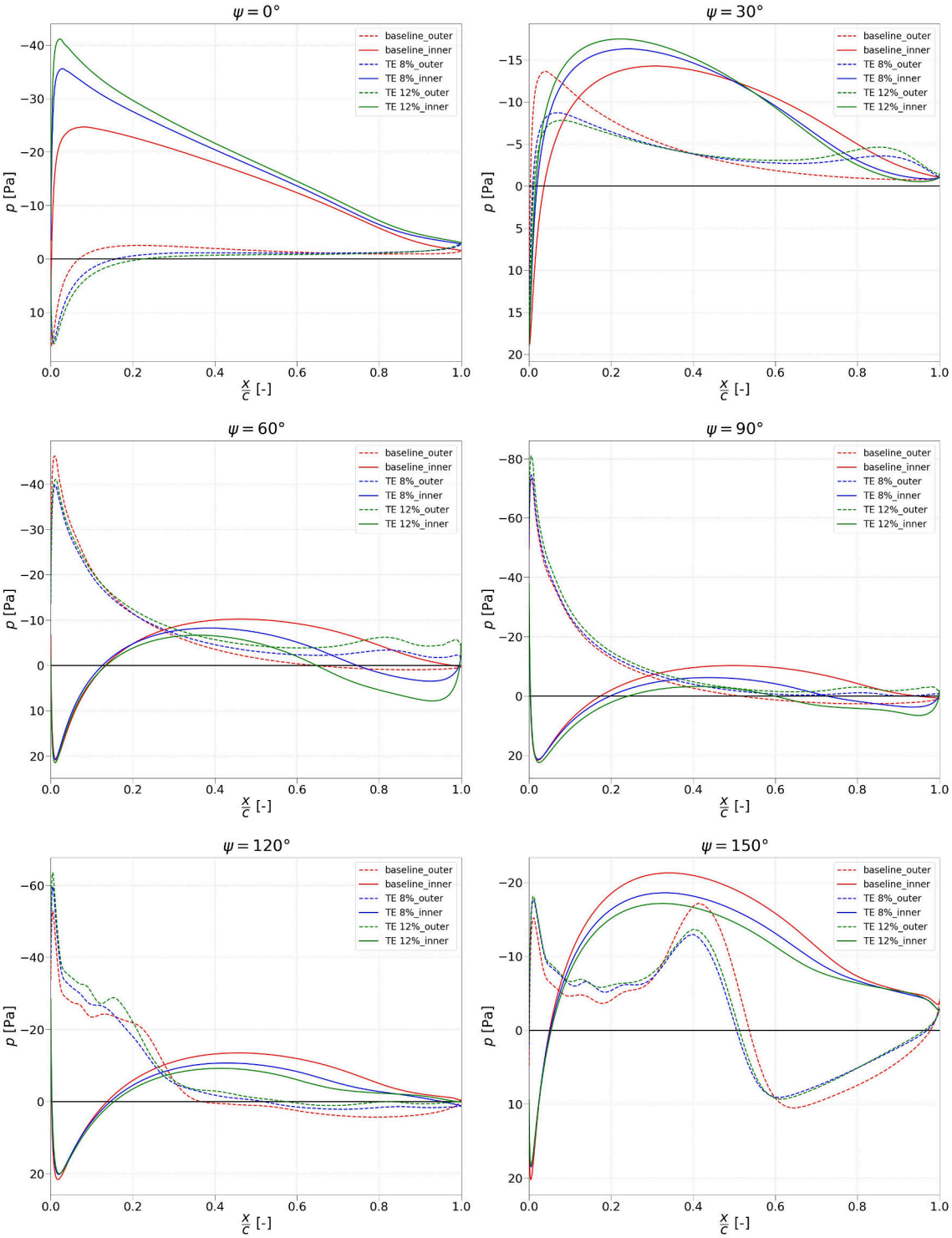

Figure 4.8: Pressure distribution for cases with different TE camber degree, $0^\circ < \psi < 150^\circ$.

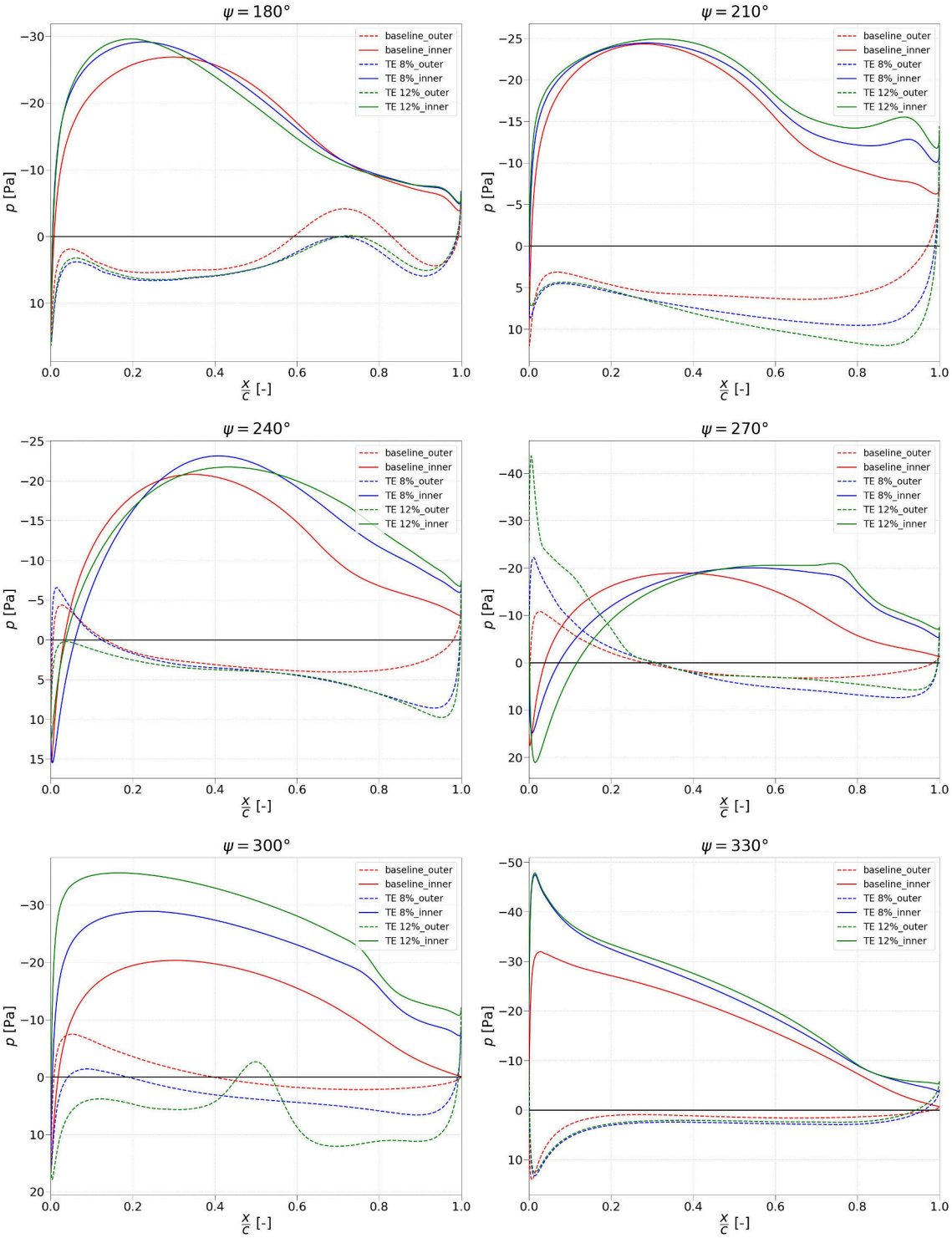

Figure 4.9: Pressure distribution for cases with different TE camber degree, $180^\circ < \psi < 330^\circ$.

- $160° < \psi < 230°$: the rapid increment in lift could be observed for all cases due to the increasing pitching angle. Particularly, when the blade is in the lower half of its trace, it will change its pitching direction from clockwise to counter-clockwise direction, which mitigates and eventually eliminates the LEV for all cases when $\psi > 180°$.

- $230° < \psi < 270°$: the local downwash velocity in this region is approximate of the same magnitude as the tangential velocity of linear rotation of the blade, thus a significant downwash effect could be observed, which causes a negative effect on lift generating. Overall, the downwash effect exceeds the pitching effect, which leads to a descending in AoA and lift generation for all cases.

- $270° < \psi < 300°$: the downwash effect is gradually eliminated, therefore both the inflow velocity and the AoA will return to relatively higher values in this area. Consequently, significant increase in vertical thrust generation and power consumption could be expected for all cases.

  For the case with cambered TE, due to the intensified downwash effect and the morphing configuration, larger pressure differences between the inner and outer surface and correspondingly higher vertical thrust generation could be obtained with the increasing TE camber degree in this region

  Moreover, the blade vortex interaction (BVI) effect becomes important for the case with large TE camber degree. In particular, as shown in Fig. 4.7, in the case of 12% TE camber, the LEV is induced on the outer surface (pressure side) when the blade is passing through the vortex shedded from the preceding blades. Consequently, a depression of the pressure in the middle of the chord on the outer surface (pressure side) is observed in this situation.

- $300° < \psi < 360°$: as the blade pitches down, the effective AOA will decrease. Combining with the reduced downwash velocity, a rapid decrease in vertical thrust would be expected in this region.

4.2 Effect of Start Location of Morphing

The start position of morphing plays an essential role in the aerodynamic performance of airfoils with the cambered trailing edge. In particular, 5 cases with different start positions of trailing edge camber (p), varying from 0.1 to 0.8, are investigated in this section. In addition, all cases have a identical 10% camber degree for the upper and lower half, i.e., $m_U = m_L = 10\%$.

4.2.1 Force and Power Analysis

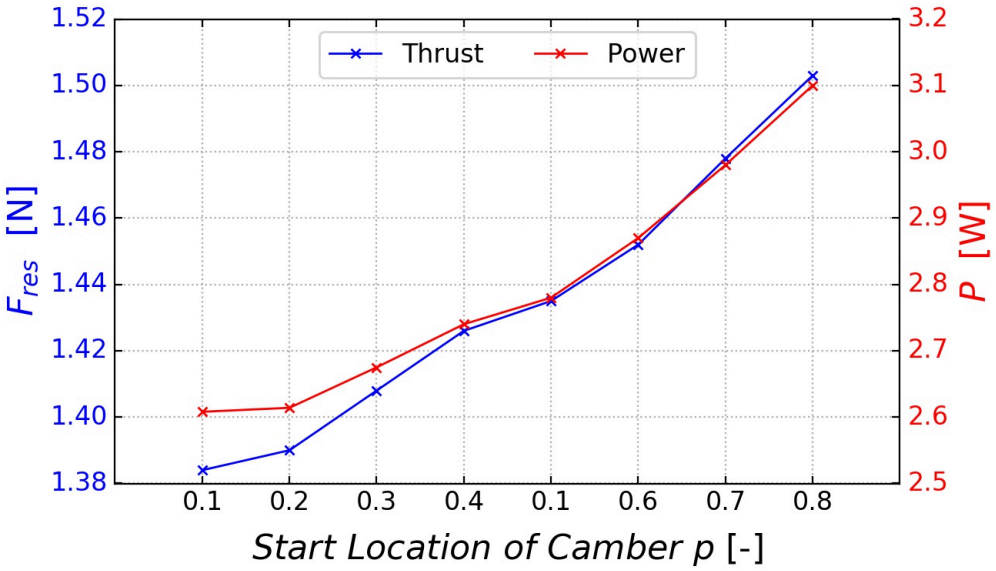

Figure 4.10: Thrust and power prediction vs. start location of TE camber, $m = 10\%$.

As shown in Fig. 4.10, a slight growth in resulting thrust is obtained, while the required power experiences a more significant increase as the start location for TE camber moves backwards. In addition, for the cases $p = 0.2$, $p = 0.4$, $p = 0.6$, and $p = 0.8$, 64.9%, 69.2%, 72.2%, and 78.3% gain in thrust, as well as 58.5%, 66.3%, 73.8%, and 88.4% more required power are observed, respectively. Besides, the power increment surpasses the gain in thrust when $p > 0.6$.

The efficiency results are included in Fig. 4.11. From the figure, a slight increase followed by a descending trend is observed for both FoM and PL. Moreover, the best efficiency is achieved by the case with $p = 0.2$, where 33.8% higher value of figure of merit, and 4.11% higher value power loading is obtained.

The variation of vertical force of one blade for cases with different start positions of TE camber is shown in Fig. 4.12. From the figure, the lift fluctuation caused by the change of start position of TE camber is limited, and all cases with cambered trailing edge developed in this section show consistent variation patterns. Furthermore, the curves of the cases almost overlap with each other in most of the intervals. Specifically, in the case of $p = 0.7$ and $p = 0.8$, as the start locations of TE camber move backwards, the ascending peak value of the vertical thrust at the positions $\psi = 230°$ and $\psi = 300°$ will lead to an overall increment in vertical thrust generation for these two cases.

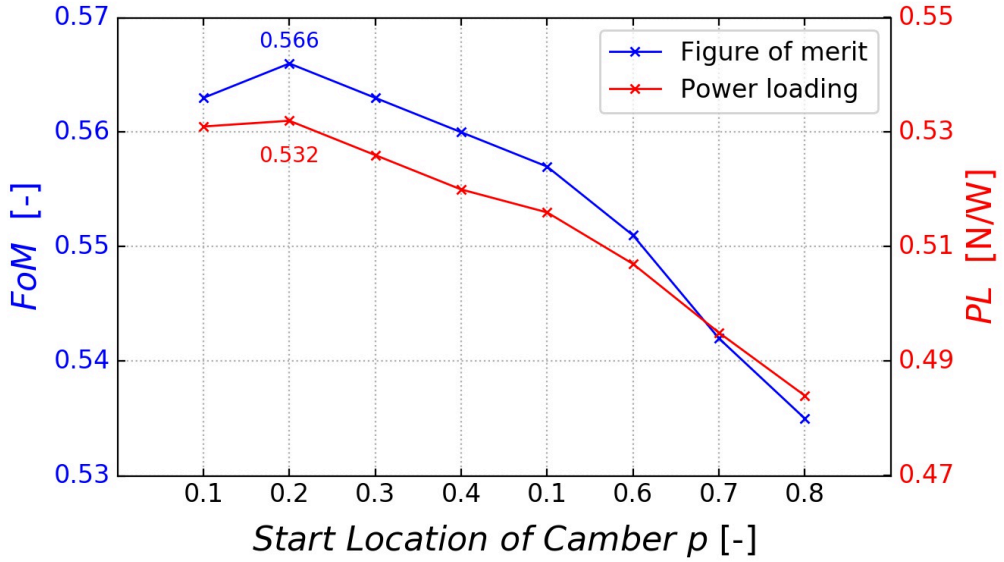

Figure 4.11: Efficiency prediction vs. start location of TE camber, $m = 12\%$.

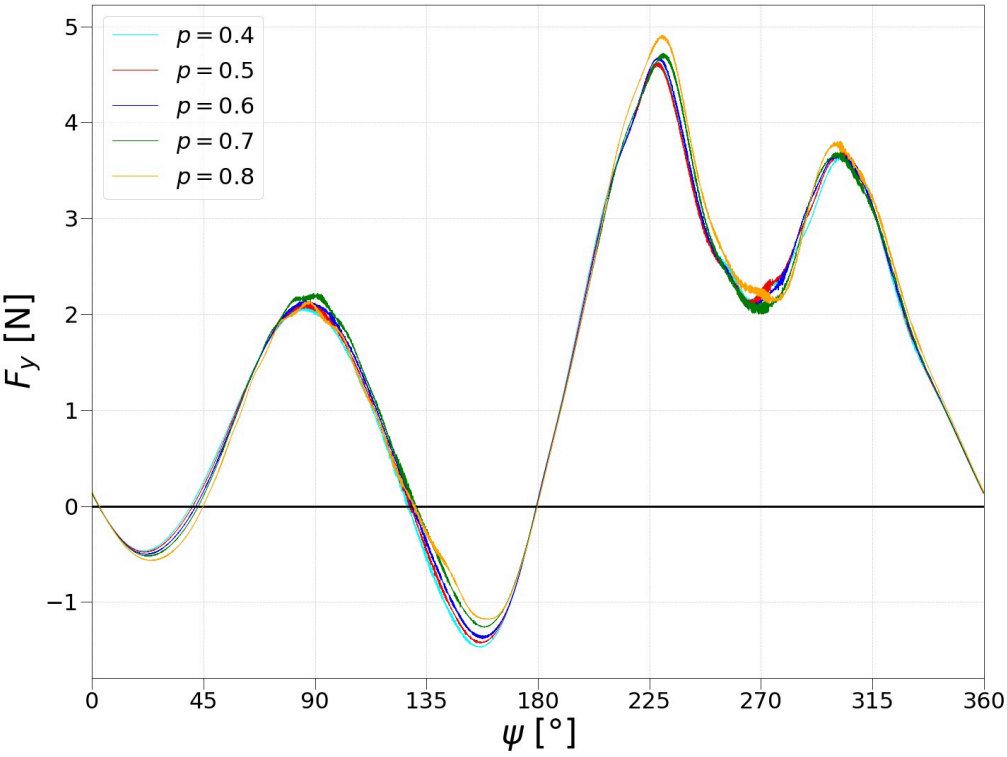

Figure 4.12: Vertical thrust distribution for one blade with different start position of TE camber.

4.2.2 Flow Field Visualization

The downwash velocity distribution for the cases of TE camber with different start positions of morphing is presented in Fig. 4.13. From the figure, as the start position of the trailing edge camber moves backwards, the flow field experiences a slightly intensified downwash velocity in the lower end of the trajectory. Meanwhile, the thrust angle varies from 98.56° ($p = 0.4$) to 100.40° ($p = 0.6$) and 102.95° ($p = 0.8$). As a consequence, a counter-clockwise shift of the area affected by downwash velocity could be observed.

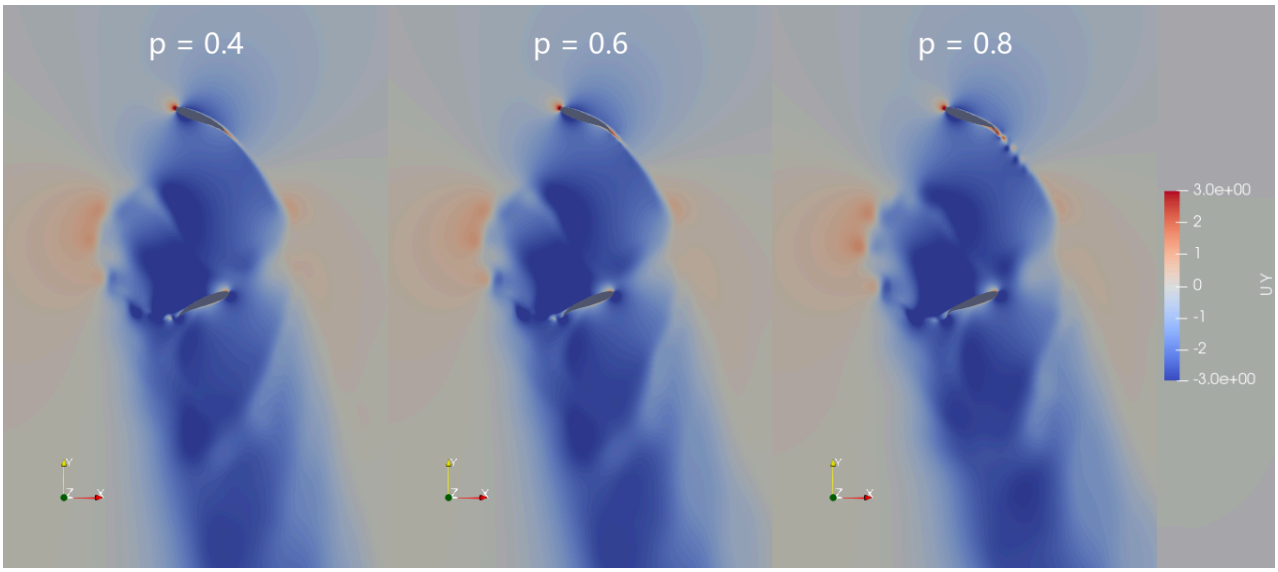

Figure 4.13: Downwash velocity for cases with different start position of TE camber.

The vorticity contours for airfoils with different start positions of TE camber are shown in Fig. 4.14. From the figure, the vorticity distribution on the surface of the blades shows similar behaviours. Particularly, the formation of LEV near the position $\psi = 130°$ could be observed for all cases. Besides, the vortex develops and occupies the entire outer surface near the position $\psi = 175°$. Moreover, for the lower half of the trajectory, i.e., $180° < \psi < 360°$, fluid flows smoothly on the surface of airfoils with different start positions of TE camber, no signs of vortex are appearing in this region. The major difference occurs in the wake region, specifically:

- when the blade is moving through the upper part of its trace, i.e., $0° < \psi < 180°$, the boundary vorticity fluctuation in the wake region appears at the position of $\psi = 60°$ in the case of $p = 0.8$, then the boundary vorticity rolls up into an array of positive (counter-clockwise) vorticity. Consequently, the shedding vortex in the wake region could be observed at the position of $\psi = 80°$. As the camber position moves forward, the appearance of boundary fluctuation and

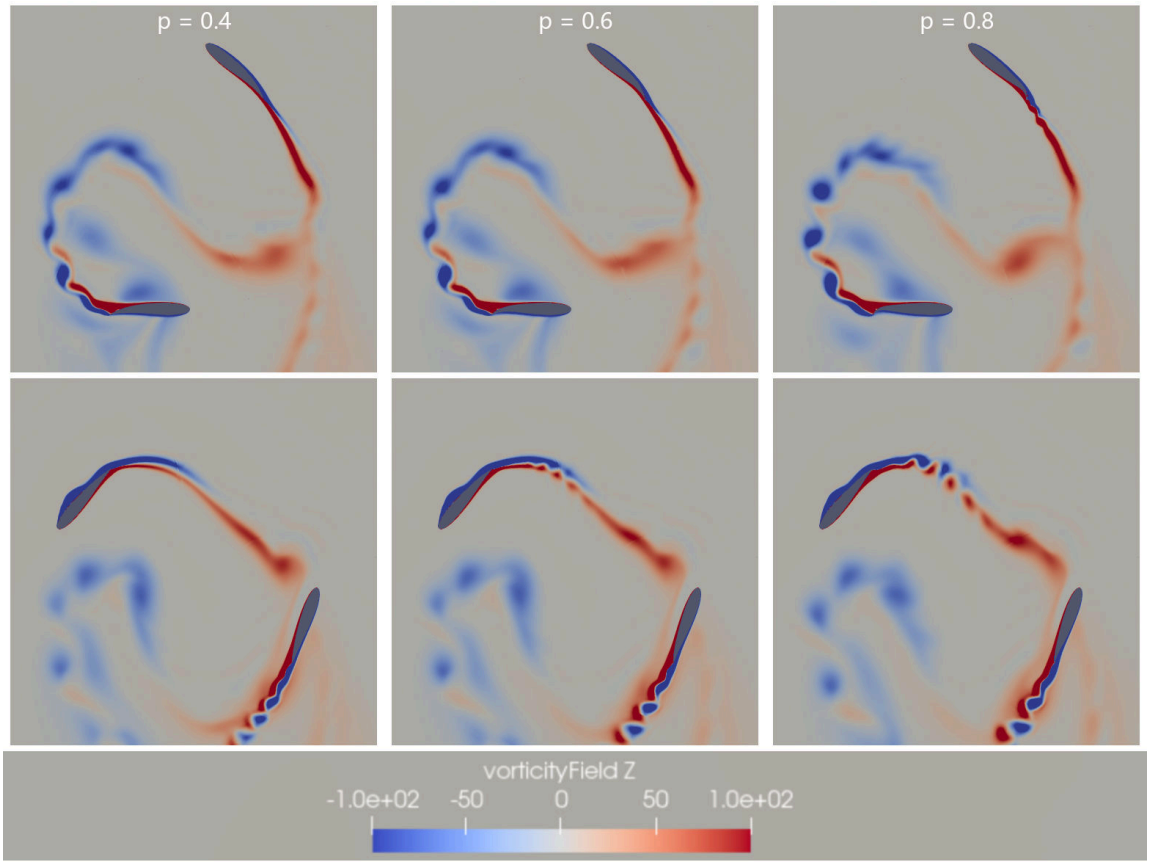

Figure 4.14: Vorticity field for cases with different start position of TE camber.

the vortex shedding is delayed or even eliminated. Particularly, in the case of $p = 0.4$, no signs of vortex shedding in the upper half can be observed.

- when the blade is moving through the lower part of its trace, i.e., $180° < \psi < 360°$, an array of negative (clockwise) vorticity in the wake region and the vortex street could be observed for all cases. Moreover, the vorticity in this region is diminished as the start position of trailing edge camber moves forwards.

More detailed unsteady phenomena and the corresponding influence on the pressure distribution is presented in the next section.

4.2.3 Pressure Distribution along the Chord

The pressure distributions of airfoils with different start positions of TE camber are shown in Fig. 4.15. From the figure, the variation of pressure distribution caused by the change of start position of the TE camber is not significant. Besides, the major differences occur at the trailing edge. As the start position of the TE camber moves backwards, the pressure differences between the upper and lower surface at the highest $\psi = 90°$ and lowest points $\psi = 270°$ increase slightly, which leads to a slight growth in lift generation. Moreover, the pressure distributions on the blade surface coincide with each other, except for the trailing edge section.

4.3 Effect of Asymmetric Camber Morphing

As illustrated in the previous sections, the blades with cambered TE behave differently at the upper and lower half of the trajectory due to the influence of downwash velocity and other effects. In this section, we investigate the aerodynamic performance of five cases with asymmetric trailing edge camber morphing. Specifically, cases have different maximum camber degrees m_U at the top and bottom m_L of the cycle. In addition, all cases have an average of 10% camber degree of the upper and lower parts and the morphing camber of all blades developed in this section starts at the position of 70% chord, i.e., $p = 0.7$.

4.3.1 Force and Power Analysis

The results of the resultant force and required power of airfoils with asymmetric cambered TE are shown in Fig. 4.16, where the digit after U and L denote the value of m_U and m_L in percentage respectively. From the figure, both resultant thrust and required power show a descending trend

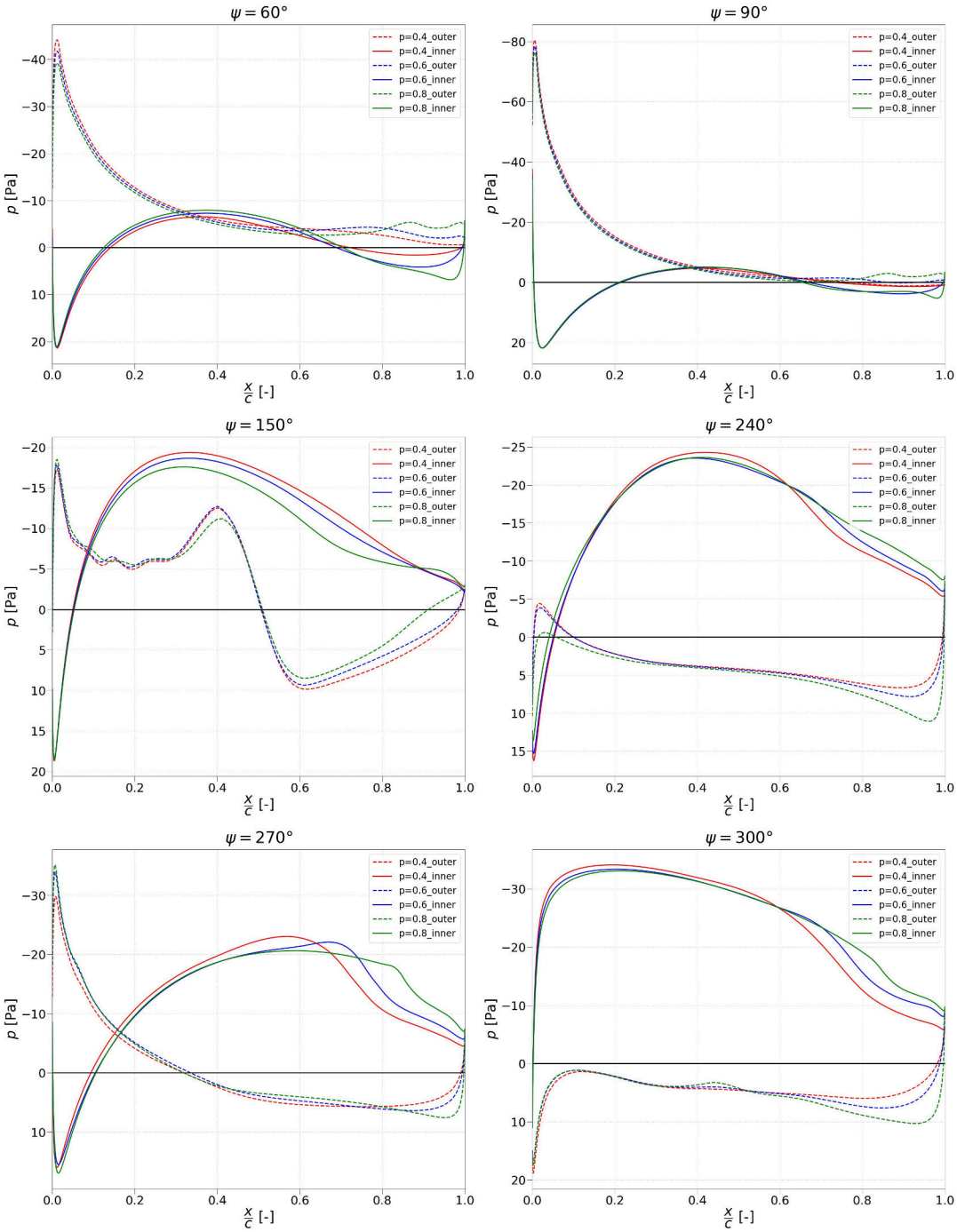

Figure 4.15: Pressure distribution for cases with different start position of TE camber.

as more camber for the upper half and less camber for the lower half are introduced into the rotor system.

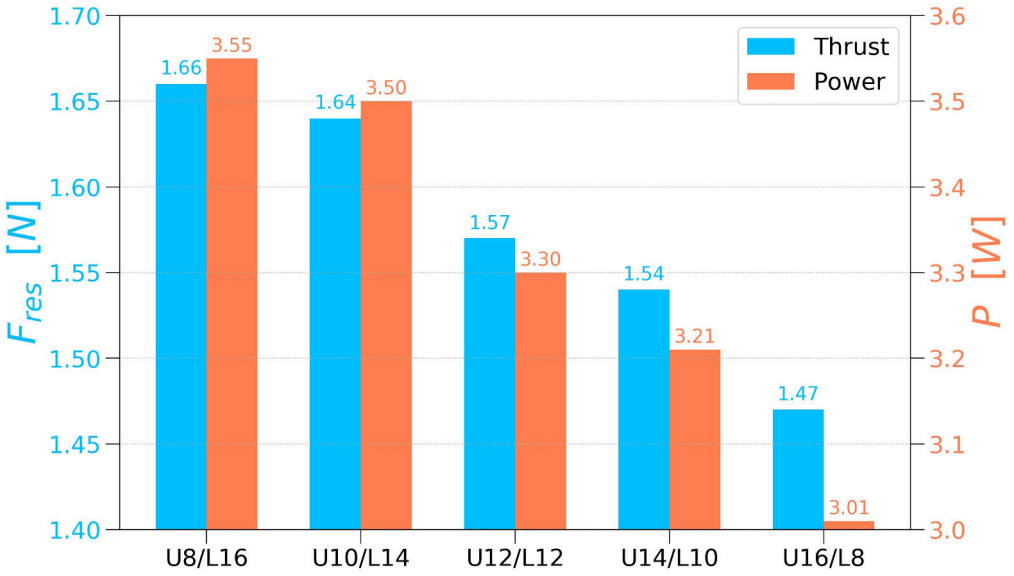

Figure 4.16: Thrust and power prediction for cases with asymmetric cambered TE.

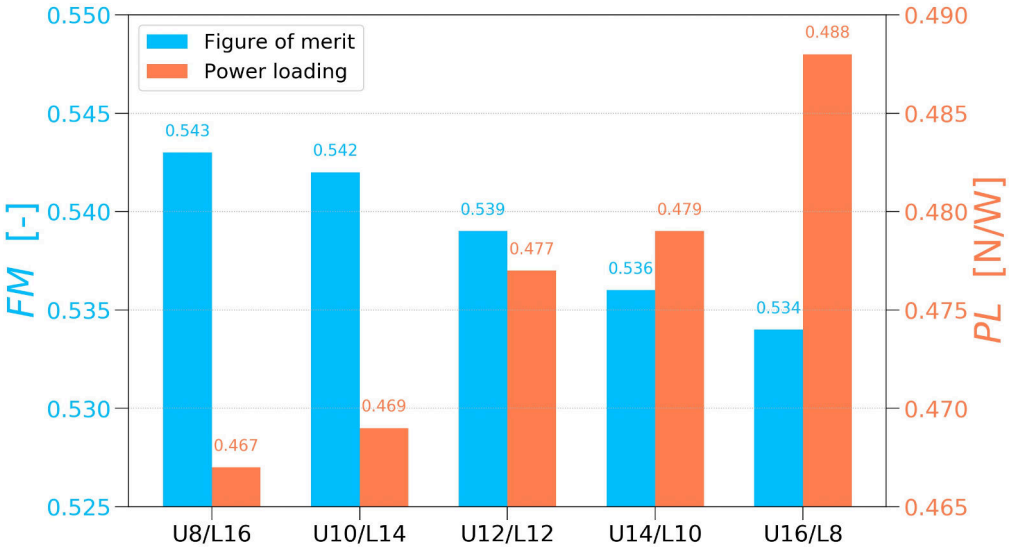

Figure 4.17: Efficiency prediction for cases with asymmetric cambered TE.

Fig. 4.17 illustrates the variation of efficiencies of airfoils with asymmetric cambered TE. Particularly, the value of the figure of merit shows a slightly descending tendency with the increasing m_U and the decreasing m_L. On the contrary, the value of power loading increases continuously. The case of U8/L16 shows the best results of figure of merit (28.4% higher than the baseline case) but the

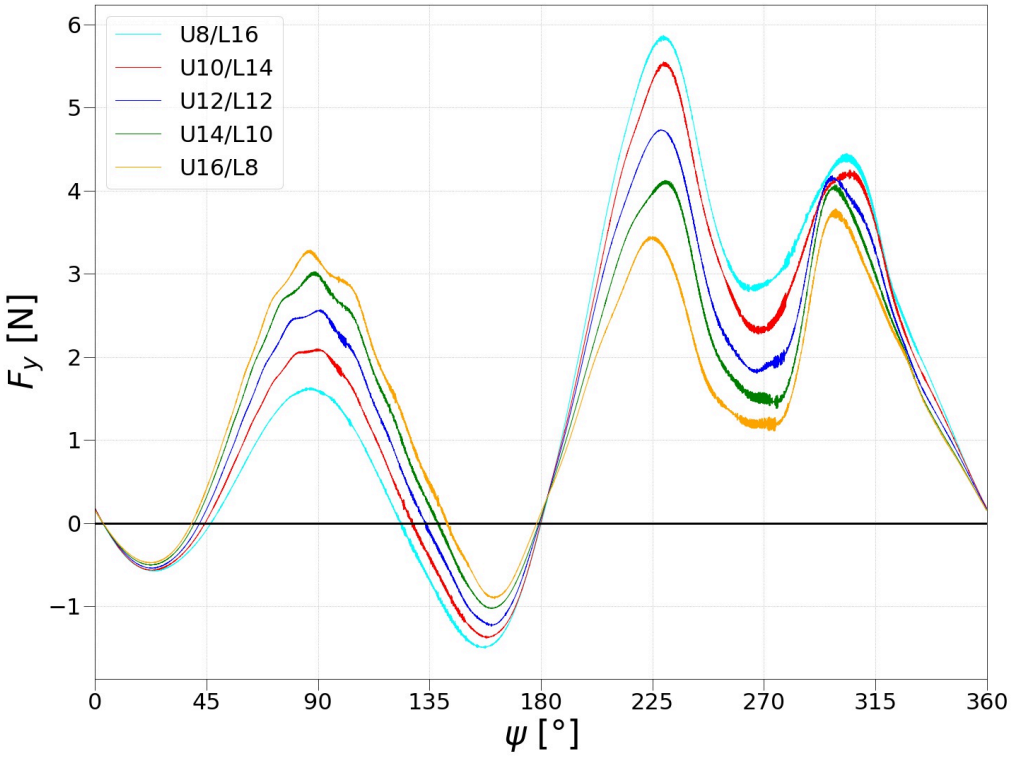

Figure 4.18: Vertical force distribution for one blade for cases with asymmetric cambered TE.

worst results of power loading (8.61% less than the baseline case), while the case U16/L8 achieves the highest value of power loading (4.5% less than the baseline case) and the lowest value of figure of merit (26.2% higher than the baseline case).

The variation of vertical force for one blade of cases with asymmetric cambered TE is shown in Fig. 4.18. From the figure, three peaks of lift generation near $\psi = 85°$, $\psi = 230°$, and $\psi = 300°$ could be observed for all cases. Besides, the peak value is related to the corresponding camber degree m_U and m_L. Especially, more camber at the upper part and less camber at the lower part, i.e., $m_U > m_L$, means better performance at the upper half and worse performance at the lower half concerning lift generation.

Furthermore, in the case of U8/L16, the contribution of lift generation of the upper part is still small, and most of the vertical thrust is produced at the lower half of the cycle. Moreover, the second lift peak, at the position of $220° < \psi < 235°$, shows the greatest peak value, which is significantly higher than the value of the other two peaks. However, as more camber for the upper half and less camber for the lower half are introduced, the gap between peak values diminishes, and the lift will be more evenly distributed over the rotation. What is more, in the case of U16/L8, the lift value of the third peak at $\psi = 300°$ exceeds the previous peak and reaches the global maximum of the

entire cycle. At the same time, the cases with a smaller m_L show a steeper slope in the interval of $270° < \psi < 300°$, thus the location of the third peak would slightly move downstream as more camber is introduced.

4.3.2 Flow Field Visualization

The downwash velocity contour for the case with asymmetric cambered TE is shown in Fig. 4.19. From the figure, for the case U8/L16, i.e., $m_U = 8\%$ and $m_L = 16\%$, more intensified and concentrated downwash velocity could be observed in the lower right part of the trajectory $270° < \psi < 290°$. On the contrary, for the case U16/L8, i.e., $m_U > m_L$, a more dispersed distributed area affected by the downwash velocity could be observed in the lower right part of the trajectory $260° < \psi < 320°$. It is worth to mention that an enlarged area will be affected by the downwash phenomenon in this situation.

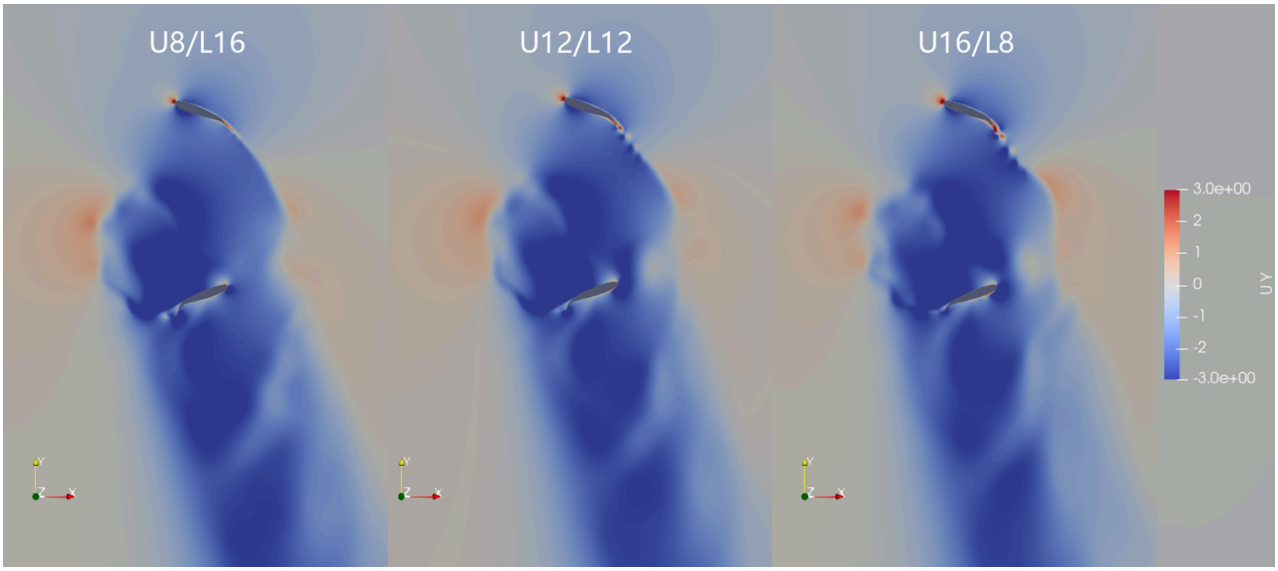

Figure 4.19: Downwash velocity for cases with asymmetric cambered TE.

The vorticity contours of the cases with asymmetric cambered TE are shown in Fig. 4.20. As depicted in the figure, when the blade is passing through the upper part of its trace, the major different behaviour occurs in the left part of the cycle. Particularly, for the case with more camber at the upper part, i.e., $m_U > m_L$, boundary vorticity of the inner surface rolls up into an array of vorticity near the highest points, subsequently, the vortex shedding in the wake region could be seen. Moreover, an enlarged leading edge vortex at the position $130° < \psi < 180°$ on the outer surface is observed for the case U16/L8.

When the blade is in the lower half of the trajectory, the major difference appears in the lower end

($260° < \psi < 310°$) of its trace. Besides, in the cases with more camber at the lower part (U12/L12 and U8/L16), the boundary vorticity is slightly thickened due to the negative vortex shedding at the position $\psi = 260°$, and the thickened boundary is disturbed by the cambered TE. Therefore, a pair of vortex street shedding into the wake region is observed in the lower right part at $\psi = 302°$. However, for the case U16/L8, the leading edge separation bubble forms at the position of $\psi = 252°$. Moreover, the blade encounters the vortex shedding from the preceding blade at the position $\psi = 280°$. As a result, the leading edge vortex is induced at the position $\psi = 300°$, which results in a great change in the local pressure distribution.

More detailed information about the unsteady phenomena and their corresponding influence on the pressure distribution is introduced in the next section.

4.3.3 Pressure Distribution along the Chord

The pressure distributions versus azimuth angle for both baseline and cases with asymmetric cambered TE are shown in Fig. 4.21. Combining with the vertical thrust variation (Fig. 4.18), the downwash-velocity (Fig. 4.19), and the vorticity contours (Fig. 4.20), following information can be obtained:

- At the top point of the trace, i.e., $\psi = 90°$, a higher suction peak for the outer side (suction side) and greater pressure in the middle of the inner surface (pressure side) result in a higher value of vertical force in the case with more camber in the upper part.
- When the blade is in the interval of $120° < \psi < 180°$, the development of leading edge vortex would lead to a significant increase in the negative pressure in the middle section of the outer surface (suction side). Moreover, in the case of U16/L8, the enlarged LEV is responsible for a higher peak of negative pressure, followed by a steeper reduction, on the outer surface.
- For the lower half of the cycle, i.e., $200° < \psi < 320°$, higher value of negative pressure on the inner surface and increased positive pressure at the outer surface would account for a higher second peak of vertical thrust for the case with $m_U < m_L$.
- Especially, for the case with less camber in the lower part (U12/L12 and U16/L8), LEV is induced at the position $\psi = 300°$, when the blade passes through the vortex shedding from the preceding blade. The development of the vortex results in the fluctuation of pressure distribution at the outer surface.

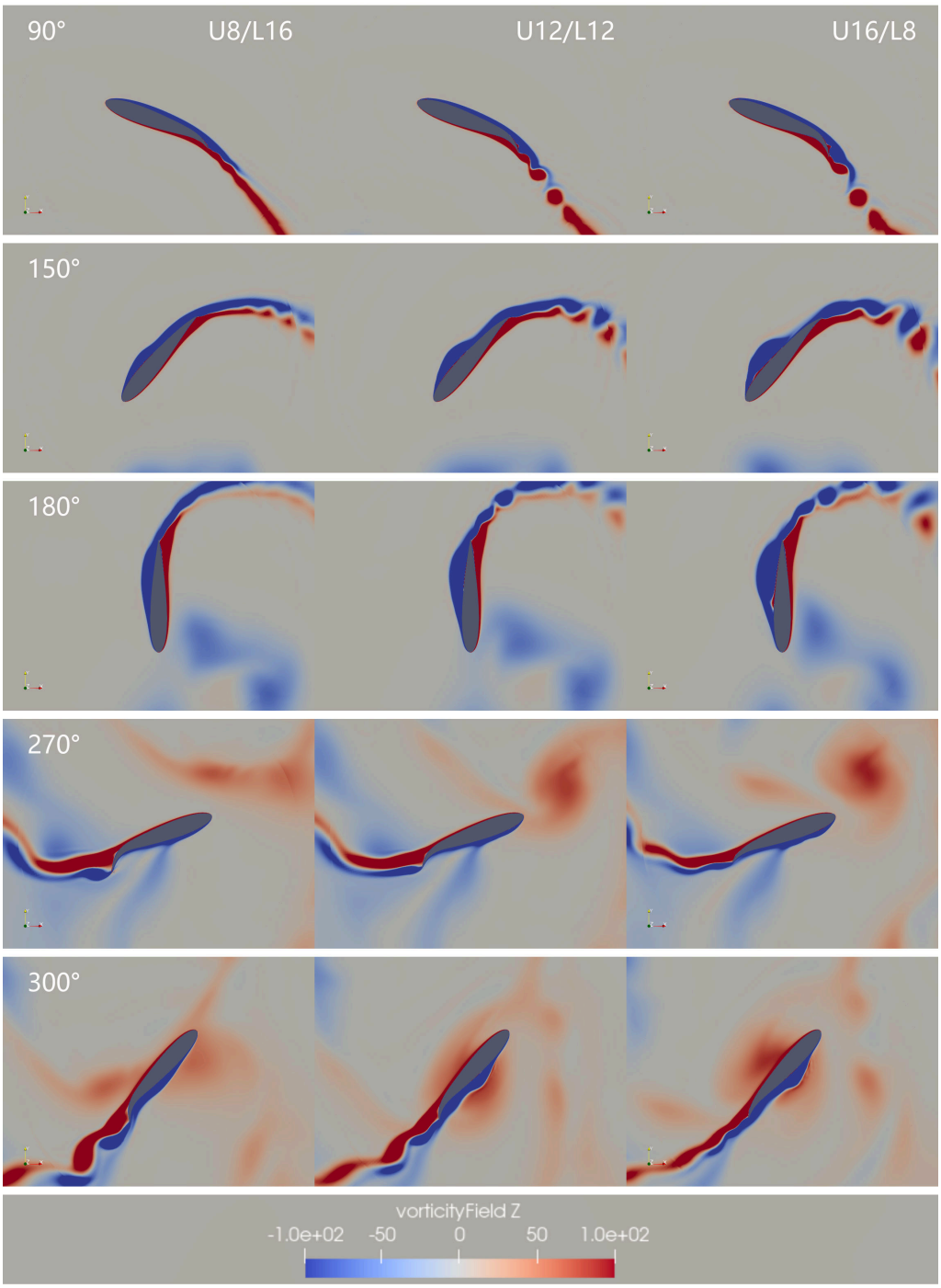

Figure 4.20: Vorticity field for cases with asymmetric cambered TE.

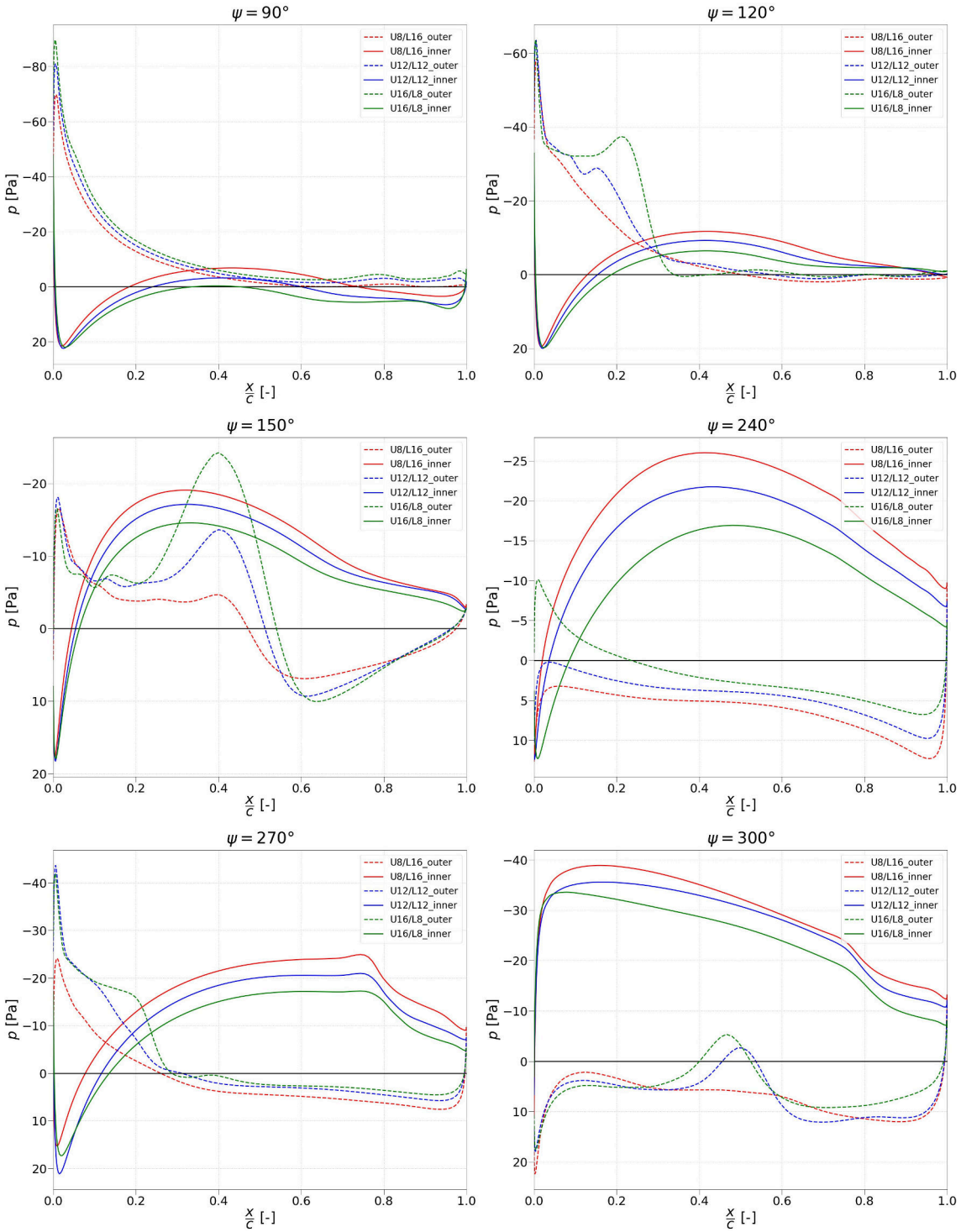

Figure 4.21: Pressure distribution for cases with asymmetric cambered TE.

5 Results of Leading Edge Morphing

The leading edge camber concept is utilized by the rotor system in this chapter. Specifically, the effect of camber degree m, the effect of end location of leading edge camber p, and the asymmetric LE camber effect are obtained in this chapter.

5.1 Effect of Maximum Degree of Camber Morphing

Firstly, the effect of camber degree is analyzed in this section. Particularly, as described in Fig. 5.1, the maximum camber degree varies from 0% to 12% of the blade chord length, and the baseline case with symmetric airfoils (NACA0015) is denoted as 0% of LE camber. Moreover, the leading edge morphing ends at the position 30% of the normalized chord, i.e., $p = 0.3$. Note that the maximum camber degrees for the upper (m_U) and lower (m_L) half are consistent in this section.

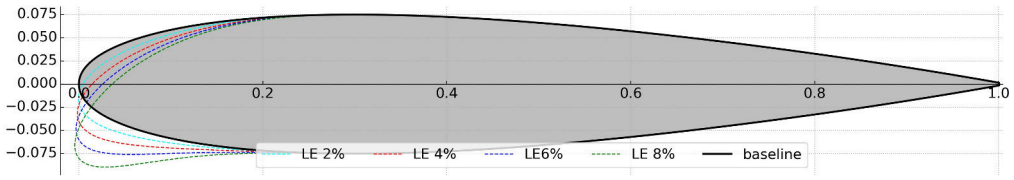

Figure 5.1: Airfoils with cambered leading edge, $p = 0.3$.

5.1.1 Force and Power Analysis

Fig. 5.2 presents the change of averaged resultant thrust F_{res} and the required power P versus the camber degree. From the figure, both the resultant thrust and the required power experience a moderate decrease with the increasing m , if the camber degree is less than 8%. Subsequently, the resultant force continues to decrease, while the required power reaches its minimum value of 1.409 (14.6% less than the baseline case) in the case of $m = 8\%$.

The results of figure of merit and power loading versus LE camber degree are illustrated in Fig. 5.3. Particularly, for the case with morphing LE, the value of both power loading and figure of merit would first increase and then decrease , as more camber is introduced. When the camber degree is less than 8%, better results for both FoM and PL are obtained in comparison to the the baseline case. However, for the case with $m = 12\%$, the increments in efficiency diminish. Besides, the best

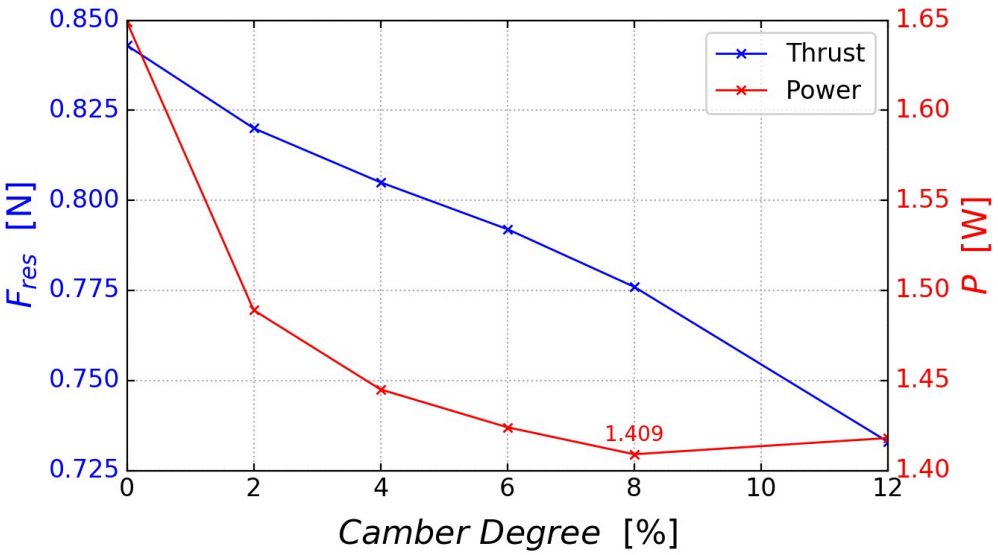

Figure 5.2: Thrust and power prediction vs. LE camber degree, $p = 0.3$.

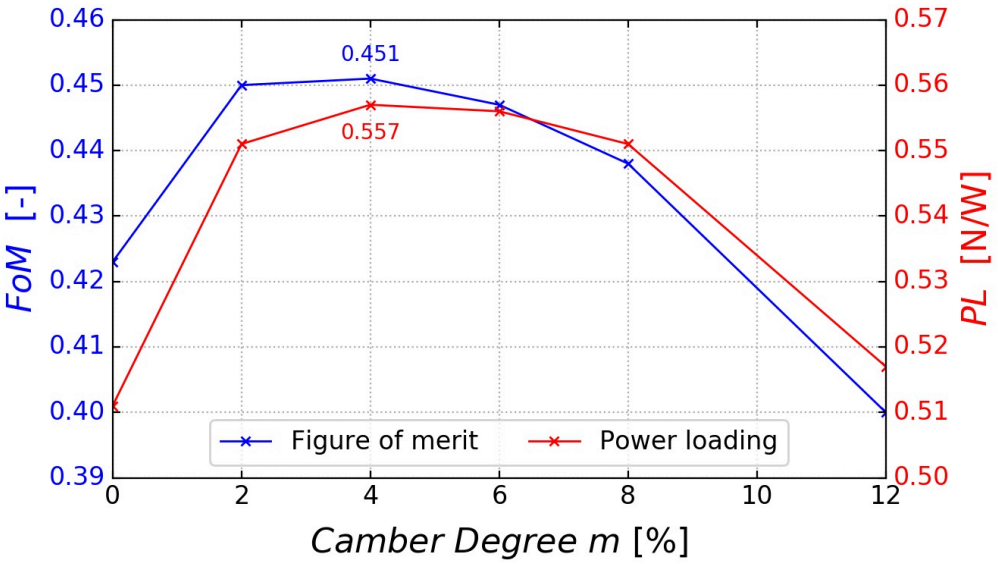

Figure 5.3: Efficiency prediction vs. LE camber degree, $p = 0.3$.

power loading result with the value 0.557 (9.0% higher than the baseline case) and figure of merit result of 0.451 (6.62% higher than the baseline case) are achieved by the case $m = 4\%$.

The variation of vertical force over the period is shown in Fig. 5.4. From the figure, both the baseline case and cases with the cambered leading edge have similar thrust variation patterns, and the curves almost overlap with each other near the intervals $-40° < \psi < 20°$ and $170° < \psi < 220°$. Specifically, when the blade is in the upper half of the trace, its contribution to the lift generation is still small for all cases. In addition, the peak value near the position $\psi = 85°$ exhibits a slight decrease with the increasing camber degree. Furthermore. the vertical thrust is mainly generated when the blade is in the lower part, especially near the interval $220° < \psi < 320°$. The plot also indicates a slight lift increment in the second and third peaks for the cambered case.

The results of the required power are shown in Fig. 5.4. In particular, the baseline airfoil exhibits a significantly higher value of required power at the upper half, due to the formation and development of the leading edge vortex. Moreover, all cases show a consistent pattern of power changes when the blade is passing through the lower half of its trace.

5.1.2 Flow Field Visualization

The downwash velocity contours of cases with different LE camber degrees are shown in Fig. 5.5. From the figure, no obvious change in velocity magnitude and its influence area could be observed. In addition, for all cases, the effect is most significant when the blade is at the lower end of the cycle. Furthermore, the thrust angle varies from 96.23° (baseline case) to 93.36° (4% LE camber) and 92.71° (8% LE camber) with increasing LE camber degree. As a result, the area affected by the downwash velocity experiences a clockwise shift in this situation.

The vorticity contours of the case with cambered LE are shown in Fig. 5.6 and Fig. 5.7. From the figure, the major different behaviour occurs in the region of $120° < \psi < 180°$.

Specifically, for the baseline case, the formation of LEV at the position $\psi = 128°$ could be observed. Subsequently, the size of the vortex grows and eventually occupies the entire outer surface (suction surface) of the blade at the position $\psi = 174°$. In addition, when the blade is in the lower half of its trace, i.e., $180° < \psi < 360°$, the fluctuation of vorticity in the wake region is observed near the lowest point of the circle. Besides, the flow is always attached to the surface of the blade in this area.

In the cases with cambered LE, there are no signs of vortex formation or severe flow separation during the entire cycle. Therefore, it can be inferred that the instability effect of the flow field is eliminated and an optimized flow field structure could be thus obtained by employing the LE camber control.

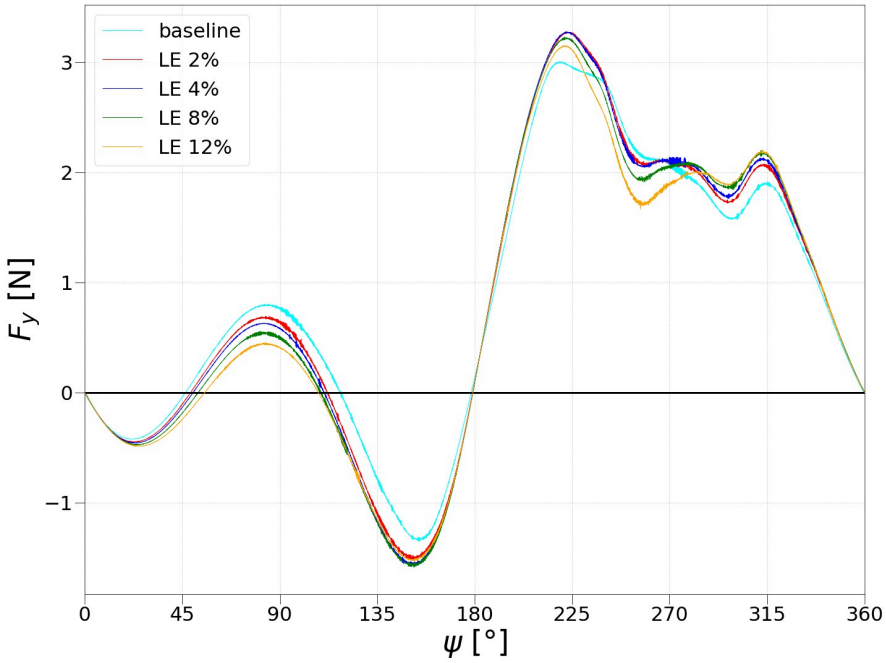

(a) Vertical force

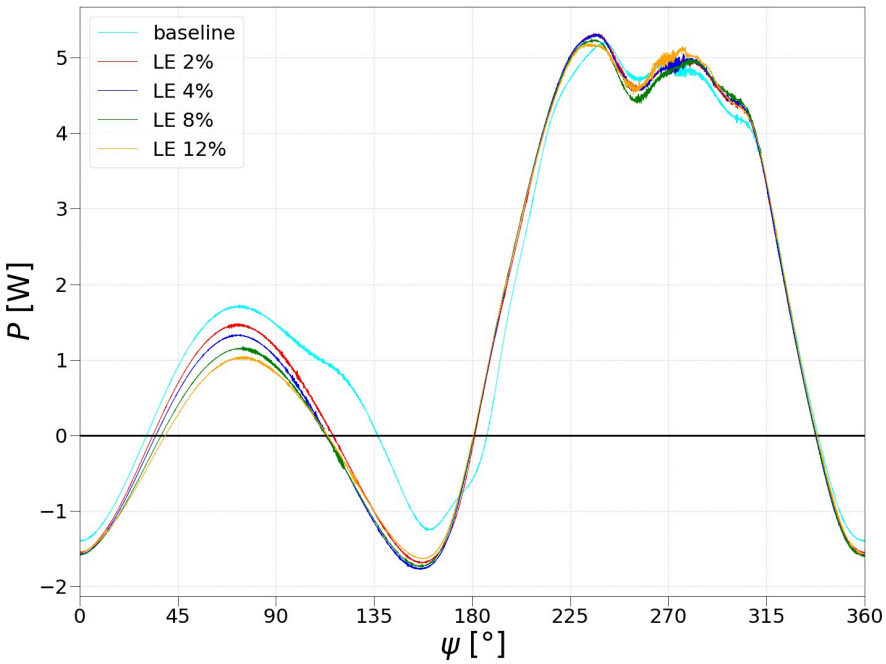

(b) Required power

Figure 5.4: Vertical thrust and power distribution for one blade with different LE camber degree.

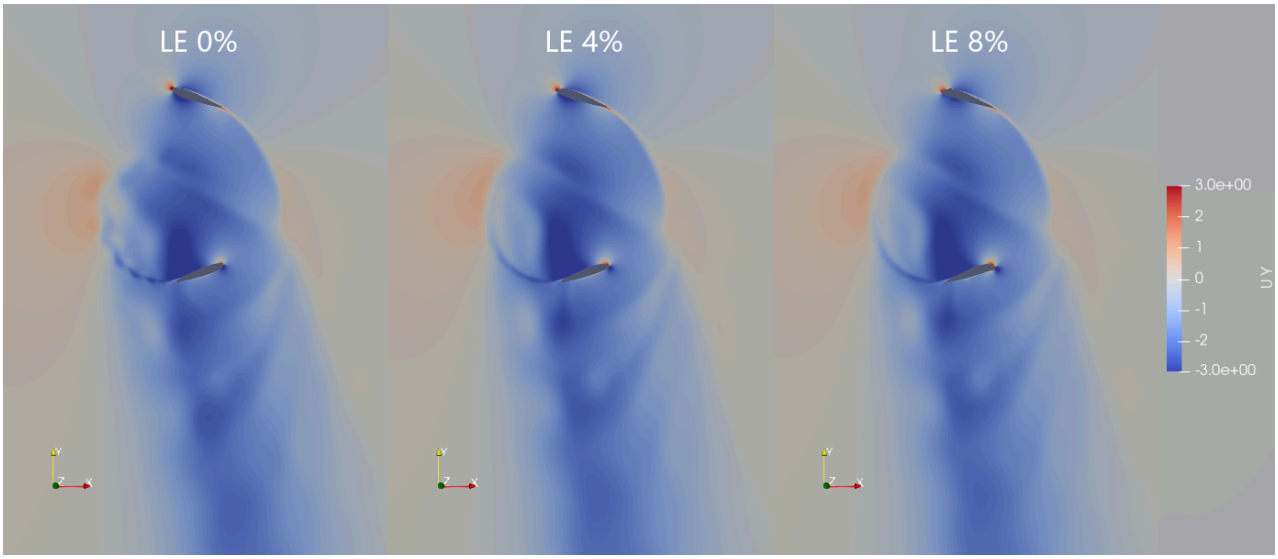

Figure 5.5: Downwash velocity for cases with different LE camber degree.

5.1.3 Pressure Distribution along the Chord

Figure 5.8 and Fig. 5.9 show the pressure distribution along the chord versus azimuth angle for both baseline and the cases with 4% and 8% cambered LE. From the figure, the pressure distribution of the inner blade shows identical behaviours, except for the major difference that occurs at the leading edge of the outer surface. Combining with the vertical thrust variation and the vorticity contours shown in the previous sections, the major difference of the pressure distribution can be summarized as follow :

- $60° < \psi < 120°$: as the LE camber degree increases, the suction peak at the outer surface (suction surface) decreases, which results in a lower vertical thrust peak for the upper part for the case with cambered LE.

- $120° < \psi < 180°$: for the baseline case, the LEV appears at the position $\psi = 120°$, which develops rapidly and shortly spans the entire outer surface (suction surface) of the aerofoil. Consequently, the fluctuation of the pressure on the outer surface (suction side) could be seen.

  For cases with curved leading edge, no formation and development of vortex are observed, which results in a lower and smoother pressure distribution at the leading edge of the outer surface (suction surface) in this region.

- $230° < \psi < 300°$: the significant downwash effect, which has a negative effect on lift generating, could be observed in this area. Overall, the downwash effect surpasses the effect of blade

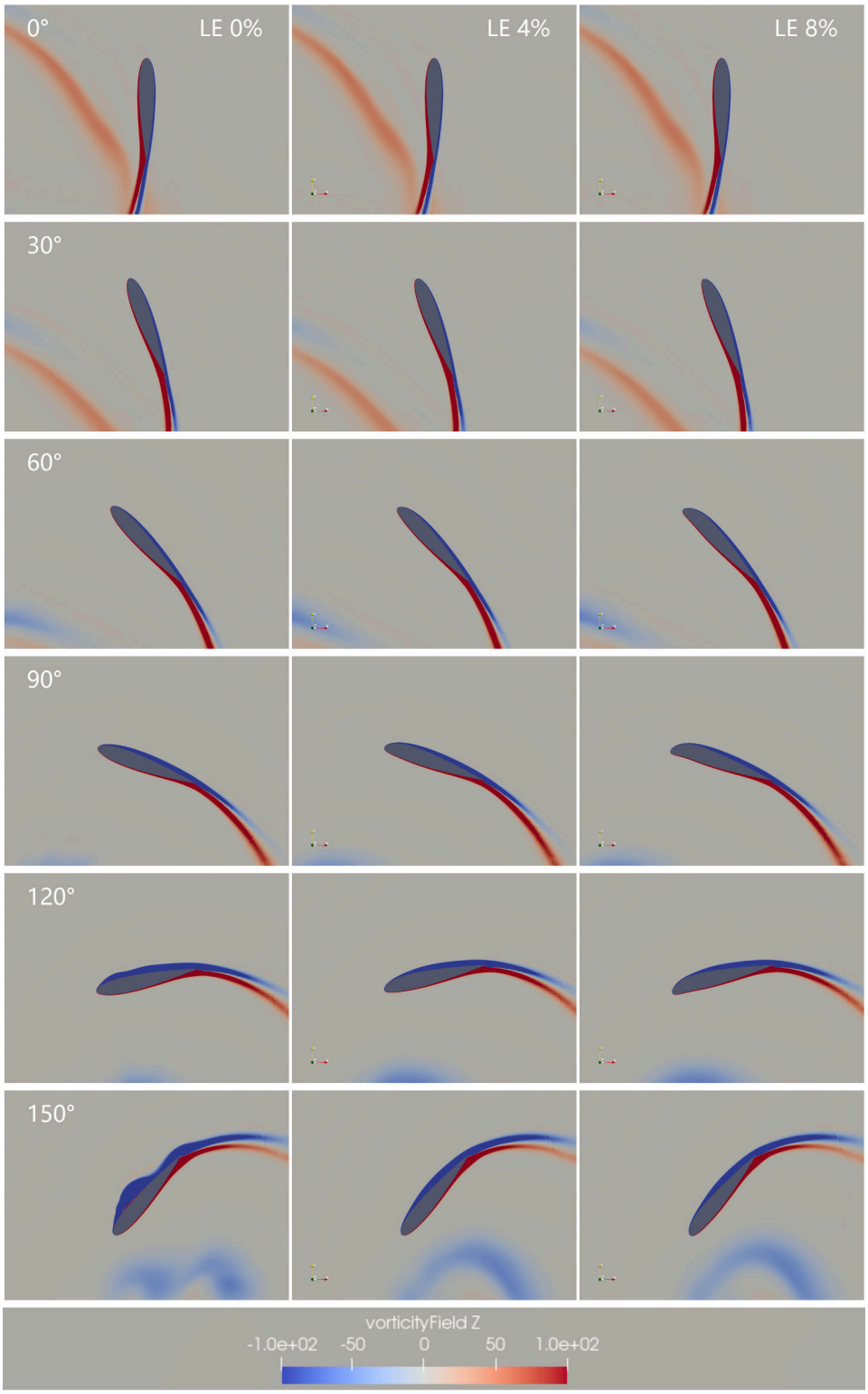

Figure 5.6: Vorticity field for cases with different LE camber degree, $0° < \psi < 150°$.

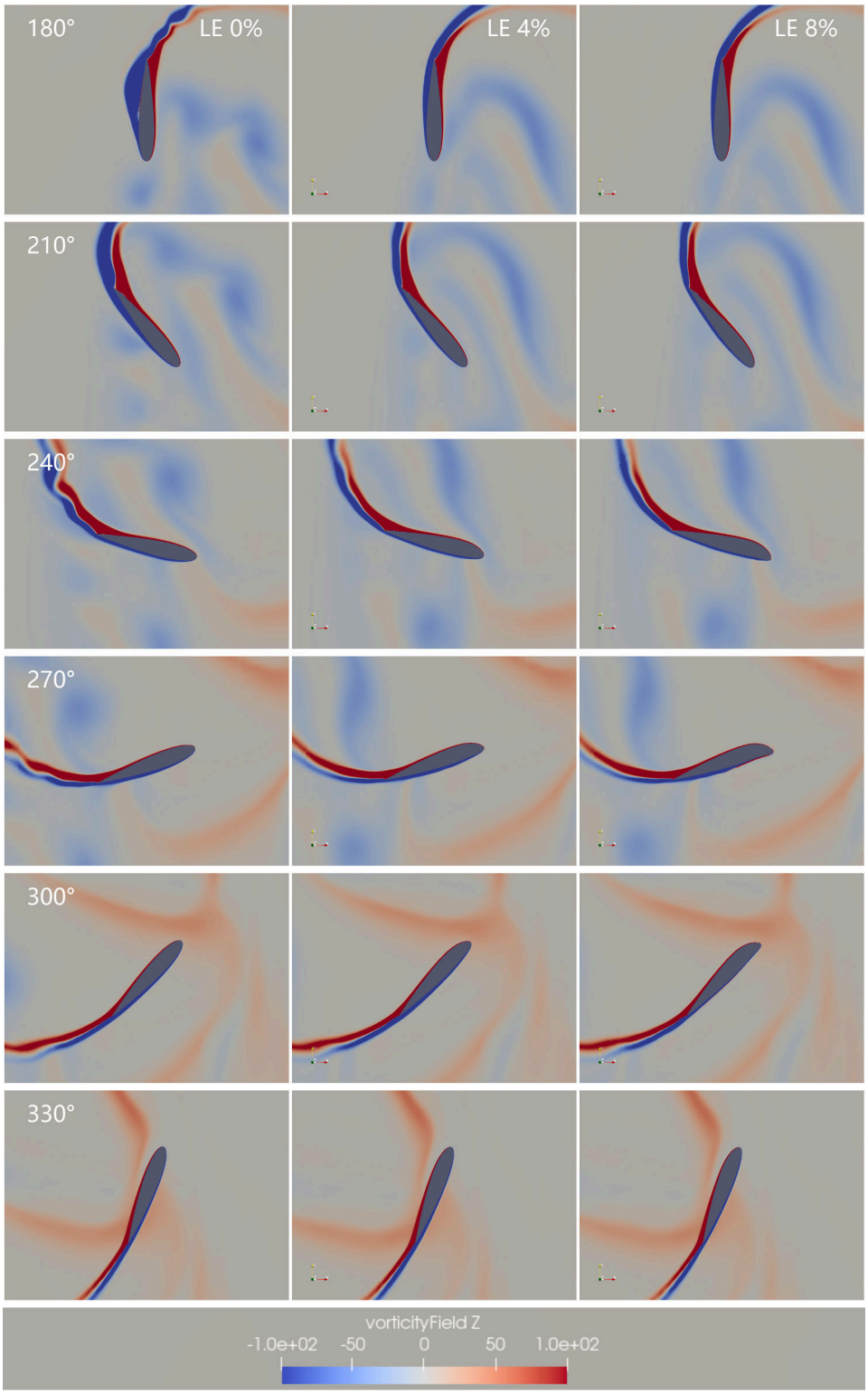

Figure 5.7: Vorticity field for cases with different LE camber degree, $180° < \psi < 330°$.

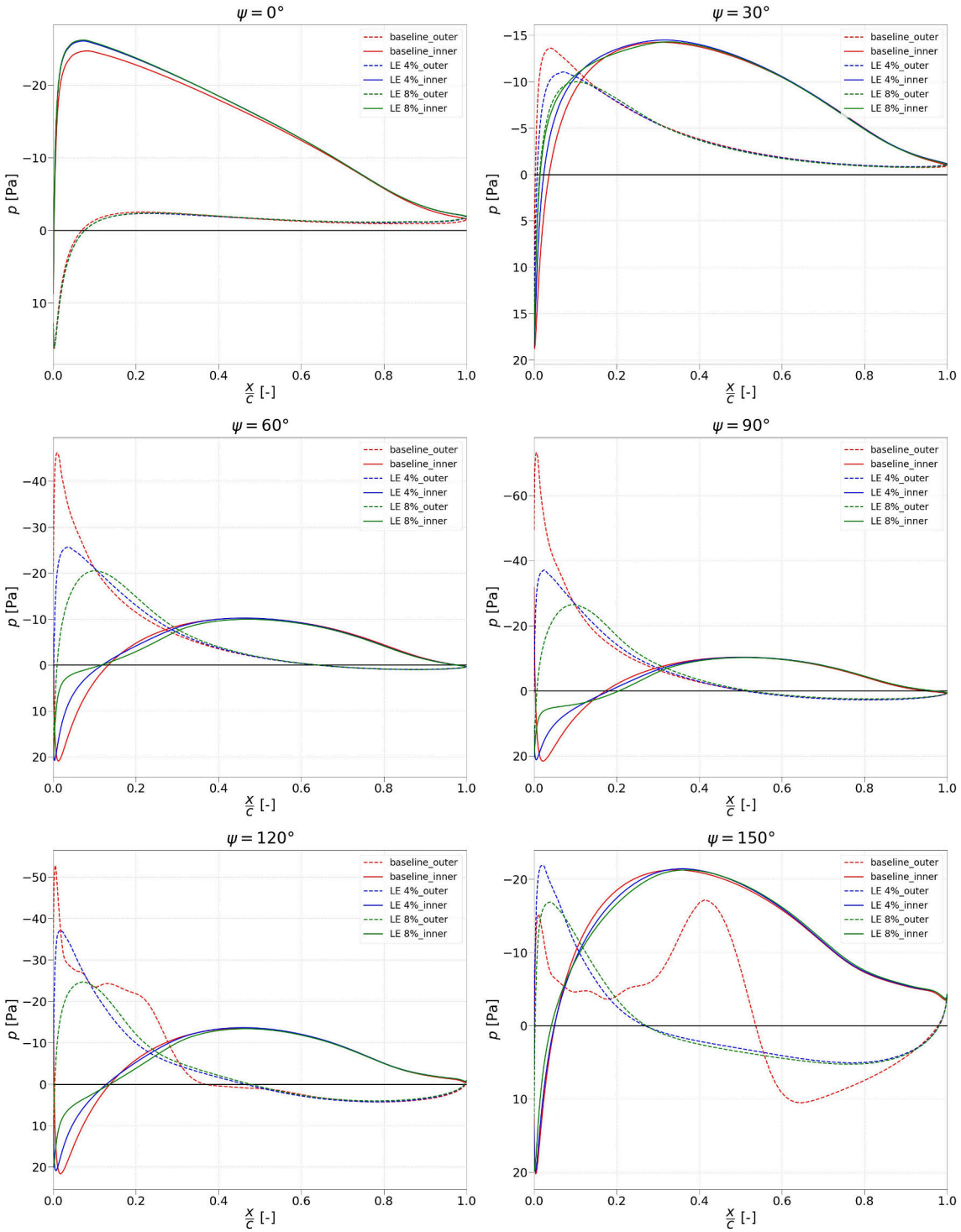

Figure 5.8: Pressure distribution for cases with different LE camber degree, $0° < \psi < 150°$.

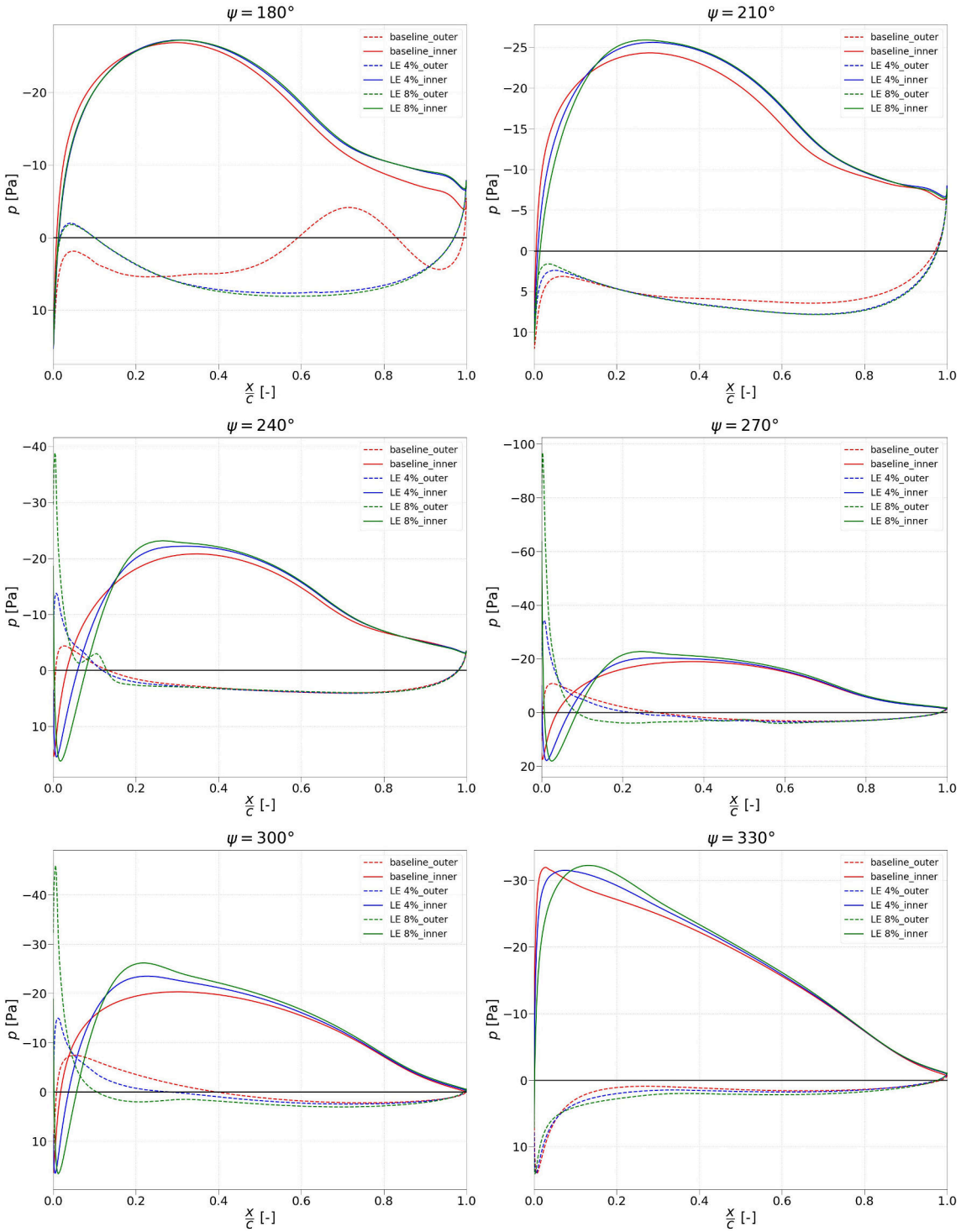

Figure 5.9: Pressure distribution for cases with different LE camber degree, $180° < \psi < 330°$.

pitching, which leads to the decrease of AoA and a sudden reduction in the lift generation for all cases.

For the case with cambered LE, significantly higher negative pressure peaks at the leading edge of the outer surface (pressure surface) are achieved as the camber degree increases. As a result, the lift exhibits a slight reduction at the lowest point of its trace.

5.2 Effect of End Location of Morphing

The end location of deflection has a great influence on the aerodynamic performance of airfoils with the morphing leading edge. In this section, the numerical simulations of 5 cases with different morphing end locations are conducted. Specifically, the end location of LE camber p varies from 0.1 to 0.5 of the normalized blade chord in this section. Besides, the maximum camber for the upper and lower half are set to be 4% for all cases, i.e., $m_U = m_L = 4\%$.

5.2.1 Force and Power Analysis

The results of the resultant force and the required power are shown in Fig. 5.10. From the figure, both F_{res} and P decrease as the end locations of leading edge morphing move backwards.

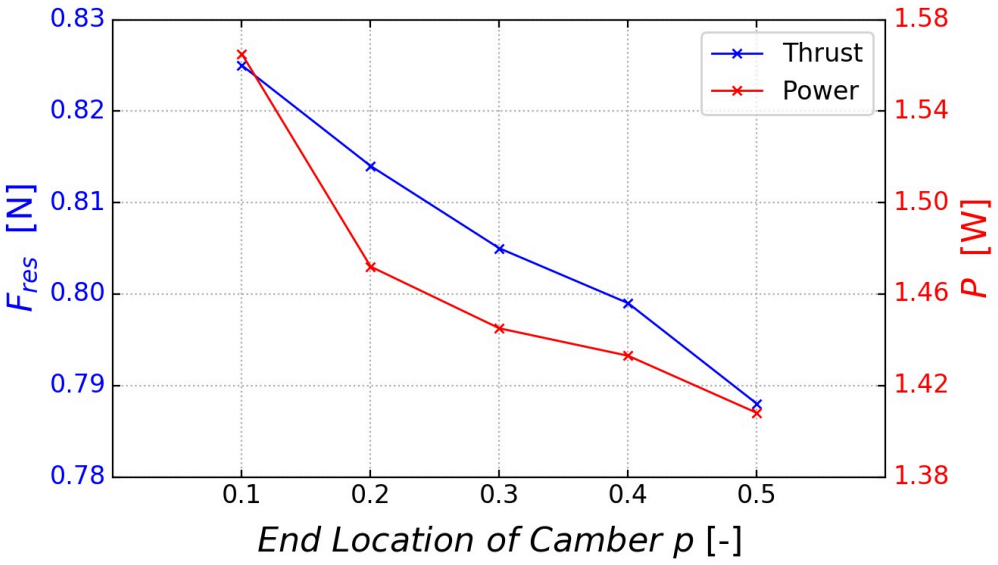

Figure 5.10: Thrust and power prediction vs. end location of LE camber, $m = 4\%$.

Fig. 5.11 illustrates the variation of efficiencies versus end position of LE camber. From the figure, the value of figure of merit experiences a great increase, followed by a slight decline, with the increasing value of p, while the value of power loading continuously increases. In addition, the case

with $p = 0.3$ achieve the best result of FoM (6.62% higher than the value of baseline case) and the highest value of PL (9.00% higher than the baseline case).

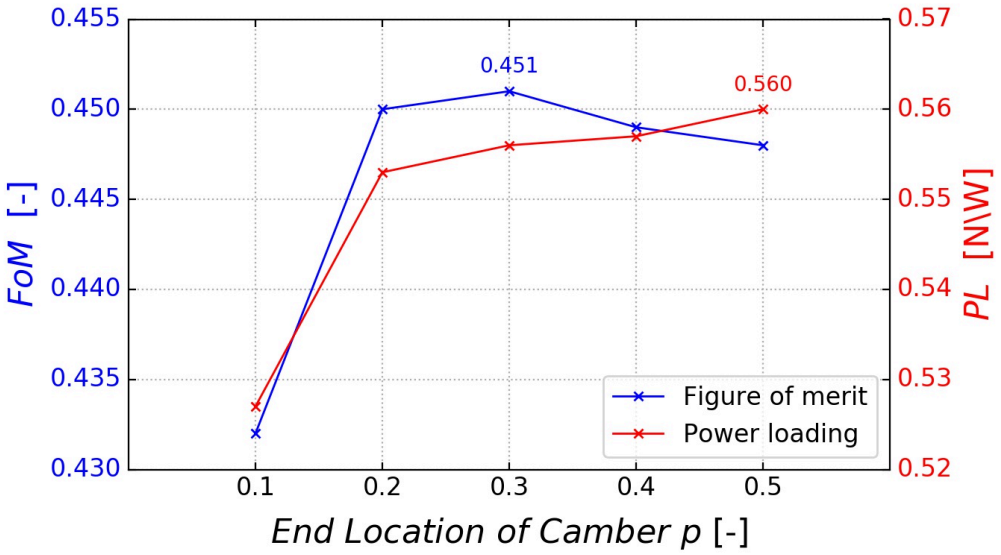

Figure 5.11: Efficiency prediction vs. end location of LE camber, $m = 4\%$.

The variation of vertical force for one blade with different p value is shown in Fig. 5.12. From the figure, all cases with cambered leading edge show similar lift variation patterns, and curves almost overlap with each other in most of the intervals except for the case $p = 0.1$.

In particular, the lift generation in the upper half exhibits a slightly descending trend with the increase of p. On the contrary, less vertical thrust is produced by the case $p = 0.1$ near the lowest point of the trace. Overall, the vertical thrust is slightly reduced as the end location of the LE camber moves backwards.

5.2.2 Flow Field Visualization

The downwash velocity contour for the cases with different end positions of LE morphing is shown in Fig. 5.13. Moreover, the cases $p = 0.1$, $p = 0.2$, $p = 0.3$ have a thrust angle of 95.12°, 93.36°, and 93.14°, respectively. As a consequence, the region with the highest downwash velocity will move slightly towards the negative y-axis. Besides, no obvious change in velocity magnitude and its influence range could be observed in this situation.

The vorticity contours for the cases with different LE end positions of morphing are shown in Fig. 5.14. From the figure, a significant change occurs when the blade is passing through the upper right part of its trace.

For case $p = 0.1$, the formation of LEV could be observed near the position $\psi = 150°$, then the

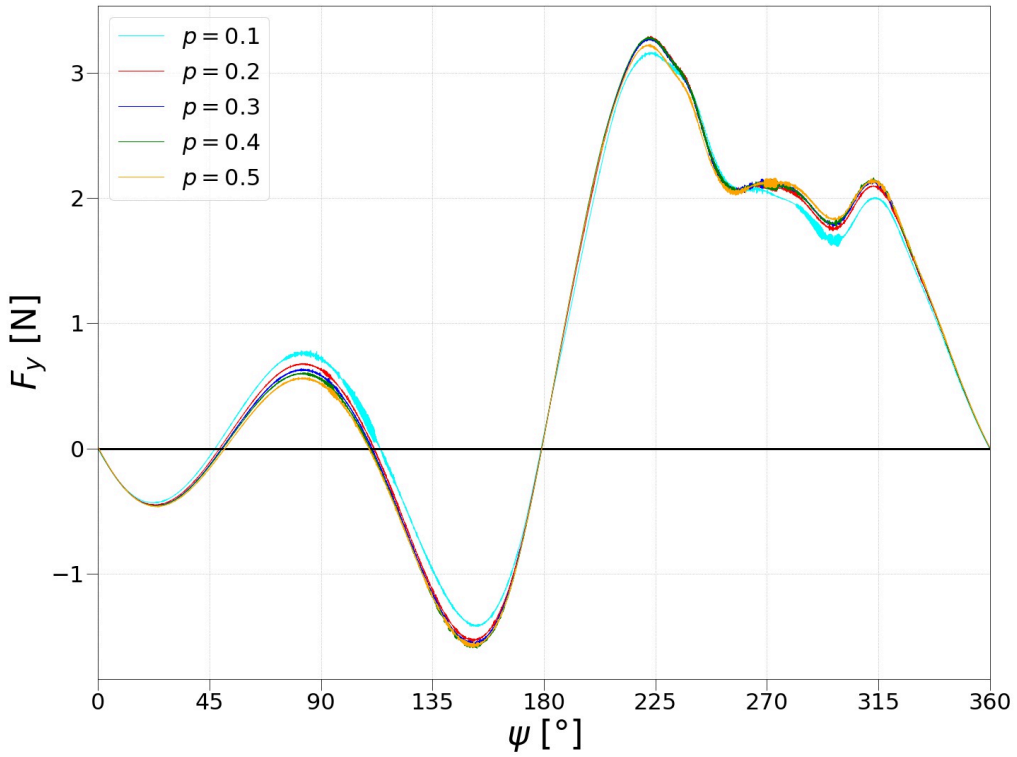

Figure 5.12: Vertical thrust distribution for one blade with different end position of LE camber.

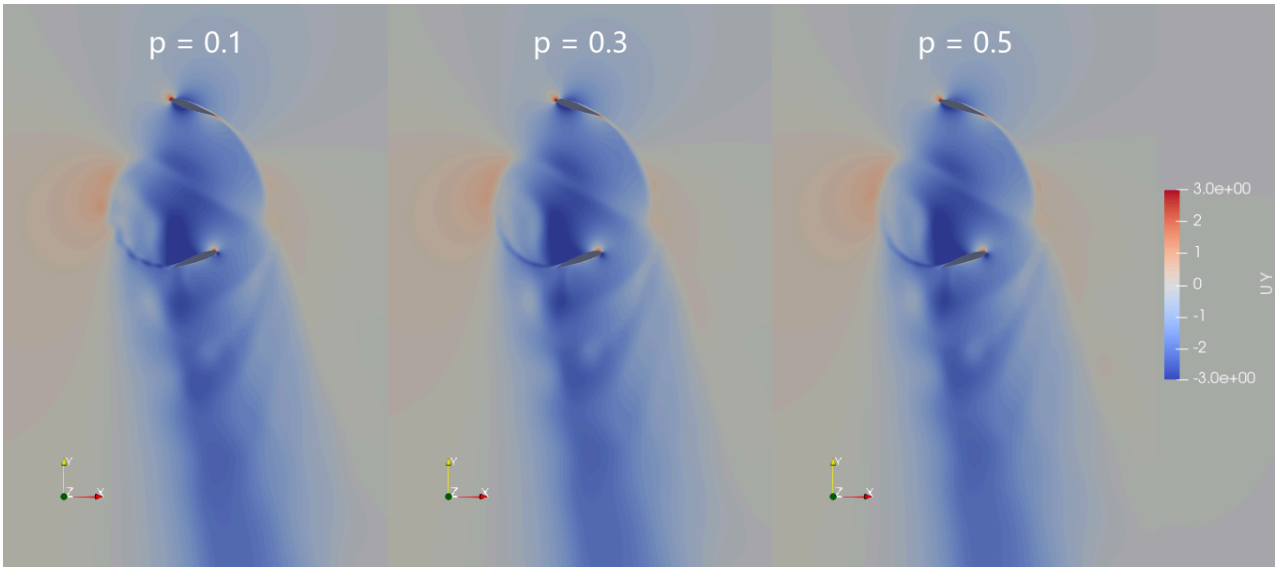

Figure 5.13: Downwash velocity for cases with different end position of LE camber.

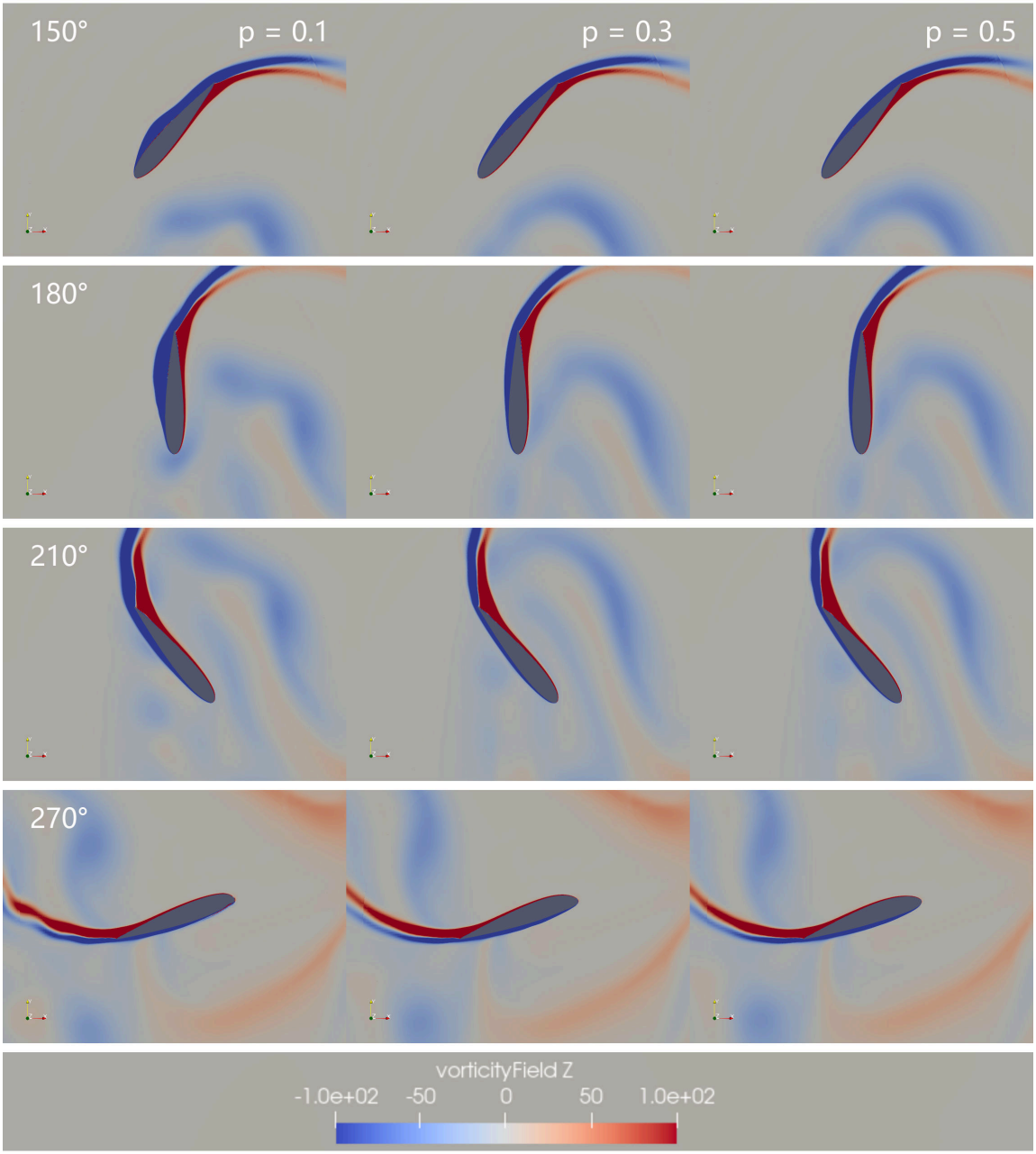

Figure 5.14: Vorticity field for cases with different LE end position.

vortex develops and spans the whole surface before it is eliminated due to decreasing pitching angle. However, as shown in the contours, with the increasing p value, there are no signs of the formation of vortex and boundary vorticity fluctuation during the entire trajectory in the case of $p = 0.3$ and $p = 0.5$.

A more detailed description of the unsteady phenomena and their corresponding influence on the pressure distribution is introduced in the next section.

5.2.3 Pressure Distribution along the Chord

Fig. 5.15 shows the pressure distribution for the cases with different end positions of morphing. Combining with the vertical thrust variation and the vorticity contours shown in the previous sections, the major difference of the pressure distribution can be summarized as follow :

- When the blade is passing the upper ends of the trajectory, i.e., $60° < \psi < 120°$, where relatively large camber degrees are employed, the suction peak at the outer surface (suction surface) achieves a relatively higher negative pressure value, which results in a slightly higher vertical thrust peak for the upper part.

- At the position of $150° < \psi < 180°$, for the case $p = 0.1$, the formation and development of leading edge vortex vary the pressure distribution on the outer surface. Consequently, moderate reduction of peak value at the leading edge and a stable pressure from the position 0.2 to 0.4 of the normalized chord, followed by a rapid decrease from the position of 0.5 to 0.7, could be observed. At the same time, the pressure distribution on the inner surface (pressure side) retains its consistency for all cases.

- When the blade is in the lower half of its trace, the major difference occurs at the position of $240° < \psi < 300°$. In particular, the pressure experiences a significant increase at the leading edge of the outer surface (pressure surface), and a fast descending successively in the case $p = 0.1$. Moreover, regarding the other two cases, they remain the similar distribution with respect to the pressure after a slight peak as the case $p = 0.1$.

5.3 Effect of Asymmetric Camber Morphing

This section investigates the aerodynamic performance of cases with asymmetric leading edge camber morphing. Therefore, cases in this section have different maximum camber degrees at the top and bottom of the circle. Besides, the aerodynamic performance of 3 cases with an averaged

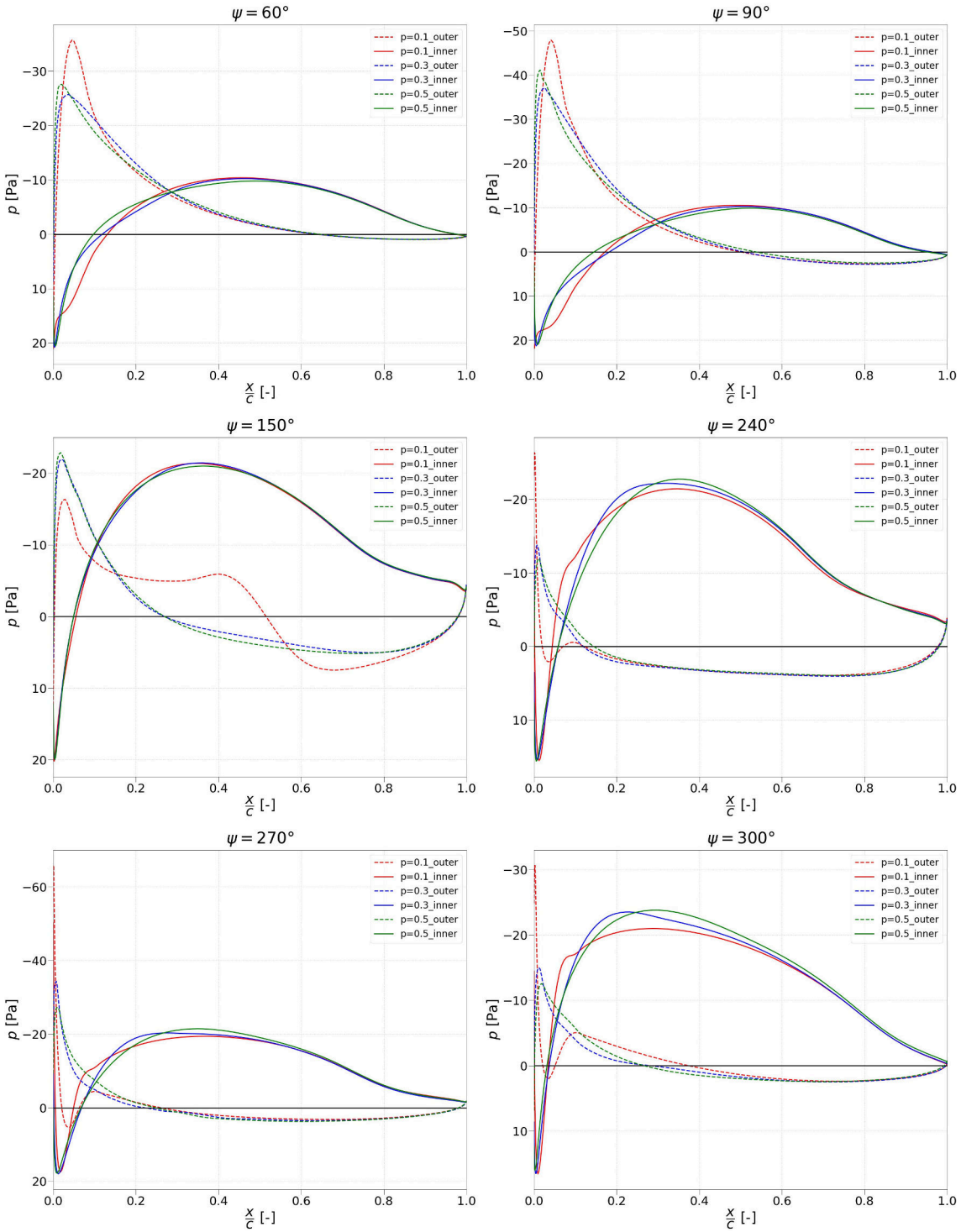

Figure 5.15: Pressure distribution for cases with different LE end position.

4%, i.e., $m = 4\%$, camber degree is investigated. Besides, the camber morphing of all blades in this section ends at the location of 30% of the normalized chord, i.e., $p = 0.3$.

5.3.1 Force and Power Analysis

The results of the force and the required power of airfoils with asymmetric cambered LE are included in Fig. 5.16, where U and L indicate the maximum camber degree for the upper half and lower half. From the figure, as more camber for the upper half and less camber for the lower half are employed, increasing resultant thrust and corresponding decreasing required power could be observed. In addition, the case U6/L2 shows the highest value of force (3.80% lower than baseline case) while the case U2/L6 achieves the greatest value of power loading (10.4% lower than baseline case).

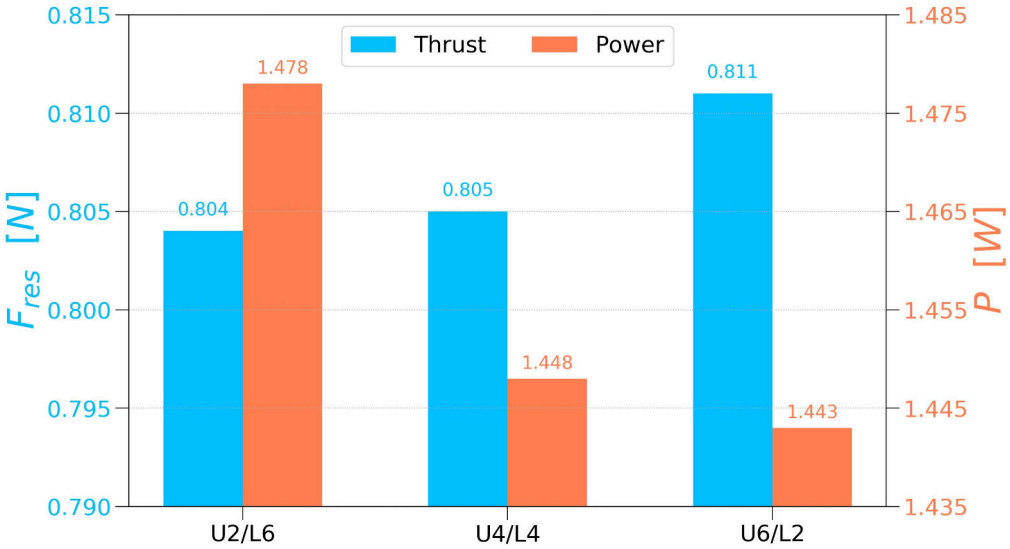

Figure 5.16: Thrust and power prediction for cases with asymmetric LE camber.

Fig. 5.17 illustrates the variation of efficiencies of airfoils with asymmetric cambered LE. From the figure, the value of the figure of merit shows a tendency to increase as the camber degree of the upper increases and the camber degree of the lower half decreases. Particularly, the case U6/L2 shows the best results of figure of merit (8.04% higher than baseline case) and the highest value of power loading (9.98% higher than baseline case), which are the best efficiencies results could be achieved by the case with cambered LE.

The variation of vertical force over the period of asymmetric LE camber is shown in Fig. 5.18. From the figure, for all three cases, the curves almost overlap with each other, and the contribution of lift generation of the upper part is still small, moreover, the majority of vertical lift is generated

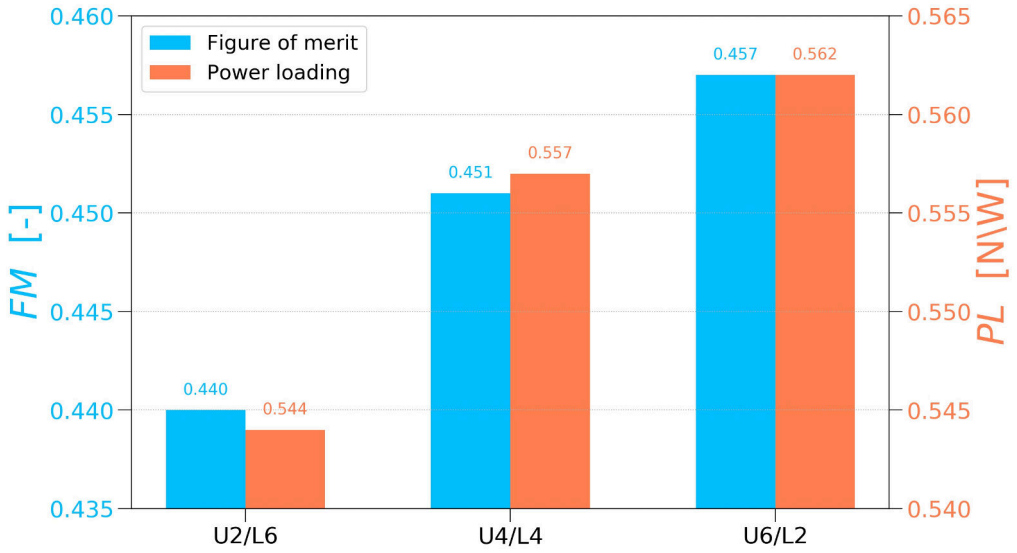

Figure 5.17: Efficiency prediction for cases with asymmetric LE camber.

in the lower half of the trace. In addition, the peak value is related to the corresponding camber degree m_U and m_L. Particularly, less camber at the upper part and more camber at the lower part indicate better performance at the upper half and worse performance at the lower half concerning lift generation.

5.3.2 Flow Field Visualization

The downwash velocity contour for the case with asymmetric cambered LE is shown in Fig. 5.19. From the figure, in the contour of velocity in the y-direction, no obvious change in velocity magnitude and its influence area could be observed. Moreover, the variation in thrust angle is less than 0.5°. It is worth mentioning that for all cases, the effect is most significant when the blade is at the lowest end of the circle.

Furthermore, for all cases investigated in this section, the fluid flows smoothly over the surface of airfoils with asymmetric leading edge camber, besides, there are no signs of vortex development or severe flow separation during the entire trajectory.

5.3.3 Pressure Distribution along the Chord

Fig. 5.20 shows the pressure distribution for the airfoils with asymmetric LE camber. Combining with the vertical thrust variation shown in the previous section, the major difference of the pressure distribution can be summarized as follow :

- When the blade is passing through the upper ends of its trajectory, i.e., $60° < \psi < 120°$, in

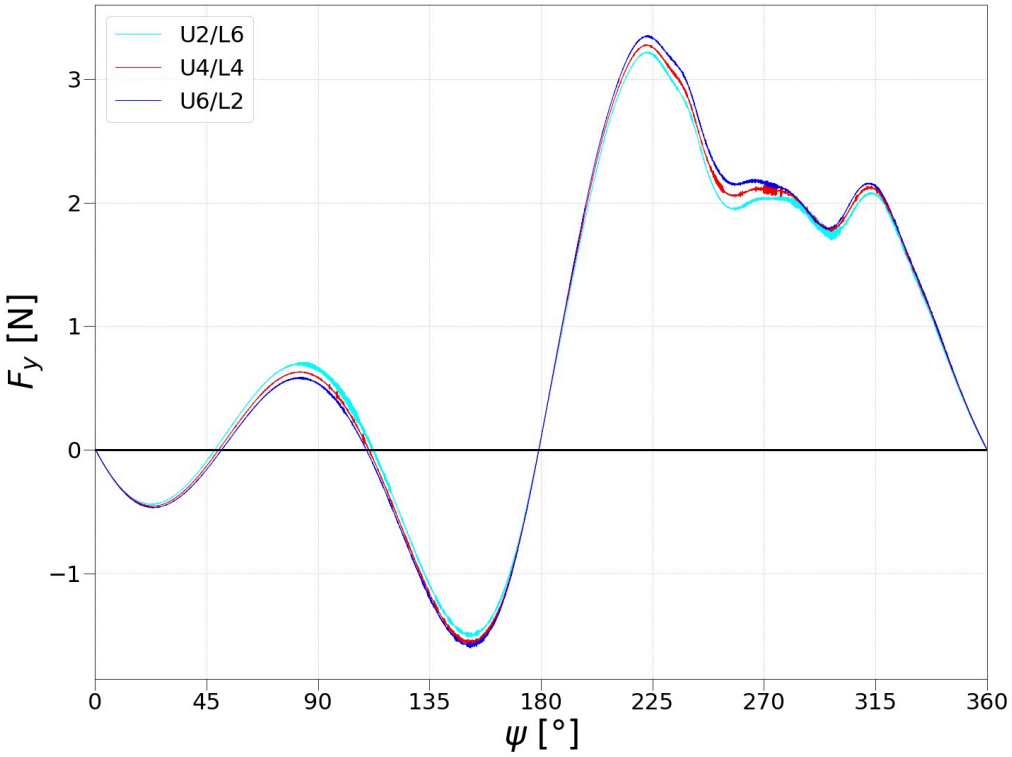

Figure 5.18: Vertical force distribution for one blade for cases with asymmetric LE camber.

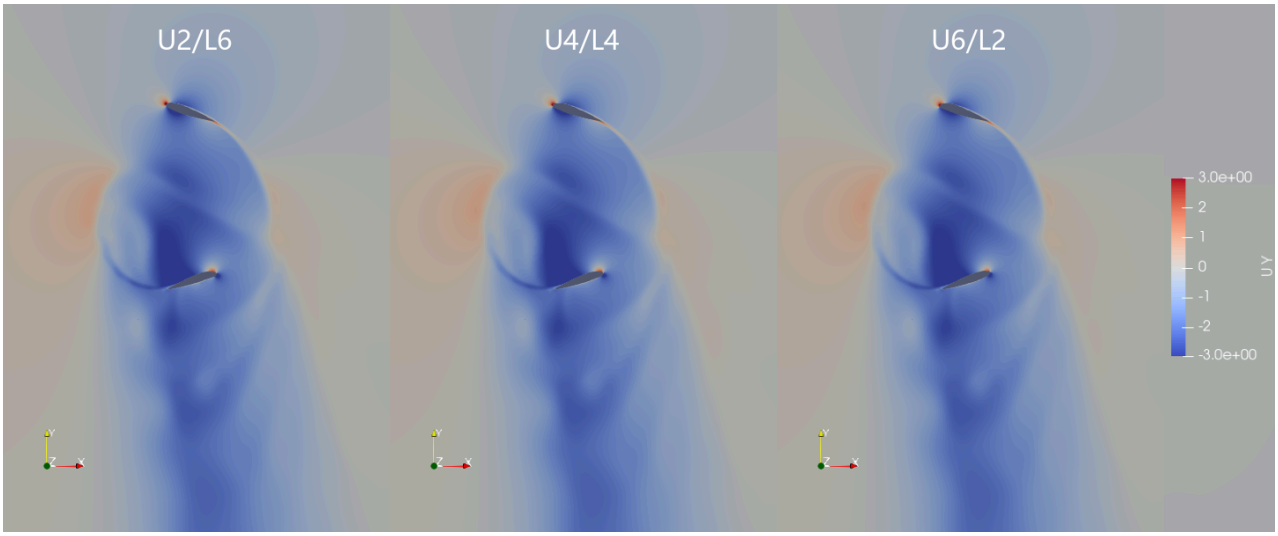

Figure 5.19: Downwash velocity for cases with asymmetric LE camber.

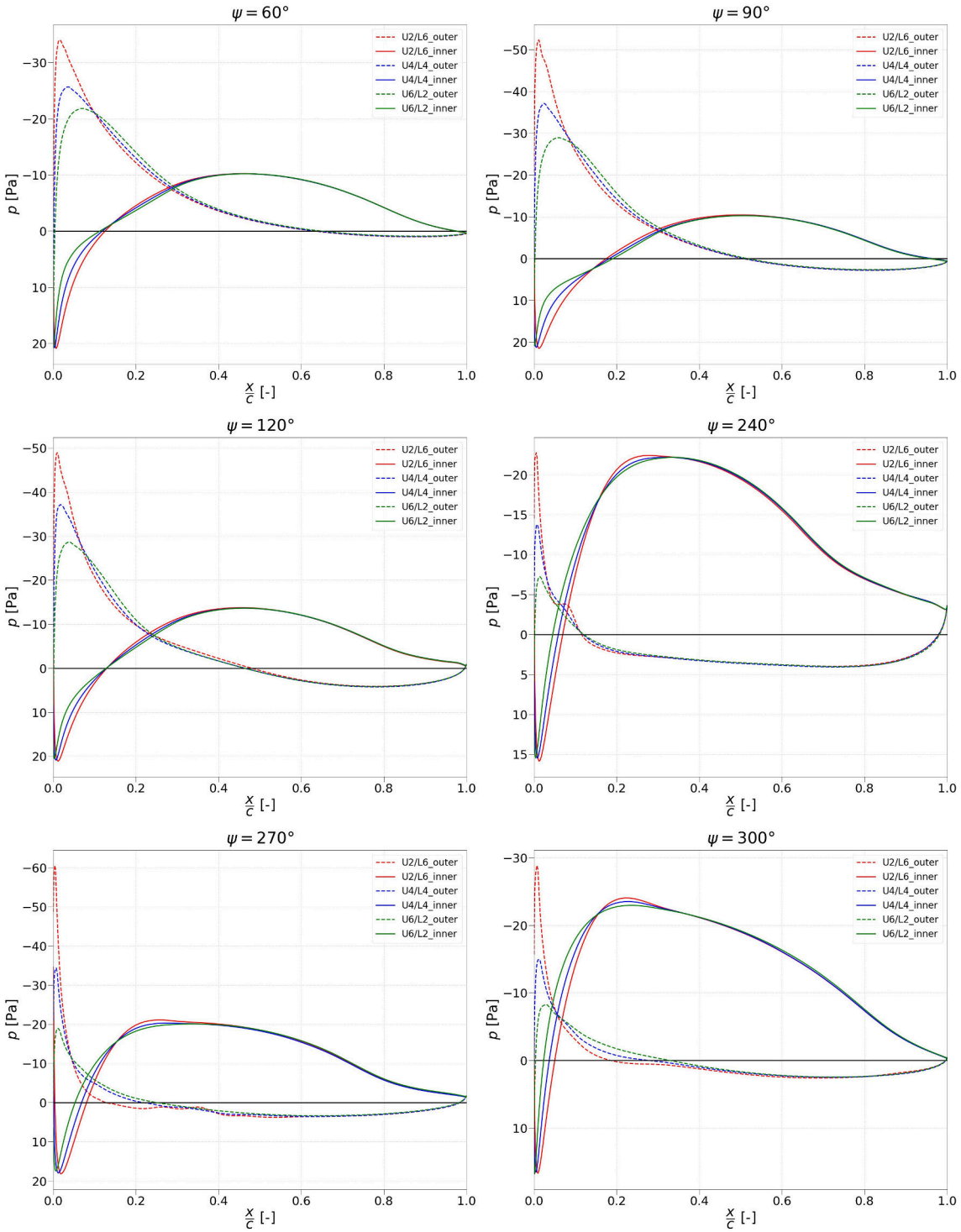

Figure 5.20: Pressure distribution for cases with asymmetric LE camber.

the case U2/L6, the negative pressure at the leading edge of the outer surface (suction surface) experiences an obviously higher suction peak, which results in a slightly higher lift value for the upper part.

- When the blade is in the lower part of its trace, the major difference occurs at the position $240° < \psi < 300°$. Similarly, higher negative pressure is observed at the leading edge of the outer surface (pressure side). Moreover, with the decreasing m_L and increasing m_U, the negative peak value is reduced, which results in slight increments in lift generation in the lower half for cases U4/L4 and U6/L2.

Overall, from the figure, the pressure distribution in all cases shows a smooth changing pattern since no formation of the vortex occurs. Besides, the influence of asymmetric LE camber effect on pressure distribution is not significant.

6 Conclusion

The objective of this work was to realize certain improvements in the aerodynamic performance of the cycloidal rotor system by employing dynamically morphing blades in the current CFD model. To achieve this goal, three different camber morphing methods, i.e., leading edge deflection, trailing edge deformation, and NACA camber concept, are first developed for the baseline 2-bladed system to define the morphing airfoils. Moreover, the structured grids are constructed for the whole computational domain by utilizing the mesh tool Pointwise. In addition, various types of mesh diffusivity in OpenFOAM are tested to ensure the grids follow the motion of the morphing surface and maintain the shape during the morphing process.

After the mesh generation, a series of 2D incompressible URANS numerical simulations are conducted by employing the open-source CFD tool OpenFOAM. Particularly, the effect of maximum camber degree, the effect of camber position, as well as the asymmetric camber effect for all three camber methods are investigated. The simulation results of cases with different camber concepts could be summarized as follow:

- For the case with cambered NACA airfoils, a moderate increase in thrust and the required power with respect to the ascending camber degree are obtained. Moreover, the highest value for both figure of merit and power loading could be achieved by utilizing such a camber concept. Especially, in the case with 16% camber NACA airfoils, the FoM reaches the value of 0.61, which is the highest value that can be achieved in this work.

  From the flow field visualization, for the case with cambered NACA airfoils, more intensified downwash velocity is observed. Specifically, the formation of the leading edge vortex at the upper left part is eliminated. However, the development of the vortex and its detachment on the pressure side could be observed at the lower end.

  According to the studies of camber position and asymmetric camber effect, the case in which the maximum camber occurs at 30% of the chord ($p = 0.3$) and the case with the symmetrical camber for the upper and lower half ($m_U = m_L$) show the best performance in efficiency.

- For the case with cambered TE, significantly higher resultant thrust and power levels can be achieved as the TE camber degree grows, while the efficiency would first increase and then decreases with the ascending of camber degree. Moreover, the case with 10% TE camber shows

the best result for figure of merit.

Moreover, for the case with camber TE, a intensified and more concentrated down-wash velocity is observed. Besides, the size of the leading edge vortex at the upper left half is slightly reduced. Moreover, vortex shedding in the wake region could be observed near the top and bottom of its trace. Consequently, the blade vortex interaction effect becomes important for the case with a relatively large TE camber degree.

As for the analysis of camber position and asymmetric camber effect, the best results of figure of merit is achieved by the case with $p = 0.2$ with the value of 0.566, while the case with $m_U < m_L$ shows a better performance in efficiency (FoM).

- For the case with cambered LE, the resultant thrust and the required power decrease with respect to the increasing of LE camber morphing degree. Besides, a slight improvement in efficiency could be expected when the camber degree is less than 4%.

  In addition, no significant change in downwash velocity for the case with cambered LE is obtained. As for the vorticity distribution, there are no signs of vortex development and severe flow separation during the entire trajectory for the cases with cambered leading edge. Therefore, the flow field condition is optimized by introducing such modification.

  Moreover, the case with $p = 0.3$ and the case with $m_U > m_L$ show the better results of FoM.

Overall, the simulation results verify that the case with the cambered trailing edge achieves the highest thrust increment while the cases with cambered NACA airfoils show the best improvement in efficiency. Besides, the optimization of the flow condition could be realized by introducing a relative small leading edge camber to the system.

Furthermore, the simulation results also indicate that, from all camber combinations, relatively large symmetric NACA camber with $p = 0.4$, modest asymmetric (more camber at lower half) TE camber with $p = 0.2$, and small asymmetric (more camber at upper half) LE camber with $p = 0.3$ have the greatest potential for further optimization.

Acknowledgements

First and foremost, I am extremely grateful to my tutor, Dr. Louis Gagnon, for his patience, continuous support and insightful comments during the past few months. Thanks for sharing your immense knowledge about cycloidal rotors and plentiful experience of OpenFOAM. This work could not be completed so smoothly without his guidance and involvement.

I would like to extend my sincere thanks to Dr. Stephane Fournier, for sharing his valuable insight on the camber morphing blade with me, which is of great help to my project.

My appreciation also goes out to the IAG-basement-crew, for providing solutions and suggestions for OpenFOAM related and other technical issues.

Moreover, I would like to express my sincere gratitude to my friends. It is their kind help and generous care over the past three years that have made my study and life in Stuttgart a wonderful time. Special thanks go to Handan, Hongjie and Zhenzi, for always beside me during the happy and hard moments to push me and motivate me. Without them, my everyday life would be way less fun.

Finally, I would like to thank my parents and my brother, who mean the most to me, for all the love, guidance and support throughout my life. Without them, I would not be where I am today.

Appendix

Relevant files of OpenFOAM settings are attached. The $fvSolution$ dictionary contains the settings for the PIMPLE algorithm and the $fvScheme$ file sets the numerical schemes for terms. The $pointDisplacaement$ file consists of the setting of boundary condition to of the point displacement field, which is employed for the realization of blade morphing. The $dynamicMeshDict$ includes the setting for mesh motion and deformation control.

Further settings of OpenFOAM, the Python script used to generate the pointDisplacement file, and the summary of simulation results can be obtained from the following link:
https://doi.org/10.18419/darus-2191

Appendix I fvSchemes

```
/*--------------------------------*- C++ -*----------------------------------*\
| =========                 |                                                 |
| \\      /  F ield         | OpenFOAM: The Open Source CFD Toolbox           |
|  \\    /   O peration     | Version:  v2006                                 |
|   \\  /    A nd           | Website:  www.openfoam.com                      |
|    \\/     M anipulation  |                                                 |
\*---------------------------------------------------------------------------*/
FoamFile
{
    version     2.0;
    format      ascii;
    class       dictionary;
    location    "system";
    object      fvSchemes;
}
// * * * * * * * * * * * * * * * * * * * * * * * * * * * * * * * * * * * * * //

ddtSchemes
{
   default backward;
}

gradSchemes
{
   default cellLimited leastSquares 1;
   grad(U) cellLimited leastSquares 1;
// grad(p)  Gauss linear limited 1;
   limitedGrad cellLimited leastSquares 1;
}

divSchemes
{
   default Gauss upwind;
   div(phi,U) Gauss limitedLinearV 1.0;
   div(phi,k) Gauss upwind;
   div(phi,omega) Gauss upwind;
   div(phi,epsilon) Gauss upwind;
   div((nuEff*dev2(T(grad(U))))) Gauss linear;
}

laplacianSchemes
{
   default Gauss linear corrected;
}

interpolationSchemes
{
   default linear;
}

snGradSchemes
{
   default corrected;
}
```

```
wallDist
{
    method meshWave;
}
// ************************************************************************* //
```

Appendix II fvSolution

```
/*--------------------------------*- C++ -*----------------------------------*\
| =========                 |                                                 |
| \\      /  F ield         | OpenFOAM: The Open Source CFD Toolbox           |
|  \\    /   O peration     | Version:  v2006                                 |
|   \\  /    A nd           | Website:  www.openfoam.com                      |
|    \\/     M anipulation  |                                                 |
\*---------------------------------------------------------------------------*/
FoamFile
{
    version     2.0;
    format      ascii;
    class       dictionary;
    object      fvSolution;
}
// * * * * * * * * * * * * * * * * * * * * * * * * * * * * * * * * * * * * * //

solvers
{
   "cellDisplacement.*"
   {
        solver          PCG;
        preconditioner  DIC;
        tolerance       1e-06;
        relTol          0;
        maxIter         100;
    }

    p
    {
        solver          PBiCGStab;
        preconditioner  DIC;
        tolerance       1e-02;
        relTol          0;
        minIter 1;
    }

    pFinal
    {
        $p;
        tolerance       5e-3;
    }

   "(pcorr|pcorrFinal)"
   {
      solver          PBiCGStab;
      preconditioner  DIC;
      tolerance       1e-2;
      relTol          0;
      smoother        GaussSeidel;
      nCellsInCoarsestLevel 256;
      agglomerator    faceAreaPair;
      minIter         1;
      maxIter         5;
   }
```

```
    "(U|k|omega|epsilon)"
    {
        solver          PBiCGStab;
        preconditioner        DILU;
        tolerance       1e-6;
        relTol          0;
      minIter     1;
    }

    "(U|k|omega|epsilon)Final"
    {
        $U;
      tolerance       1e-9;
        relTol          0;
    }
}

PIMPLE
{
 correctPhi          yes;
 nOuterCorrectors    30;
 nCcorrectors        3;
 nNonOrthogonalCorrectors 3;
 turbOnFinalIterOnly no;

 residualControl
 {
   "(U|k|omega|p)"
  {
   relTol           0;
   tolerance        1e-2;
  }
 }
}

relaxationFactors
{
 fields
 {
  p                0.3;
  pFinal           1.0;
 }
 equations
 {
  "(U)"            0.7;
  "(U)Final"       1.0;
  "(p)"            0.3;
  "(p)Final"       1.0;
  "(k|omega)"      0.3;
  "(k|omega)Final"  1.0;
 }
}
// ************************************************************************* //
```

Appendix III pointDisplacement

```
/*--------------------------------*- C++ -*----------------------------------*\
| =========                 |                                                 |
| \\      /  F ield         | OpenFOAM: The Open Source CFD Toolbox           |
|  \\    /   O peration     | Version:  v2006                                 |
|   \\  /    A nd           | Website:  www.openfoam.com                      |
|    \\/     M anipulation  |                                                 |
\*---------------------------------------------------------------------------*/
FoamFile
{
    version     2.0;
    format      ascii;
    class       pointVectorField;
    location    "0";
    object      pointDisplacement;
}
// * * * * * * * * * * * * * * * * * * * * * * * * * * * * * * * * * * * * * * * //

dimensions      [0 1 0 0 0 0 0];

internalField   uniform (0 0 0);

boundaryField
{
    "AMI*"
    {
        type            cyclicAMI;
    }
    farfield
    {
        type            fixedValue;
        value           uniform (0 0 0);
    }
    wing1
    {
        type            timeVaryingMappedFixedValue;
        value           uniform (0 0 0);
        offset          constant (0 0 0);
    }
    wing2
    {
        type            timeVaryingMappedFixedValue;
        value           uniform (0 0 0);
        offset          constant (0 0 0);
    }
    BaseAndTop
    {
        type            empty;
    }
}
// ************************************************************************* //
```

Appendix IV dynamicMeshDict

```
/*--------------------------------*- C++ -*----------------------------------*\
| =========                 |                                                 |
| \\      /  F ield         | OpenFOAM: The Open Source CFD Toolbox           |
|  \\    /   O peration     | Version:  v2006                                 |
|   \\  /    A nd           | Website:  www.openfoam.com                      |
|    \\/     M anipulation  |                                                 |
\*---------------------------------------------------------------------------*/
FoamFile
{
    version     2.0;
    format      ascii;
    class       dictionary;
    location    "constant";
    object      dynamicMeshDict;
}

// * * * * * * * * * * * * * * * * * * * * * * * * * * * * * * * * * * * * * //

dynamicFvMesh dynamicMultiMotionSolverFvMesh;
motionSolver multiSolidBodyMotionSolver;
motionSolverLibs ("libdynamicMesh.so");

interpolation patchCorrected
(
    (wing1 wing2)
    (farfield)
);

rotation1
{
    solidBodyMotionFunction  rotatingMotion;
    rotatingMotionCoeffs
    {
        origin      (0 0 0);
        axis        (0 0 1);
        omega       17.4532925199;
    }
}


dynamicMultiMotionSolverFvMeshCoeffs
{
    rotate_wholeDomain
    {
        solver solidBody;
        cellZone wholeDomain;
        solidBodyCoeffs
        {
            $rotation1;
        }
    }

   rotate_Wing1
    {
        cellZone AMI1;
```

```
        solver solidBodyDisplacementLaplacian;
        solidBodyDisplacementLaplacianCoeffs
        {
            solidBodyMotionFunction  multiMotion;
            multiMotionCoeffs
            {
                rotationMotion
                {
                    $rotation1;
                }
            pitchingMotion
            {
               solidBodyMotionFunction  oscillatingRotatingMotion;
               origin        (0.32 0.0 0.0);
               axis        (0 0 1);
               amplitude     (0 0 -20);  // degs
               omega        17.4532925199;//17.45329;
            }
            }
            diffusivity quadratic inverseDistance (wing1 wing2 AMI1_inner AMI2_inner
     AMI1_outer AMI2_outer);
             frozenDiffusion off;
             frozenPointsZone frozenAMI;
        }
    }

   rotate_wing2
    {
        cellZone AMI2;
        solver solidBodyDisplacementLaplacian;
        solidBodyDisplacementLaplacianCoeffs
        {
            solidBodyMotionFunction  multiMotion;
            multiMotionCoeffs
            {
                rotationMotion
                {
                    $rotation1;
                }
            pitchingMotion
            {
               solidBodyMotionFunction  oscillatingRotatingMotion;
               origin        (-0.32 0.0 0.0);
               axis        (0 0 1);
               amplitude     (0 0 20);  // degs
               omega        17.4532925199;
            }
            }
            diffusivity quadratic inverseDistance (wing1 wing2 AMI1_inner AMI2_inner
     AMI1_outer AMI2_outer);//
             frozenDiffusion off;
             frozenPointsZone frozenAMI;
        }
    }
}


// ************************************************************************* //
```

Bibliography

[1] F. Rodrigues, M. Habibnia, and J. Páscoa, "Novel propulsion system for vtol aircraft based on cycloidal rotors coupled with wings," 07 2020.

[2] J. B. Wheatley, "Simplified aerodynamic analysis of the cyclogiro rotating wing system," 1930.

[3] J. B. Wheatley and R. Windler, "Wind-tunnel tests of a cyclogiro rotor," 1935.

[4] I. S. Hwang, S. Y. Min, M. K. Kim, and S. J. Kim, "Multidisciplinary optimal design of cyclocopter blade system," in *46th AIAA/ASME/ASCE/AHS/ASC Structures, Structural Dynamics and Materials Conference*, 2005, p. 2287.

[5] I. S. Hwang, S. Y. Min, C. H. Lee, and S. J. Kim, "Experimental investigation of vtol uav cyclocopter with four rotors," in *48th AIAA/ASME/ASCE/AHS/ASC Structures, Structural Dynamics, and Materials Conference*, 2007, p. 2247.

[6] ——, "Development of a four-rotor cyclocopter," *Journal of Aircraft*, vol. 45, no. 6, pp. 2151–2157, 2008.

[7] C. H. Lee, S. Y. Min, J. W. Lee, and S. J. Kim, "Design and experiment of two-rotored uav cyclocopter," in *29th Congress of the International Council of the Aeronautical Sciences (ICAS)*, 2014, pp. 7–12.

[8] M. Benedict, M. Ramasamy, and I. Chopra, "Improving the aerodynamic performance of micro-air-vehicle-scale cycloidal rotor: an experimental approach," *Journal of Aircraft*, vol. 47, no. 4, pp. 1117–1125, 2010.

[9] M. Benedict, T. Jarugumilli, and I. Chopra, "Effect of rotor geometry and blade kinematics on cycloidal rotor hover performance," *Journal of Aircraft*, vol. 50, no. 5, pp. 1340–1352, 2013.

[10] M. Benedict, T. Jarugumilli, V. Lakshminarayan, and I. Chopra, "Effect of flow curvature on forward flight performance of a micro-air-vehicle-scale cycloidal-rotor," *AIAA journal*, vol. 52, no. 6, pp. 1159–1169, 2014.

[11] M. Benedict, E. Shrestha, V. Hrishikeshavan, and I. Chopra, "Development of a micro twin-rotor cyclocopter capable of autonomous hover," *Journal of Aircraft*, vol. 51, no. 2, pp. 672–676, 2014.

[12] M. Benedict, J. Mullins, V. Hrishikeshavan, and I. Chopra, "Development of a quad cycloidal-rotor unmanned aerial vehicle," *Journal of the American Helicopter Society*, vol. 61, no. 2, pp. 1–12, 2016.

[13] A. J. Kellen, "Performance measurements on a uav-scale cycloidal rotor in hover," Ph.D. dissertation, 2019.

[14] M. Kerho, "Adaptive airfoil dynamic stall control," *Journal of aircraft*, vol. 44, no. 4, pp. 1350–1360, 2007.

[15] A. Abdelmoula and J. Rauleder, "Aerodynamic performance of morphed camber rotor airfoils," in *AIAA Scitech 2019 Forum*, 2019, p. 1101.

[16] A. Abdelmoula, S. Platzer, M. Hajek, and J. Rauleder, "Numerical investigation of the effects of dynamic camber variation on the airfoil characteristics of a pitching rotor airfoil," in *AIAA Scitech 2020 Forum*, 2020, p. 1302.

[17] L. Ferrier, M. Vezza, and H. Zare-Behtash, "Improving the aerodynamic performance of a cycloidal rotor through active compliant morphing," *Aeronautical Journal*, vol. 121, no. 1241, pp. 901–915, 2017.

[18] H. Zhang, Y. Hu, and G. Wang, "The effect of aerofoil camber on cycloidal propellers," *Aircraft Engineering and Aerospace Technology*, 2018.

[19] E. N. Jacobs, K. E. Ward, and R. M. Pinkerton, *The Characteristics of 78 related airfoil section from tests in the Variable-Density Wind Tunnel*. US Government Printing Office, 1933, no. 460.

[20] B. K. Woods, J. H. Fincham, and M. I. Friswell, "Aerodynamic modelling of the fish bone active camber morphing concept," in *Proceedings of the RAeS Applied Aerodynamics Conference, Bristol, UK*, vol. 2224, 2014.

[21] "Investigation of the reynolds number on the performance of a cycloidal rotor," Stuttgart, pp. VIII, 59 Seiten, 2021, institut für Aerodynamik und Gasdynamik.

[22] B. Engquist, "Far field computational boundary conditions," *Journal of Computational Mathematics*, vol. 7, no. 2, pp. 113–120, 1989. [Online]. Available: http://www.jstor.org/stable/43692421